AN ABSTRACT OF THE THESIS OF

Guangliang He for the degree of Doctor of Philosophy in Physics presented on May 15, 1992.

Title: A Cloudy Quark Bag Model of S, P, and D Wave Interactions for the Coupled Channel Antikaon-Nucleon System

Abstract approved: Redacted for Privacy

Rubin H. Landau

The Cloudy Quark Bag Model is extended from S-wave to P- and D-wave. The parameters of the model are determined by K^-p scattering cross section data, $K^-p \to \Sigma\pi\pi\pi$ production data, K^-p threshold branching ratio data, and $K^-p \to \Lambda\pi\pi\pi$ production data. The resonance structure of the $\Lambda(1405)$, $\Sigma(1385)$, and $\Lambda(1520)$ are studied in the model. The shift and width of kaonic hydrogen are calculated using the model.

A Cloudy Quark Bag Model of S, P, and D Wave Interactions for the Coupled Channel Antikaon-Nucleon System

by

Guangliang He

A Thesis submitted to

Oregon State University

in partial fulfillment of the

requirements for the degree of

Doctor of Philosophy

Completed May 15, 1992

Commencement June 1993

APPROVED:

Redacted for Privacy

Professor of Physics in charge of major

Redacted for Privacy

Head of Department of Physics

Redacted for Privacy

Dean of Graduate School

Date thesis presented May 15, 1992

Typed by Guangliang He for Guangliang He

ACKNOWLEDGEMENTS

This thesis is dedicated to Haiyan.

I am extremely thankful to Dr. Rubin H. Landau for providing me the opportunity and the guidance for my graduate study here at OSU. It has been very rewarding to work with his patience, understanding, dedication and professionalism. It is very rewarding and heartwarming to work with someone who is not only a great teacher, but also a friend. I thank Dr. Landau and Mrs. Landau for the help they have given to my family.

I thank Jeffrey Schnick for initiating the antikaon research. I thank Paul Fink, Milton Sagen, Timothy Mefford and Dinghui Lu for many hours of helpful discussion and for all the assistance they provided me on this project. I thank Dr. Rubin .H. Landau, Dr. Thomas Dillon, Dr. Albert W. Stetz, Dr. Allen Wasserman, Dr. Henri Jansen and Dr. Victor A. Madsen for their critical review of the material and their excessive cooperation with respect to scheduling requirements.

I thank the United States Department of Energy for research support.

Table of Contents

List of Figures

List of Tables

A Cloudy Quark Bag Model of S, P, and D Wave Interactions for the Coupled Channel Antikaon-Nucleon System

Chapter 1

Introduction

1.1 History of the Cloudy Bag Model

Nucleons are made of quarks, and the interactions between quarks (therefore the nucleons) constitute the strong interaction. The theory for the strong interaction between quarks is Quantum Chromodynamics, or QCD[1, 2]. Although this theory is so complicated that no one has yet found an exact solution, there are a number of phenomenological models which incorporate the features expected from QCD. One of them is the bag model developed by the MIT group, the MIT bag model[3, 4, 5, 6]. In the MIT bag model, quarks are confined to an extended region of space-time. A constant energy density is associated with the volume of the bag and the balance between this density and field pressure dynamically determines the bag configuration.

The MIT bag model has been remarkably successful in explaining the static properties of the low-lying hadrons[5, 7]. There is however one major difficulty in this model, namely the lack of *chiral symmetry.* This symmetry is an important property of QCD itself. Further, experiments have shown that besides isospin, the chiral SU(2)×SU(2) is the best symmetry in the strong interaction[8]. A classic example of a chiral symmetric theory is the σ-model[9] in which the massless nucleon couples to an isospin scalar field σ and an isospin vector field π. The potential of the σ and π fields provides a mechanism for *spontaneous symmetry breaking.* According to the Goldstone's theorem[10, 11], this eventually gives a finite mass to the nucleon and leaves a massless boson field.

The difficulty of lack of chiral symmetry was recognized by the MIT group soon after the original MIT model was developed. In 1975, Chodos and Thorn[12] made a simple generalization of the σ-model to the original MIT bag model. The phenomenological fields σ and $\vec{\pi}$ in the σ-model are coupled to the quarks on the surface of the bag to conserve the chirality.

A number of extensions to the original MIT bag model have been developed to restore chiral symmetry by introducing the pion field as a Goldstone boson[13, 14, 15, 16, 17]. Among them, the *little brown bag*, proposed by the Stony Brook group[13, 14] was a combination of nonlinear σ-model and the original MIT bag model. With the idea of a two phase picture of physical hadrons, Brown and Rho proposed that the interior of the static MIT bag contains asymptotically free, massless quarks, while the exterior contains pions–the Goldstone bosons of SU(2)×SU(2). The typical value of the bag radius is about 0.3 fm, a small number due to the tremendous pressure of

pion field outside the bag.

Jaffe continued Brown and collaborators' work in a different direction[15]. He worked with a classical pion field and took the view that the MIT bag should not be drastically altered by the coupling to the pion field. In fact, in the perturbation expansion procedure used by Jaffe, the first term is exactly the MIT bag model.

In the early 1980s the *Cloudy Bag Model* (CBM) [18, 19, 20, 21, 22, 23, 24] was proposed by the TRIUMF group. As with Jaffe's bag model, the CBM also uses a perturbative approach. However, it has two distinguishing features which differ from Jaffe's model: (a) using a quantized pion field and (b) letting the pion penetrate into the interior of the bag. Although it is contrary to the two phase picture of hadrons to have a pion field inside the bag, there are reasons to justify it and it is consistent within the approximation level of the model[16, 17, 23, 24]. First, the probability of creating $\bar{q}q$ objects with the quantum number of the pion is non-zero for a finite distance between quarks. Therefore the pion field will have finite probability to get into the interior of the bag. Also, since the surface of the bag (nucleon) must be dynamic due to its emitting and absorbing the pion field, the time-averaged pion field will penetrate into the bag to some extent. Finally, due to the static nature of the bag model, we are restricted to study low energy interactions, and therefore, a long wavelength approximation of pion field is acceptable and in this limit the pion field penetrates all space.

The CBM Lagrangian is a highly non-linear model. Any real calculation has to be carried out in a perturbation expansion fashion. The zeroth order term of such a perturbation expansion is just the MIT bag model. The CBM

was very successful in a number of calculations, such as predicting the axial current coupling constant g_A, the P_{33} resonance, and the nucleonic charge radii and magnetic moments[25, 26]. Nevertheless, with the original surface coupling CBM Lagrangian, there is no obvious prediction for low energy pion-baryon scattering. A volume pseudovector coupling CBM was introduced later by applying a unitary transformation to the surface coupling quark field[27]. Weinberg's effective Lagrangian for the pion-nucleon system[28, 29] is found within the volume coupling CBM, and in fact the pion-nucleon scattering was studied in detail for volume coupling CBM[30, 31, 32, 33, 34]. The volume coupling CBM was also extended from SU(2) to SU(3) for studying the kaon-nucleon and S-wave antikaon-nucleon scattering[35, 36].

1.2 History of the $\bar{K}N$ Interactions

In this thesis, we study the $\bar{K}N$ system in the region of center of mass energy from 1250 to 1550 MeV.

$$K^- p \longrightarrow \begin{cases} K^- p \\ \bar{K}^0 n \\ \pi^+ \Sigma^- \\ \pi^0 \Sigma^0 \\ \pi^- \Sigma^+ \\ \pi^0 \Lambda \end{cases} \tag{1.1}$$

Within this energy range, the $\bar{K}N$ system couples to the two body channels $\pi\Lambda$, $\pi\Sigma$, and three body channels $\pi\pi\Sigma$. At sub-threshold energy, this system couples to the resonances $\Lambda(1405)$ (S-wave) and $\Sigma(1385)$ (P-wave). Above

the threshold, the system couples to the $\Lambda(1520)$ (D-wave) at COM energy 1520 MeV.

Several kinds of experimental data exist for the $\bar{K}N$ system. The scattering cross sections from 70 to 513 MeV/c of K^- incident momentum, mainly from hydrogen bubble chamber experiments, consist the largest portion of the data[37, 38, 39, 40, 41, 42, 43, 44, 45, 46]. At zero momentum, the K^-p branching ratios are also measured and reported by different groups[47, 48, 49, 50]. Below the threshold, there are also data derived from $\pi\Sigma$ mass spectra of the $\Lambda(1405)$ production processes[51, 52] and data derived from $\pi\Lambda$ mass spectra of the $\Sigma(1385)$ production processes[53]. There are also experimental data on the X-ray of $2p$-$1s$ transition of K^-p atomic state.

Although there are large numbers of experimental data on the $\bar{K}N$ interactions, there is not yet a theory which can describe all these data in a consistent way. Unexplained experimental results include the nature of $\Lambda(1405)$, the shift and width of $1S$ state of kaonic hydrogen, the branching ratios of K^-p at rest. This helps make this system more difficult and also more interesting.

1.3 The Layout of Thesis

In this thesis, we first extend the Cloudy Bag Model from S-wave only to P- and D-wave. This is our theoretical foundation for studying the $\bar{K}N$ system. We derive the potential from the CBM and use it as the driving term in a coupled channel Lippmann-Schwinger Equation. Then we introduce the

numerical methods used for solving the coupled channel Lippmann-Schwinger Equation. Next we deduce the parameters of the model from fitting the model to experimental data with the method of minimizing χ^2. We also introduce some of the applications of the extended CBM for the $\bar{K}N$ system. Finally, we discuss the conclusions from this study and some future directions to study.

Chapter 2

The Cloudy Bag Model

2.1 The Basic Cloudy Bag Model Lagrangian

In the early 1980's, there was a great deal of interest in extensions of the MIT bag model to incorporate Partial Conservation of Axial-vector Current (PCAC). One of the models extending the MIT bag model is the Cloudy Bag Model developed by the TRIUMF group[20, 21, 19, 25, 23, 22, 24, 54].

As we mentioned in the introduction, most physicists believe that Quantum Chromo-Dynamics (QCD) is the best candidate for a theory for the interactions between quarks and gluons. But because of the high degree of difficulty, no one has found a solution of QCD yet. (The numerical solution of lattice QCD may not be too far from reality due to the rapid development of massive parallel computers.)

The QCD theory is an SU(3) gauge theory of quarks and gluons based on the symmetry of an internal quantum number called "color". The non-Abelian nature of SU(3) leads to some of the most important features of QCD. First, at high-momentum transfer or short distances, the interactions

between quarks become weaker and weaker until the point when quarks become free from each other— "asymptotic freedom". Second, it appears that at large distances the interactions grow stronger and stronger and it takes infinitely large energy to separate single quark from hadrons. This leads to the confinement of quarks into color-singlet states. Although there is no theoretical proof of quark confinement based on QCD yet, the fact that people have yet to see a free quark experimently supports this assumption.

There are several models which try to incorporate these important features of QCD to study the strong interaction. The bag model developed by the group at MIT is one of them[3, 4, 5]. In the MIT bag model, the "quark confinement" is achieved by only allowing the quarks to stay inside a small space-like cavity—the bag, not outside of the cavity. The bag acts like an infinitely high potential wall. Inside the bag, quarks move freely like in free space, therefore the "asymptotic freedom". In a mathematical manner, the MIT bag model can be described by the Lagrangian density[12, 15]

$$\mathcal{L}_{MIT} = (\frac{i}{2}\bar{q} \overleftrightarrow{\partial} q - B)\theta_v - \frac{1}{2}\bar{q}q\delta_s \tag{2.1}$$

where q is the quark field, B is a universal constant called the "bag pressure", v is the volume of the bag, θ_v is a step-function of the bag defined as

$$\theta_v(x) = \begin{cases} 1 & \text{where } x \text{ inside bag} \\ 0 & \text{where } x \text{ outside bag} \end{cases} \tag{2.2}$$

and δ_s is the surface delta function defined by

$$\partial^\mu \theta_v = n^\mu \delta_s \tag{2.3}$$

n^μ being the outward 4-normal to the bag surface. For a static spherical bag, these functions are reduced to the regular step-function and the Dirac δ-function

$$\theta_v(x) \rightarrow \theta(R-r) \tag{2.4}$$

$$\delta_s(x) \rightarrow \delta(R-r) \tag{2.5}$$

The equations of motion for the MIT bag model are obtained by demanding the action S

$$S = \int d^4x \, \mathcal{L}_{MIT}(x) \tag{2.6}$$

is stationary under arbitrary changes in the field configurations

$$q \rightarrow q + \delta q \tag{2.7}$$

$$\bar{q} \rightarrow \bar{q} + \delta\bar{q} \tag{2.8}$$

$$\theta_v \rightarrow \theta_v + \epsilon\delta_s \tag{2.9}$$

$$\delta_s \rightarrow \delta_s - \epsilon n \cdot \partial\delta_s \tag{2.10}$$

The results are the Dirac Equation inside the bag

$$i \not{\partial} q(x) = 0 \quad r < R, \tag{2.11}$$

the linear boundary condition

$$i \not{n} q(x) = q(x) \quad r = R, \tag{2.12}$$

and the condition for the bag pressure

$$B = -\frac{1}{2} n \cdot \partial \left[\bar{q(x)} q(x)\right]_{r=R}. \tag{2.13}$$

Now, let us study the symmetry of the MIT bag model under the "chiral transformation". In an infinitesimal chiral transformation, the quark fields transform as

$$q \rightarrow q - i(\vec{\epsilon}\cdot\vec{\tau}/2)\gamma_5 q \tag{2.14}$$

$$\bar{q} \rightarrow \bar{q} - i\bar{q}\gamma_5(\vec{\epsilon}\cdot\vec{\tau}/2) \tag{2.15}$$

where $\vec{\tau}$ is the Pauli matrices for the isospin SU(2), and $\vec{\epsilon}$ is an infinitesimal parameter. The MIT Lagrangian density transforms as

$$\mathcal{L} \rightarrow \mathcal{L} + \frac{i}{2}\bar{q}\vec{\tau}\cdot\vec{\epsilon}\gamma_5 q\delta_s \tag{2.16}$$

and it does *not* vanish. The source of this non-vanishing term is the surface term $\frac{1}{2}\bar{q}q\delta_s$. It is "chiral-odd" because it changes the chirality of the quark hitting the bag surface, therefore, violating the chiral symmetry. Because of the lack of invariance of the Lagrangian density under the chiral transformation, the current $\vec{A}^\mu$ associated with the transformation is not conserved. It has the form

$$\vec{A}^\mu = \bar{q}\gamma^\mu\gamma_5\frac{\vec{\tau}}{2}q\theta_v \tag{2.17}$$

and a non-vanishing divergence

$$\partial_\mu\vec{A}^\mu = i\bar{q}\gamma_5\frac{\vec{\tau}}{2}q\delta_s \tag{2.18}$$

The lack of chiral symmetry presents an essential problem for the MIT bag model, since the experiments have shown that chiral symmetry is a good symmetry of strong interactions. For example, Pagels has concluded that, "SU(2)×SU(2) is a good hadron symmetry to within 7%. This makes chiral

SU(2)×SU(2) the most accurate hadron symmetry after isotopic invariance"[8]. In an ideal chiral symmetric world, the quarks are massless and the pions, as the Goldstone bosons, are massless, and we would have the conserved axial current $\partial_\mu \vec{A}^\mu = 0$. But in the real world, the pions have a small mass (compare to other hadrons), and the axial current is only partially conserved (PCAC)[55],

$$\partial_\mu \vec{A}^\mu = -f_\pi m_\pi^2 \vec{\phi} \tag{2.19}$$

where f_π is the pion decay constant and $\vec{\phi}$ is the pion field.

There are many models to restore the chiral symmetry in the MIT bag model[12, 56, 13, 15]. One remarkable way to solve this problem is the *Cloudy Bag Model*[20, 21, 25, 27, 19] by the TRIUMF group. In the original CBM, the pion fields are introduced into the picture. The pions interact with quarks on the surface of the bag to compensate the chirality change of quarks hitting the surface. The CBM Lagrangian density has the form

$$\mathcal{L}_{CBM} = \left(\frac{i}{2}\bar{q} \overleftrightarrow{\partial} q - B\right)\theta_v - \frac{1}{2}\bar{q}e^{i\vec{\tau}\cdot\vec{\phi}\gamma_5/f}q\delta_s + \frac{1}{2}\left(D_\mu\vec{\phi}\right)^2 \tag{2.20}$$

Here $\vec{\phi}$ is the three-vector field of pions, ϕ is the magnitude of the pion field, and $\hat{\phi}$ is the unit vector giving its direction in isospin space

$$\phi = \left(\vec{\phi}\cdot\vec{\phi}\right)^{1/2} \tag{2.21}$$

$$\hat{\phi} = \vec{\phi}/\phi \tag{2.22}$$

The $D_\mu\vec{\phi}$ in (2.20) is the "covariant derivative"

$$D_\mu\vec{\phi} = (\partial_\mu\phi)\hat{\phi} + f\sin(\phi/f)\partial_\mu\hat{\phi} \tag{2.23}$$

Unlike prior hybrid bag models, the CBM allows the pions to penetrate into the interior of the bag. This may sound unrealistic but it does have its justification. In the MIT bag model and the CBM, a bag is a static spherical cavity with a sharp boundary. Since the bag is meant to simulate the confinement generated by quark gluon interaction, it is impossible to believe that the bag remains static and unperturbed by the interaction of quarks and pions on the boundary. The very concept of the interior and exterior of the bag, therefore, is by no means clear cut. Letting pions penetrate into the bag does not make the CBM inferior to other bag models which excludes pions from the interior of the bag, but if anything, more realistic.

Now let us consider the chiral transformation

$$q \rightarrow q - i\vec{\epsilon}\cdot\vec{\tau}/2\,\gamma_5 q \tag{2.24}$$

$$\vec{\phi} \rightarrow \vec{\phi} + \vec{\epsilon} f + f(\vec{\epsilon}\times\hat{\phi})\times\hat{\phi}\,[1-(\phi/f)\cot(\phi/f)] \tag{2.25}$$

The CBM Lagrangian density (2.20) is invariant under this chiral transformation

$$\begin{aligned}\delta\mathcal{L} &= \frac{\partial\mathcal{L}}{\partial q}\delta q + \frac{\partial\mathcal{L}}{\partial(\partial_\mu q)}\delta(\partial_\mu q) + \delta\bar{q}\frac{\partial\mathcal{L}}{\partial\bar{q}} + \delta(\partial_\mu\bar{q})\frac{\partial\mathcal{L}}{\partial(\partial_\mu\bar{q})} \\ &\quad + \frac{\partial\mathcal{L}}{\partial\vec{\phi}}\delta\vec{\phi} + \frac{\partial\mathcal{L}}{\partial(\partial_\mu\vec{\phi})}\delta(\partial_\mu\vec{\phi}) \\ &= 0\end{aligned} \tag{2.26}$$

Further there is conserved axial current associated with this chiral transformation

$$\partial_\mu\vec{A}^\mu = 0 \tag{2.27}$$

where the axial current has the form

$$\vec{A}^{\mu} = \bar{q}\gamma^{\mu}\gamma_5\frac{\vec{\tau}}{2}q\theta_v + \left[f\hat{\phi}\partial^{\mu}\phi + \frac{f^2}{2}(\partial^{\mu}\hat{\phi})\sin(2\phi/f)\right] \tag{2.28}$$

Now if we go back to the real world in which the chiral symmetry is broken and the pion has a finite mass m_π, the CBM Lagrangian will have a mass term for the pions

$$\mathcal{L}_b = -\frac{1}{2}m_\pi^2\phi^2 \tag{2.29}$$

The subscript 'b' is added because this term 'breaks' the chiral symmetry. Once the chiral symmetry is broken, the axial current is no longer conserved, and it has a non-vanishing divergence

$$\partial_\mu A^{\mu} = -fm_\pi^2\vec{\phi} \tag{2.30}$$

This is the same as the PCAC condition Eq. (2.19).

2.2 Volume-Coupling Cloudy Bag Model

A direct consequence of PCAC in the energy pion-nucleon scattering is the Weinberg-Tomozawa relation[28, 29] originally developed in the late 1960's. According to the Weinberg-Tomozawa relation, the S-wave scattering length of a pion on any target (other than another pion) of isospin T_t, is exactly

$$a_T = -L\left(1+\frac{m_\pi}{m_t}\right)^{-1}[T(T+1) - T_t(T_t+1) - 2] \tag{2.31}$$

Here T is the total isospin, $L = 0.11m_\pi^{-1}$ is a convenient length[28], the term in parenthesis is the center of mass correction, and the term in the square brackets is $2\hat{T}_t \cdot \hat{T}_\pi$. We can see that the scattering length is purely

isovector coupling in the soft-pion limit. The values of scattering lengths predicted by this relation compare very well with experimental values[28]. If the CBM is a valid candidate for meson-baryon interaction, one would expect the CBM to repeat the successes of the Weinberg-Tomozawa relation. But unfortunately, the original CBM has no obvious prediction for low-energy pion-nucleon scattering[27]. However, we can perform an unitary transformation on the original CBM Lagrangian density so the Weinberg-Tomozawa relation appears explicitly[27].

Consider the following unitary transformation on the Lagrangian density

$$q \rightarrow \quad q_w \quad = Sq \tag{2.32}$$

$$\bar{q} \rightarrow \quad \bar{q}_w \quad = \bar{q}S \tag{2.33}$$

with

$$S = \exp\left[i\vec{\tau}\cdot\vec{\phi}(\gamma_5/2f)\right] \tag{2.34}$$

With this transformation, the CBM Lagrangian density (2.20) becomes

$$\begin{aligned}\mathcal{L} \;=\; & \left(\frac{i}{2}\bar{q}_w \overleftrightarrow{\partial}\, q_w - B\right)\theta_v - \frac{1}{2}\bar{q}_w q_w \delta_s + \frac{1}{2}\left(D_\mu\vec{\phi}\right)^2 \\ & + \frac{i}{2}\left[\bar{q}_w\gamma^\mu S(\partial_\mu S^\dagger)q_w + \bar{q}_w S^\dagger(\partial_\mu S)\gamma^\mu q_w\right]\theta_v \end{aligned} \tag{2.35}$$

After expanding the operators S and $S^\dagger$ as

$$\begin{aligned} S, S^\dagger \;&=\; \sum_{n=0}^{\infty}\left[\pm i\vec{\tau}\cdot\vec{\phi}\gamma_5/2f\right]^n/\,n! \\ &=\; \cos(\phi/2f) \pm i(\vec{\tau}\cdot\hat{\phi}\gamma_5)\sin(\phi/2f) \end{aligned} \tag{2.36}$$

we can find

$$\begin{aligned} S(\partial_\mu S^\dagger) \;=\; & -i\partial_\mu(\phi/f)(\hat{\phi}\cdot\vec{\tau}/2)\gamma_5 - i(\partial_\mu\hat{\phi}\cdot\vec{\tau}/2)\gamma_5\sin(\phi/f) \\ & -i\left(\cos(\phi/f)-1\right)(\hat{\phi}\times\partial_\mu\hat{\phi})\cdot\vec{\tau}/2 \end{aligned} \tag{2.37}$$

and

$$S^\dagger(\partial_\mu S) = i\partial_\mu(\phi/f)(\hat{\phi}\cdot\vec{\tau}/2)\gamma_5 + i(\partial_\mu\hat{\phi}\cdot\vec{\tau}/2)\gamma_5\sin(\phi/f) - i(\cos(\phi/f)-1)(\hat{\phi}\times\partial_\mu\hat{\phi})\cdot\vec{\tau}/2 \quad (2.38)$$

Recalling the definition of the covariant derivative of the pion field (2.23), we find

$$S(\partial_\mu S^\dagger) = -i\gamma_5(D_\mu\vec{\phi}/f)\cdot\vec{\tau}/2 - i(\cos(\phi/f)-1)(\hat{\phi}\times\partial_\mu\hat{\phi})\cdot\vec{\tau}/2 \quad (2.39)$$

and

$$S^\dagger(\partial_\mu S) = i\gamma_5(D_\mu\vec{\phi}/f)\cdot\vec{\tau}/2 - i(\cos(\phi/f)-1)(\hat{\phi}\times\partial_\mu\hat{\phi})\cdot\vec{\tau}/2 \quad (2.40)$$

Now, if we define the "covariant derivative" of the quark field as

$$D_\mu q_w = \partial_\mu q_w - i\left[\frac{\cos(\phi/f)-1}{2}\right]\vec{\tau}\cdot\left(\hat{\phi}\times\partial_\mu\hat{\phi}\right)q_w \quad (2.41)$$

After some algebraic manipulations, the transformed Lagrangian density finally becomes

$$\mathcal{L} = (\frac{i}{2}\bar{q}_w \overleftrightarrow{\not{D}}\, q_w - B)\theta_v - \frac{1}{2}\bar{q}_w q_w\delta_s + \frac{1}{2}\left(D_\mu\vec{\phi}\right)^2 + \frac{1}{2f}\bar{q}_w\gamma^\mu\gamma_5\vec{\tau}q_w\cdot(D_\mu\vec{\phi})\theta_v \quad (2.42)$$

Note in (2.42) the interaction term with a step function θ_v. We see that the original CBM Lagrangian (2.20) density which had surface coupling, has now been transformed into a *volume-coupling* Lagrangian density.

To determine S-wave pion scattering from a bag, we expand the Lagrangian density (2.42) to the lowest order in the pion field. The covariant derivative of the quark fields leads to an interaction term quadratic in the pion field:

$$\mathcal{L}_s = -\frac{1}{2f^2}[\bar{q}_w\gamma^0\vec{\tau}/2q_w]\cdot(\vec{\phi}\times\partial_0\vec{\phi})\theta_v \quad (2.43)$$

Notice in (2.43), the term in square brackets is the isospin density for the hadronic bag target, and the $(\vec{\phi}\times\partial_0\vec{\phi})$ term is the pion isospin density which is independent of x at the zero momentum. Therefore the S-wave pion-baryon interaction at threshold has the form

$$\begin{aligned} H_s &= -\int d^3x\mathcal{L}_s \\ &= \frac{1}{2f^2}\vec{t}\cdot\vec{t_\pi} \end{aligned} \tag{2.44}$$

which is completely equivalent to the W-T relation Eq. (2.31).

2.3 The S-Wave $\bar{K}N$ Interaction in the CBM

The Cloudy Bag Model has had some success in describing the low energy pion-nucleon interactions[20, 21, 25, 27]. Accordingly it is natural to think about applying this model to the kaon-nucleon and antikaon-nucleon interactions. One of the differences between kaon-nucleon and pion-nucleon system is the *strangeness* of the kaon. Consequently we need to include the strange quark in to the Cloudy Bag Model. The old SU(2)×SU(2) symmetry is no longer enough now, and so we use the SU(3)×SU(3) symmetry group for the kaon-nucleon and antikaon-nucleon interactions. Replacing the SU(2) Pauli matrices $\vec{\tau}$ in the volume coupling CBM Lagrangian (2.42) by the SU(3) Gell-Mann matrices $\vec{\lambda}$, we obtain the SU(3)×SU(3) CBM Lagrangian for both the antikaon-nucleon and the kaon-nucleon interactions[54, 35, 36]

$$\mathcal{L} = (\frac{i}{2}\bar{q}\overleftrightarrow{\not{D}}q - B)\theta_v - \frac{1}{2}\bar{q}q\delta_s + \frac{1}{2}(D_\mu\vec{\phi})^2 + \frac{1}{2f}\bar{q}\gamma^\mu\gamma_5\vec{\lambda}q\cdot(D_\mu\vec{\phi})\theta_v \tag{2.45}$$

In using (2.45) it is important to keep in mind that the quark fields q are in the SU(3) space instead of the SU(2) u and d quarks, that the meson fields $\vec{\phi}$ are

the SU(3) octet instead of the SU(2) pions, that B is the phenomenological "bag pressure", and that f is the meson decay constant. The volume θ function θ_v is 1 inside the bag volume and 0 outside, while δ_s is a surface δ-function. For a static, spherical bag, as used throughout this thesis, θ_v and δ_s reduce to the regular step function $\theta(R-r)$ and Dirac δ-function $\delta(R-r)$. The covariant derivatives of meson fields (2.23) and quark fields (2.41) are also generalized from SU(2) to SU(3)

$$D_\mu \vec{\phi} = (\partial_\mu \phi)\hat{\phi} + f \sin(\phi/f)\partial_\mu \hat{\phi} \tag{2.46}$$

$$D_\mu q = \partial_\mu q - \frac{i}{2}(\cos(\phi/f) - 1)\vec{\lambda} \cdot (\hat{\phi} \times \partial_\mu \hat{\phi})q \tag{2.47}$$

Here $\phi = |\vec{\phi}|$, $\hat{\phi} = \vec{\phi}/\phi$, and the SU(3) cross product is defined as

$$(\vec{A} \times \vec{B})_c = \sum_{a,b} f_{abc} A_a B_b \tag{2.48}$$

with f_{abc} the SU(3) structure constants.

If we take a limit of the meson field $\vec{\phi} = 0$, i.e. remove the explicit meson fields, the Lagrangian density (2.45) reduces to the original MIT bag model Lagrangian density (2.1). Since we know that the MIT bag model was quite successful in the static properties of baryons, we assume that we can perturbatively expand the field configuration around the MIT bag model, or equivalently, around $\vec{\phi} = 0$.

For small ϕ, keeping only terms up to order of ϕ^2, the covariant derivatives reduce to

$$D_\mu \vec{\phi} \approx \partial_\mu \vec{\phi} \tag{2.49}$$

and

$$D_\mu q \approx \partial_\mu q + \frac{i}{4f^2}\vec{\lambda} \cdot (\vec{\phi} \times \partial_\mu \vec{\phi})q \tag{2.50}$$

Substituting the covariant derivatives into Eq. (2.45), we get a linearized, volume coupling, SU(3)×SU(3) CBM Lagrangian density[35, 36]

$$\begin{aligned}\mathcal{L}_{CBM} &= \left(\frac{i}{2}\bar{q}\overleftrightarrow{\not\partial}q - B\right)\theta_v - \frac{1}{2}\bar{q}q\delta_s + \frac{1}{2}(\partial_\mu\vec{\phi})^2 \\ &+\frac{\theta_v}{2f}\bar{q}\gamma^\mu\gamma_5\vec{\lambda}q\cdot(\partial_\mu\vec{\phi}) - \frac{\theta_v}{(2f)^2}\bar{q}\gamma^\mu\vec{\lambda}\cdot(\vec{\phi}\times\partial_\mu\vec{\phi})q \qquad (2.51)\end{aligned}$$

Notice that the Lagrangian density (2.51) can be broken up into pieces:

$$\mathcal{L}_{CBM} = \mathcal{L}_{MIT} + \mathcal{L}_{KG} + \mathcal{L}_s + \mathcal{L}_c \qquad (2.52)$$

Here $\mathcal{L}_{MIT}$ is the free MIT bag Lagrangian given in Eq. (2.1), $\mathcal{L}_{KG}$ is the Klein-Gordon Lagrangian density for the free meson field,

$$\mathcal{L}_{KG} = \frac{1}{2}(\partial_\mu\vec{\phi})^2 \qquad (2.53)$$

and the s-channel and contact interaction Lagrangian densities are

$$\mathcal{L}_s = \frac{\theta_v}{2f}\bar{q}\gamma^\mu\gamma_5\vec{\lambda}q\cdot(\partial_\mu\vec{\phi}) \qquad (2.54)$$

$$\mathcal{L}_c = -\frac{\theta_v}{(2f)^2}\bar{q}\gamma^\mu\vec{\lambda}\cdot(\vec{\phi}\times\partial_\mu\vec{\phi})q \qquad (2.55)$$

As usual, the energy-momentum tensor $T^{\mu\nu}$ is defined as[55]

$$T^{\mu\nu} = \frac{\partial\mathcal{L}}{\partial(\partial_\mu q)}\partial^\nu q + \partial^\nu\bar{q}\frac{\partial\mathcal{L}}{\partial(\partial_\mu\bar{q})} + \frac{\partial\mathcal{L}}{\partial(\partial_\mu\vec{\phi})}\partial^\nu\vec{\phi} - g^{\mu\nu}\mathcal{L} \qquad (2.56)$$

and the Hamiltonian is obtained in the canonical way[20, 35, 36]

$$\hat{H} = \int d^3x\, T^{00}(x) = \hat{H}_{MIT} + \hat{H}_{KG} + \hat{H}_s + \hat{H}_c + \hat{H}_{nd} \qquad (2.57)$$

here $\hat{H}_{MIT}$ describes the free MIT bag, $\hat{H}_{KG}$ the free mesons, and $\hat{H}_{nd}$ is a "normal-dependent" term due to the derivative coupling interaction

$$\hat{H}_{nd} = -\frac{\theta_v}{2}\left(\frac{1}{4f^2}\bar{q}(\vec{\lambda}\times\vec{\phi})\gamma^0 q - \frac{1}{2f}\bar{q}\gamma^0\gamma_5\vec{\lambda}q\right)^2 \qquad (2.58)$$

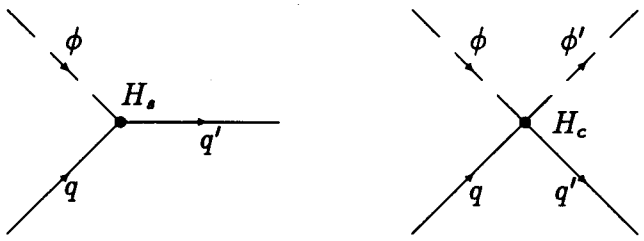

Figure 1. The Feynman diagram representation of the basic CBM interaction at the quark-meson level. The solid lines are quarks and the dashed lines are mesons.

Since the "normal-dependent" term is canceled in the S-matrix, we will not consider it further[1]. The two interaction Hamiltonian terms are

$$\hat{H}_s = -\int d^3x \frac{\theta_v}{2f}\bar{q}\gamma^\mu\gamma_5\vec{\lambda}q\partial_\mu\vec{\phi} \tag{2.59}$$

and

$$\hat{H}_c = \int d^3x \frac{\theta_v}{4f^2}\bar{q}\gamma^\mu\vec{\lambda}\cdot(\vec{\phi}\times\partial_\mu\vec{\phi})q \tag{2.60}$$

The s-channel and the contact interactions $\hat{H}_s$ and $\hat{H}_c$ are represented by the Feynman diagrams shown in Fig. 1.

For calculational purposes, it is convenient to project the CBM Hamiltonian onto the space of colorless baryon states[26, 24]:

$$H = \sum_{B_0,B_0'} B_0^\dagger\langle B_0|\hat{H}|B_0'\rangle B_0' = H_{MIT} + H_{KG} + H_s + H_c \tag{2.61}$$

where $B_0^\dagger$ and B_0' are the creation and annihilation operators for three quark bags of type B_0 and B_0', and $|B_0\rangle$ and $|B_0'\rangle$ are bare baryonic states.

[1]The interested reader can refer to page 242 of "Particles and Fields" by David Lurié, Interscience Publishers, New York, 1968.

The Fourier transformation of meson fields is written in terms of the meson annihilation and creation operators a_i and $a_i^\dagger$,

$$\phi_i(\mathbf{x}) = \int \frac{d^3k}{\sqrt{(2\pi)^3 2\omega_k}} [a_i(\mathbf{k})e^{i\mathbf{k}\cdot\mathbf{x}} + a_i^\dagger(\mathbf{k})e^{-i\mathbf{k}\cdot\mathbf{x}}] \tag{2.62}$$

The normal commutation relations are obeyed by a_i and $a_i^\dagger$

$$[a_i(\mathbf{k}), a_j^\dagger(\mathbf{k}')] = \delta_{ij}\,\delta^3(\mathbf{k}-\mathbf{k}') \tag{2.63}$$

$$[a_i(\mathbf{k}), a_j(\mathbf{k}')] = [a_i^\dagger(\mathbf{k}), a_j^\dagger(\mathbf{k}')] = 0 \tag{2.64}$$

With the help of Eq. (2.62), we now project the free Hamiltonian onto baryon-meson states

$$H_0 = H_{MIT} + H_{KG} = \sum_{B_0} m_{B_0} B_0^\dagger B_0 + \sum_i \int d^3k \omega_k a_i^\dagger(\mathbf{k}) a_i(\mathbf{k}) \tag{2.65}$$

where m_{B_0} is the MIT bare bag mass. In the next sections we project the interaction Hamiltonian onto the specific baryon and meson states.

2.3.1 The S-Wave H_s Interaction: $BM\Lambda^*_{1/2}$ Vertex

The s-channel interaction term $\hat{H}_s$ (2.59) has been studied in Ref. [35] for S-wave interactions and we now review that work. For convenience, we write the interaction term here as

$$\hat{H}_s = -\int d^3x \frac{\theta_v}{2f} \bar{q}\gamma^\mu\gamma_5\vec{\lambda}q\partial_\mu\vec{\phi} \tag{2.66}$$

From its structure, we see that $\hat{H}_s$ involves a quark transition from the initial state to the final state or absorbing or emitting a meson. From the baryon level, the corresponding interaction represents a baryon transition from its

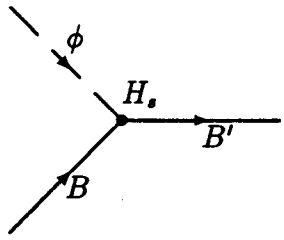

Figure 2. The Feynman diagram representation of a baryon absorbing a meson and transition from initial state B to final state B' via CBM interaction H_s.

initial state to its final state via the interaction with a single meson. Its Feynman diagram representation is shown in Fig. 2.

To project $\hat{H}_s$ onto the baryon space, we first integrate the right hand side of Eq. (2.66) by parts,

$$\begin{aligned}\hat{H}_s &= -\int d^3x \left\{ \partial_\mu \left[\frac{\theta_v}{2f} \bar{q}\gamma^\mu\gamma_5 \vec{\lambda} q \cdot \vec{\phi} \right] - \frac{(\partial_\mu \theta_v)}{2f} \bar{q}\gamma^\mu\gamma_5 \vec{\lambda} q \cdot \vec{\phi} \right. \\ &\quad \left. - \frac{\theta_v}{2f} \partial_\mu \left[\bar{q}\gamma^\mu\gamma_5 \vec{\lambda} q \right] \cdot \vec{\phi} \right\} \qquad (2.67)\end{aligned}$$

Using the Dirac equation for the MIT bag (2.11), we see that the last term vanishes. Applying the linear boundary condition (2.12), and the relation (2.3), the second term of $\hat{H}_s$ is transformed to

$$-\frac{(\partial_\mu \theta_v)}{2f} \bar{q}\gamma^\mu\gamma_5 \vec{\lambda} q \cdot \vec{\phi} = -\frac{i}{2f} \delta_s \bar{q}\gamma_5 \vec{\lambda} q \cdot \phi \qquad (2.68)$$

Notice that the space derivative part in the first term can be converted to a surface integration over a infinitely large surface, and so it too vanishes (the quark field is located inside the bag). We now eliminate the space derivative

part of $\hat{H}_s$ by rewriting it as

$$\hat{H}_s = \int d^3x \left[\frac{i}{2f} \bar{q}\gamma_5 \vec{\lambda} \cdot q\vec{\phi}\delta_s - \frac{\theta_v}{2f} \partial_0 (\bar{q}\gamma^0\gamma_5 \vec{\lambda} \cdot q\vec{\phi}) \right] \tag{2.69}$$

Before we continue any further, it is necessary to analyze the system in which we are interested. Our interest is in the $\bar{K}N$ system, including the $\Sigma\pi$, $\Lambda\pi$ channels to which it can couple.

$$\bar{K}N \rightarrow \begin{cases} \bar{K}N \\ \pi\Sigma \\ \pi\Lambda \end{cases} \tag{2.70}$$

In this system, the total strangeness equals -1 and the total angular momentum equals $1/2$ (we are looking at S-wave only at this point). For the energy range near $\bar{K}N$ threshold, the only possible intermediate state is $\Lambda^*_{1/2}$, and so we will calculate the vertex for the $BM \rightarrow \Lambda^*_{1/2}$ transition.

The bare state $\Lambda^*_{1/2}$ is considered as a bag containing three quarks, two in a $1s$ state and the third in a $1p_{1/2}$ state. The three quarks have flavor u, d, and s, and form a SU(3) singlet. The transition $BM \rightarrow \Lambda^*_{1/2}$ can be viewed as one quark absorbing a meson and being excited from the $1s$ state to $1p_{1/2}$ state.

For a MIT bag of radius R, the s quark wave function is[7]

$$q^M_{1s}(\mathbf{r},t) = \frac{N_s}{\sqrt{4\pi}} \begin{pmatrix} j_0(\omega_s r) \\ i j_1(\omega_s r)(\vec{\sigma}\cdot\hat{r}) \end{pmatrix} \theta(R-r) \chi^M_{\frac{1}{2}} e^{-i\omega_s t} \tag{2.71}$$

and $1p_{1/2}$ wave function is[7]

$$q^M_{1p_{\frac{1}{2}}}(\mathbf{r},t) = \frac{N_{p1}}{\sqrt{4\pi}} \begin{pmatrix} -j_1(\omega_{p1} r)(\vec{\sigma}\cdot\hat{r}) \\ i j_0(\omega_{p1} r) \end{pmatrix} \theta(R-r) \chi^M_{\frac{1}{2}} e^{-i\omega_{p1} t} \tag{2.72}$$

Here χ is the spin-flavor wave function of the quark, j_0 and j_1 are the spherical Bessel functions, $\omega_s \approx 2.04/R$, and $\omega_{p1} \approx 3.81/R$ are the quark energy level of $1s$ and $1p_{1/2}$ state, and N_s and N_{p1} are the normalization constants of respective quark wave functions.

We project the Hamiltonian $\hat{H}_s$ onto the baryon space:

$$H_s = \sum_{B_0} \left[B_0^\dagger \langle B_0 | \hat{H}_s | \Lambda_{1/2}^* \rangle \Lambda_{1/2}^* + \Lambda_{1/2}^{*\dagger} \langle \Lambda_{1/2}^* | \hat{H}_s | B_0 \rangle B_0 \right] \tag{2.73}$$

In (2.73) we keep only the terms related to the process in which we are interested, $BM \leftrightarrow \Lambda_{1/2}^*$. After substituting the Fourier transformation of the meson fields (2.62), we can write the Hamiltonian for $BM \leftrightarrow \Lambda_{1/2}^*$ as

$$H_s^{(s)} = \sum_i \int d^3k \left[V_{0i}^{(s)}(\mathbf{k}) a_i(\mathbf{k}) + V_{0i}^{(s)\dagger}(\mathbf{k}) a_i^\dagger(\mathbf{k}) \right] \tag{2.74}$$

where the superscript (s) labels the interaction as S-wave. The vertex function is given by

$$V_{0i}^{(s)}(\mathbf{k}) = \Lambda_{1/2}^{*\dagger} v_{\Lambda_{1/2}^* \alpha}(\mathbf{k}) B_0 \tag{2.75}$$

Applying the quark wave functions, we can evaluate the function $v_{\Lambda_{1/2}^* \alpha}(\mathbf{k})$ as[35]

$$\begin{aligned} v_{\Lambda_{1/2}^* \alpha}(\mathbf{k}) &= \langle \Lambda_{1/2}^* | H_s | \alpha \rangle \\ &= \frac{1}{2f} {}^{sf}\langle \Lambda_{1/2}^* | \lambda_i | B \rangle^{sf} \frac{u_{\Lambda_{1/2}^* \alpha}(k)}{\sqrt{(2\pi)^3 2\omega_k}} \end{aligned} \tag{2.76}$$

where α represents the channel BM_i, i labels the type of meson (including its charge state), ${}^{sf}\langle \Lambda_{1/2}^* | \lambda_i | B \rangle^{sf}$ represents the matrix element in spin-flavor space, and finally, the form factor function u is:

$$u_{\Lambda_{1/2}^* \alpha}(k)$$

α	$\bar{K}N$	$\pi\Sigma$	$\pi\Lambda$
λ_α^Λ	$\sqrt{2}$	$\sqrt{3}$	0

Table 1. The coupling constants λ_α^Λ for different channels α.

$$= -N_s N_{p1} 2R^2 j_0(\omega_s R) j_0(\omega_{p1} R) j_0(kR) + N_s N_{p1}(\omega_k + \omega_s - \omega_{p1}) \times \int_0^R dr\, r^2 \left[j_0(\omega_s r) j_0(\omega_{p1} r) + j_1(\omega_s r) j_1(\omega_{p1} r) \right] j_0(kr) \tag{2.77}$$

The Wigner-Eckart theorem tells us that the spin-flavor matrix elements are

$$^{sf}\langle \Lambda^*_{1/2} | \lambda_i | B \rangle^{sf} = \lambda_\alpha^\Lambda \langle I_B i_B; I_M i_M | I_B I_M; 00 \rangle \tag{2.78}$$

where the bracket on the right-hand side is a Clebsch-Gordan coefficient, and the coupling constants λ_α^Λ can be calculated by using the SU(6) quark wave function[35, 57]. The values of these coupling constants are listed in the Table 1.

2.3.2 The S-Wave H_c Interaction: $BMB'M'$ Vertex

The contact interaction H_c (2.60) has also been studied in Ref. [35] for the S-wave $\bar{K}N$ interactions. We review this interaction term now. We start with the interaction Hamiltonian:

$$\hat{H}_c = \int d^3x \frac{\theta_v}{4f^2} \bar{q} \gamma^\mu \vec{\lambda} \cdot (\vec{\phi} \times \partial_\mu \vec{\phi}) q \tag{2.79}$$

The structure of this Hamiltonian $\hat{H}_c$ shows a quark making a transition from its initial state to the final state by absorbing a meson and then emitting another one. At the baryon level, we are studying the process $BM \to B'M'$.

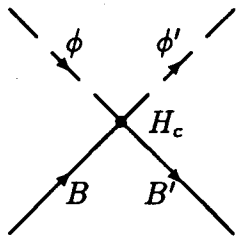

Figure 3. The Feynman diagram representation of a baryon absorbing a meson and emitting another one while transition from initial state B to final state B' via the CBM interaction H_c.

This corresponds to a baryon transition from one state to the other by absorbing a meson and emitting another, as shown in Fig. 3. Because the baryons in the initial and the final states belong to the octet, the quarks in these baryons are all in $1s$ state. Thus the quarks in the process must have the $1s$ state as their initial and final state.

For S-wave $BM \to B'M'$ scattering, the spatial derivative part of the interaction $\hat{H}_c$ vanishes, and only the time derivative part contributes. Substituting the Fourier expansion of meson fields (2.62), we obtain the interaction Hamiltonian $\hat{H}_c$ for the transition $BM \to B'M'$:

$$H_c = \sum_{i,j} \int d^3k \, V_{0ij}(\mathbf{k}', \mathbf{k}) a_i^\dagger(\mathbf{k}') a_j(\mathbf{k}) \tag{2.80}$$

Here the vertex function is given by

$$V_{0ij}(\mathbf{k}', \mathbf{k}) = \sum_{B_0, B_0'} B_0'^\dagger v^c_{\beta\alpha}(\mathbf{k}', \mathbf{k}) B_0 \tag{2.81}$$

With the $1s$ quark wavefunction (2.71), we have[35]

$$v^c_{\beta\alpha}(\mathbf{k}',\mathbf{k}) = \frac{1}{2f^2}{}^{sf}\langle B'| - \frac{i}{2} f_{j i' i} \lambda_j |B\rangle^{sf} \frac{u^c_{\beta\alpha}(k',k)}{\sqrt{(2\pi)^3\omega'(k')}\sqrt{(2\pi)^3\omega(k)}} \tag{2.82}$$

and so the form factor is

$$u^c_{\beta\alpha}(k',k) = N_s^2 \left[\omega(k) + \omega'(k')\right] \int_0^R dr\, r^2 \left[j_0^2(\omega_s r) + j_1^2(\omega_s r)\right] j_0(kr) j_0(k'r) \tag{2.83}$$

The spin-flavor matrix elements in Eq (2.82) are reduced by the Wigner-Eckart theorem:

$$\begin{aligned} {}^{sf}\langle B| - \frac{i}{2} f_{j i' i} \lambda_j |B\rangle^{sf} = \\ \sum_I \lambda^{t,I}_{\beta\alpha} \langle I_{B'} i_{B'}; I_{M'} i_{M'} | I_{B'} I_{M'}; I0\rangle \langle I_B i_B; I_M i_M | I_B I_M; I0\rangle \end{aligned} \tag{2.84}$$

The coupling constants $\lambda^{t,I}_{\beta\alpha}$ are then calculated with the help of the explicit form of the SU(6) wavefunction of the baryon octet[57]. The values of these coupling constants are listed in the Table 2[35]

2.4 The P- and D-Wave $\bar{K}N$ Interactions in the CBM

Part of the original work in this thesis is the extension of the CBM $\bar{K}N$ interaction from S-wave[35] to P- and D-wave. Although the P- and D-wave CBM has been studied for the KN interactions, and there is some similarities between KN and $\bar{K}N$ contact interaction terms H_c, there are more differences than similarities. First of all, the physics of these two system are very different. The KN interaction is relatively weak at the threshold energy, while the $\bar{K}N$ interaction is much stronger. In fact the existence of resonances in the threshold energy range, leads to new set of diagrams (processes) possible for antikaons.

	$\lambda^{t,I}_{\beta\alpha}$					
	$I=0$			$I=1$		
	$\bar{K}N$	$\pi\Sigma$	$\pi\Lambda$	$\bar{K}N$	$\pi\Sigma$	$\pi\Lambda$
$\bar{K}N$	$-\frac{3}{2}$	$-\frac{\sqrt{6}}{4}$	0	$-\frac{1}{2}$	$-\frac{1}{2}$	$\frac{\sqrt{6}}{4}$
$\pi\Sigma$	$-\frac{\sqrt{6}}{4}$	-2	0	$-\frac{1}{2}$	-1	0
$\pi\Lambda$	0	0	0	$\frac{\sqrt{6}}{4}$	0	0

Table 2. The coupling constants $\lambda^{t,I}_{\beta\alpha}$ for different incoming and outgoing channels α and β.

2.4.1 The P-Wave H_s Interaction: $BM\Sigma^*_{3/2}$ Vertex

For the energy range we are interested in, the only possible intermediate particle for the P-wave $\bar{K}N$ H_s interaction is the neutral $\Lambda^*_{3/2}$. The $\Sigma^*_{3/2}$ is an excited state of the Σ hyperon. This excited sigma has spin $\frac{3}{2}$, positive parity, and mass 1385 MeV. Only the neutral member $\Sigma^{*0}_{3/2}$ of the triplet couples to the $\bar{K}N$ system. The bare state of the $\Sigma^*_{3/2}$ is assumed to be a member of the $\underline{10}$ of SU(3). The quark constituent of the bare neutral state is uds, with the quarks staying in the $1s$ state. The transition $BM \rightarrow \Sigma^*_{3/2}$ can be viewed as one quark changing its state (including the flavor, spin) to another after absorbing a meson.

Similar to what we have seen previously in the case of $BM \leftrightarrow \Lambda^*_{1/2}$ H_s interaction, with the help of the Fourier transformation (2.62) of the meson

fields, we can project $\hat{H}_s$ (2.69) to the baryon space:

$$H_s^{(p)} = \sum_i \int d^3k \, [V_{0i}^{(p)}(\mathbf{k}) a_i(\mathbf{k}) + V_{0i}^{(p)\dagger}(\mathbf{k}) a_i^\dagger(\mathbf{k})] \tag{2.85}$$

where the vertex function is

$$V_{0i}^{(p)}(\mathbf{k}) = \Sigma_{3/2}^{0*\dagger} v_{\Sigma_{3/2}^* \alpha}(\mathbf{k}) B_0 = \Sigma_{3/2}^{0*\dagger} \langle \Sigma_{3/2}^* | H_s | \alpha \rangle B_0 \tag{2.86}$$

The superscript (p) in the above equation indicates the P-wave interaction.

The vertex function $v_{\Sigma_{3/2}^* \alpha}(\mathbf{k})$ in (2.86) can be written explicitly as

$$v_{\Sigma_{3/2}^* \alpha}(\mathbf{k}) = \frac{1}{2f} \int \frac{d^3x}{\sqrt{(2\pi)^3 2\omega_k}} e^{i\mathbf{k}\cdot\mathbf{r}} \langle \Sigma_{3/2}^* | i\delta_s \bar{q}_{1s} \gamma_5 \lambda_i q_{1s} + i\theta_v \omega_k \bar{q}_{1s} \gamma^0 \gamma_5 \lambda_i q_{1s} | B \rangle \tag{2.87}$$

Here we have substituted the $1s$ quark wave function since the quark initial and final are both $1s$. Notice in (2.87) that $\bar{q}_{1s}\gamma^0\gamma_5 q_{1s} = 0$, so the second term vanishes for the $BM \to \Sigma_{3/2}^*$ process. After using the $1s$ quark wave function (2.71), we obtain

$$v_{\Sigma_{3/2}^* \alpha}(\mathbf{k}) = \frac{1}{2f} \frac{N_s^2}{4\pi} (-2) \int \frac{d^3x}{\sqrt{(2\pi)^3 2\omega_k}} e^{i\mathbf{k}\cdot\mathbf{r}} j_0(\omega_s r) j_1(\omega_s r) \delta_s{}^{sf} \langle \Sigma_{3/2}^* | \lambda_i \boldsymbol{\sigma} \cdot \hat{r} | B \rangle^{sf} \tag{2.88}$$

To simplify the vertex function, we start with the partial wave expansion of the plane wave

$$e^{i\mathbf{k}\cdot\mathbf{r}} = 4\pi \sum_{LM} i^L j_L(kr) Y_{LM}^*(\hat{k}) Y_{LM}(\hat{r}) \tag{2.89}$$

and the relation

$$\boldsymbol{\sigma} \cdot \hat{r} = \sqrt{\frac{4\pi}{3}} \sum_q Y_{1q}^*(\hat{r}) \sigma_q \tag{2.90}$$

where σ_q are defined as

$$\sigma_{\pm 1} = \mp\frac{1}{\sqrt{2}}(\sigma_x \pm \sigma_y) \tag{2.91}$$

$$\sigma_0 = \sigma_z \tag{2.92}$$

Substitution yields:

$$v_{\Sigma^*_{3/2}\alpha}(\mathbf{k}) = \frac{1}{2f}\frac{N_s^2}{4\pi}\frac{-2}{\sqrt{(2\pi)^3 2\omega_k}}\int d^3x\, \delta_s 4\pi \sum_{LM} i^L j_L(kr) Y^*_{LM}(\hat{k}) Y_{LM}(\hat{r})$$
$$\times j_0(\omega_s r) j_1(\omega_s r) \sum_q \sqrt{\frac{4\pi}{3}} Y^*_{1q}(\hat{r})\, {}^{sf}\langle \Sigma^*_{3/2}|\lambda_i \sigma_q|B\rangle^{sf} \tag{2.93}$$

Using the fact that the surface δ-function δ_s is just $\delta(R-r)$, and integrating over the solid angle, we find the vertex function:

$$v_{\Sigma^*_{3/2}\alpha}(\mathbf{k}) = \frac{1}{2f}\frac{-2iN_s^2R^2}{\sqrt{(2\pi)^3 2\omega_k}} \sum_q Y^*_{1q}(\hat{k}) j_0(\omega_s R) j_1(\omega_s R) j_1(kR)\, {}^{sf}\langle \Sigma^*_{3/2}|\lambda_i \sigma_q|B\rangle^{sf} \tag{2.94}$$

At this point, it is appropriate to add in the spin indices we have previously ignored. Let the $\Sigma^*_{3/2}$ has spin μ, and baryon B has spin ν, then the Wigner-Eckart theorem tells us

$${}^{sf}\langle \Sigma^*_{3/2}(\mu)|\lambda_i \sigma_q|B(\nu)\rangle^{sf} = \lambda^\Sigma_\alpha \langle \tfrac{1}{2}\nu; 1q|\tfrac{1}{2}1; \tfrac{3}{2}\mu\rangle \langle I_B i_B; I_M i_M|I_B I_M; 10\rangle \tag{2.95}$$

Substituting this back into the expression for $v_{\Sigma^*_{3/2}\alpha}(\mathbf{k})$, we get the final expression for the vertex function

$$v_{\Sigma^*_{3/2}\alpha}(\mathbf{k};\mu,\nu) = \frac{\lambda^\Sigma_\alpha}{2f}\frac{(-2iN_s^2R^2)}{\sqrt{(2\pi)^3 2\omega_k}}\sqrt{\frac{4\pi}{3}} \langle \tfrac{1}{2}\nu; 1q|\tfrac{1}{2}1; \tfrac{3}{2}\mu\rangle \langle I_B i_B; I_M i_M|I_B I_M; 10\rangle$$
$$\times Y^*_{1(\mu-\nu)}(\hat{k}) j_0(\omega_s R) j_1(\omega_s R) j_1(kR) \tag{2.96}$$

α	$\bar{K}N$	$\pi\Sigma$	$\pi\Lambda$
λ_α^Σ	$\sqrt{\frac{8}{3}}$	$-\sqrt{\frac{8}{3}}$	2

Table 3. The coupling constants λ_α^Σ for different channels α.

The coupling constants λ_α^Σ in (2.96) are calculated using the explicit SU(6) spin-flavor wave function of the baryons. In practice, they are calculated using a Mathematica^{TM} symbolic manipulation program package we have developed specifically for this purpose and verified with tedious hand calculation for several cases. The values of these coupling constants are listed in Table 3.

2.4.2 The D-Wave H_s Interaction: $BM\Lambda_{3/2}^*$ Vertex

The $\Lambda_{3/2}^*(1520)$ is an excite state of the Λ hyperon with -1 strangeness, 0 charge and negative parity. With spin 3/2, the $\Lambda_{3/2}^*$ couples to the $\bar{K}N$ system in the D-wave interaction. It is a special H_s interaction of the CBM Hamiltonian and is added in to others. The bare state of $\Lambda_{3/2}^*$ is composed of u, d, and s quarks and is assumed to be a SU(3) singlet with total spin 3/2. The space wave function configuration of the quarks is $1s^2 1p_{3/2}$. Correspondingly the transition $BM \leftrightarrow \Lambda_{3/2}^*$ can be viewed as one quark in B absorbing a meson and changing its state from $1s$ to the $1p_{3/2}$ one of the $\Lambda_{3/2}^*$ (or vise versa). Flavor may also change during the transition.

As in the S and P wave case, we project the Hamiltonian $\hat{H}_s$

$$H_s^{(d)} = \sum_i \int d^3k \, [V_{0i}^{(d)}(\mathbf{k}) a_i(\mathbf{k}) + V_{0i}^{(d)\dagger}(\mathbf{k}) a_i^\dagger(\mathbf{k})] \tag{2.97}$$

with the vertex function

$$V_{0i}^{(d)}(\mathbf{k}) = \Lambda_{3/2}^{*\dagger} v_{\Lambda_{3/2}^* \alpha}(\mathbf{k}) B_0 = \Lambda_{3/2}^{*\dagger} \langle \Lambda_{3/2}^* | H_s | \alpha \rangle B_0 \tag{2.98}$$

The superscript (d) indicates the interaction is in D-wave.

The vertex function $v_{\Lambda_{3/2}^* \alpha}(\mathbf{k})$ can be written explicitly as

$$v_{\Lambda_{3/2}^* \alpha}(\mathbf{k}) = \frac{i}{2f} \int \frac{d^3x}{\sqrt{(2\pi)^3 2\omega_k}} e^{i\mathbf{k}\cdot\mathbf{r}} \times {}^{sf}\langle \Lambda_{3/2}^* | \delta_s \bar{q}_{1p_{3/2}} \gamma_5 \lambda_i q_{1s} + (\omega_s + \omega_k - \omega_{p3}) \bar{q}_{1p_{3/2}} \gamma^0 \gamma_5 \lambda_i q_{1s} | B \rangle^{sf} \tag{2.99}$$

where we have used the $1s$ and $1p_{3/2}$ quark wave function as the initial and final wave function. The $1p_{3/2}$ quark wave function is given in Ref [7], and we rewrite it here for convenience,

$$q_{1p_{3/2}}^M(\mathbf{r}, t) = N_{p3} \begin{pmatrix} j_1(\omega_{p3} r) \\ i j_2(\omega_{p3} r)(\boldsymbol{\sigma} \cdot \hat{r}) \end{pmatrix} \theta(R - r) e^{-i\omega_{p3} t} \mathcal{Y}_{1\frac{3}{2}}^M(\theta, \phi) \tag{2.100}$$

where $\mathcal{Y}$ is the spin-angle function, N_{p3} is the normalization constant and $\omega_{p3} \approx 3.20/R$ is the energy level of the $1p_{3/2}$ state.

The spin-angle function in (2.100) can be expanded in terms of spherical harmonics and 2-component spinors

$$\mathcal{Y}_{1\frac{3}{2}}^M = \sum_m \langle 1m; \tfrac{1}{2} M - m | 1\tfrac{1}{2}; \tfrac{3}{2} M \rangle Y_{1m} \chi^{M-m} \tag{2.101}$$

Accordingly, since $\Lambda_{1/2}^*$ and $\Lambda_{3/2}^*$ share the same SU(3) flavor function, we expand the $\Lambda_{3/2}^*$ spin-flavor wave function as

$$|\Lambda_{3/2}^*\rangle^{sf} = \sum_m \langle 1m; \tfrac{1}{2} M - m | 1\tfrac{1}{2}; \tfrac{3}{2} M \rangle Y_{1m} |\Lambda_{1/2}^*\rangle^{sf} \tag{2.102}$$

We now further calculate the vertex function of $BM \to \Lambda^*_{3/2}$ with the spin-flavor wave function of $\Lambda^*_{1/2}$:

$$
\begin{aligned}
v_{\Lambda^*_{3/2}\alpha}(\mathbf{k};\mu,\nu) &= \langle \Lambda^*_{3/2}(\mu)|V_{0i}^{(d)}|B(\nu)\rangle \\
&= -\frac{1}{2f}\frac{1}{\sqrt{3}}\frac{4\pi N_s N_{p3}}{\sqrt{(2\pi)^3 2\omega_k}}\sum_{mq}\sum_{LM} i^L(-1)^q\langle 1m;\tfrac{1}{2}\mu-m|1\tfrac{1}{2};\tfrac{3}{2}\mu\rangle Y^*_{LM}(\hat{k}) \\
&\quad \times {}^{sf}\langle \Lambda^*_{1/2}(\mu-m)|\lambda_i\sigma_q|B(\nu)\rangle^{sf}\int d^3x Y_{1-q}(\hat{r})Y^*_{1m}(\hat{r})Y_{LM}(\hat{r})j_L(kr) \\
&\quad \times \{\delta_s[j_1(\omega_s r)j_1(\omega_{p3}r)+j_0(\omega_s r)j_2(\omega_{p3}r)] \\
&\qquad + \theta_v(\omega_s+\omega_k-\omega_{p3})[j_1(\omega_s r)j_1(\omega_{p3}r)-j_0(\omega_s r)j_2(\omega_{p3}r)]\} \qquad (2.103)
\end{aligned}
$$

Completing the integral, and using the relations

$$j_0(\omega_s R) = j_1(\omega_s R) \qquad (2.104)$$

$$j_2(\omega_{p3}R) = j_1(\omega_{p3}R) \qquad (2.105)$$

we find

$$
\begin{aligned}
&v_{\Lambda^*_{3/2}\alpha}(\mathbf{k};\mu,\nu) \\
&= \frac{1}{2f}\sqrt{\frac{4\pi}{3}}\frac{1}{\sqrt{(2\pi)^3 2\omega_k}}\sum_{LM}\sum_{mq}(-1)^m i^L\sqrt{2L+1}Y^*_{LM}(\hat{k})u^{(L)}_{\Lambda^*_{3/2}\alpha}(k) \\
&\quad \times {}^{sf}\langle \Lambda^*_{1/2}(\mu-m)|\lambda_i\sigma_q|B(\nu)\rangle^{sf}\langle L0;10|L1;10\rangle \\
&\quad \times \langle 1m;\tfrac{1}{2}\mu-m|1\tfrac{1}{2};\tfrac{3}{2}\mu\rangle\langle LM;1-m|L1;1q\rangle \qquad (2.106)
\end{aligned}
$$

The form factor function $u(k)$ is defined as

$$
\begin{aligned}
u^{(L)}_{\Lambda^*_{3/2}\alpha}(k) &= -N_s N_{p3}2R^2 j_0(\omega_s R)j_1(\omega_{p3}R)j_L(kR) \\
&\quad -N_s N_{p3}(\omega_s+\omega_k-\omega_{p3}) \\
&\quad \times \int_0^R dr\, r^2 j_L(kr)[j_1(\omega_s r)j_1(\omega_{p3}r)-j_0(\omega_s r)j_2(\omega_{p3}r)] \qquad (2.107)
\end{aligned}
$$

We now apply the Wigner-Eckart theorem to both isospin and spin, in which case we write

$$\begin{aligned} &{}^{sf}\langle \Lambda^*_{1/2}(\mu - m)|\lambda_i \sigma_q|B(\nu)\rangle^{sf} \\ &= -\sqrt{3}\,\lambda^{\Lambda}_{\alpha}\langle \tfrac{1}{2}\nu; 1q|\tfrac{1}{2}1; \tfrac{1}{2}\mu - m\rangle \langle I_B i_B; I_M i_M|I_B I_M; 00\rangle \end{aligned} \tag{2.108}$$

where $\lambda^{\Lambda}_{\alpha}$ is calculated using explicit SU(6) quark spin-flavor wave functions. We explicitly calculated the λ's with the Mathematica package and verified several elements by hand calculation. The coupling constants $\lambda^{\Lambda}_{\alpha}$ are the same as in the $BM \leftrightarrow \Lambda^*_{1/2}$ case, so we adopted the same notation for them:

$$\begin{aligned} v_{\Lambda^*_{3/2}\alpha}(\mathbf{k};\mu,\nu) &= \frac{\lambda^{\Lambda}_{\alpha}}{2f}\langle I_B i_B; I_M i_M|I_B I_M; 00\rangle \sqrt{\frac{4\pi}{(2\pi)^3 2\omega_k}} \\ &\quad \times \sum_{LM} i^L \sqrt{2L+1}\, Y^*_{LM}(\hat{k})\langle L0; 10|L1; 10\rangle u^L_{\Lambda^*_{3/2}\alpha}(k) \\ &\quad \times \sum_{mq}(-1)^m \langle 1m; \tfrac{1}{2}\mu - m|1\tfrac{1}{2}; \tfrac{3}{2}\mu\rangle \langle LM; 1-m|L1; 1q\rangle \\ &\quad \times \langle \tfrac{1}{2}\nu; 1q|\tfrac{1}{2}1; \tfrac{1}{2}\mu - m\rangle \end{aligned} \tag{2.109}$$

After some lengthy algebraic manipulation with the Clebsch-Gordan coefficients and $6j$ symbols, we obtained

$$\begin{aligned} &\sum_{mq}(-1)^m \langle 1m; \tfrac{1}{2}\mu - m|1\tfrac{1}{2}; \tfrac{3}{2}\mu\rangle \langle LM; 1-m|L1; 1q\rangle \\ &\qquad \times \langle \tfrac{1}{2}\nu; 1q|\tfrac{1}{2}1; \tfrac{1}{2}\mu - m\rangle \\ &= -\sqrt{6}\begin{Bmatrix} \frac{1}{2} & 1 & \frac{1}{2} \\ 1 & \frac{3}{2} & L \end{Bmatrix} \delta_{M(\mu-\nu)}\langle \tfrac{1}{2}\nu; LM|\tfrac{1}{2}L; \tfrac{3}{2}\mu\rangle \end{aligned} \tag{2.110}$$

where the object with big braces is a $6j$ symbol. Notice that

$$\langle \tfrac{1}{2}\nu; LM|\tfrac{1}{2}L; \tfrac{3}{2}\mu\rangle \langle L0; 10|L1; 10\rangle = 0 \quad \text{for } L \neq 2 \tag{2.111}$$

and that

$$\left\{ \begin{array}{ccc} \frac{1}{2} & 1 & \frac{1}{2} \\ 1 & \frac{3}{2} & 2 \end{array} \right\} = \frac{1}{2\sqrt{3}} \tag{2.112}$$

After these manipulations we finally obtain a clean expression for the vertex function:

$$\begin{aligned} v_{\Lambda^*_{3/2}\alpha}(\mathbf{k};\mu,\nu) &= \frac{\lambda_\alpha}{2f}\langle I_B i_B; I_M i_M | I_B I_M; 00\rangle \langle \tfrac{1}{2}\nu; 2\mu-\nu | \tfrac{1}{2}2; \tfrac{3}{2}\mu\rangle \\ &\quad \times\sqrt{4\pi}\, Y^*_{2(\mu-\nu)}(\hat{k}) \frac{u^{(2)}_{\Lambda^*_{3/2}\alpha}(k)}{\sqrt{(2\pi)^3 2\omega_k}} \end{aligned} \tag{2.113}$$

Here $u^{(2)}_{\Lambda^*_{3/2}\alpha}(k)$ is defined in Eq. (2.107) and the coupling constant λ_α is listed in Table 1.

2.4.3 The P- and D-Wave H_c Interaction: $BMB'M'$ Vertex

While the particles involved in the P and D-wave process $BM \to B'M'$ are no different from the ones in S-wave, the vertex function now gets much more complicated due to spin and angular momenta. For example, we showed in Subsection 2.3.2, that the spatial derivative part of the $\hat{H}_c$ vanishes in S-wave, yet this is no longer true in the P- and D-wave. To make the formulas more clear, we separate the time part and the spatial parts. Using the same technique we used in the S-wave case, we can project the Hamiltonian onto the baryon space:

$$H_c = H_{ct} + H_{cs} = \sum_{i,j} \int d^3k \, [V^{ct}_{0ij} + V^{cs}_{0ij}] a^\dagger_i(\mathbf{k}') a_j(\mathbf{k}) \tag{2.114}$$

$$V_{0ij}^{ct} = \sum_{B_0,B_0'} B_0'^{\dagger} v_{\beta\alpha}^{ct}(\mathbf{k}',\mathbf{k}) B_0 \tag{2.115}$$

$$V_{0ij}^{cs} = \sum_{B_0,B_0'} B_0'^{\dagger} v_{\beta\alpha}^{cs}(\mathbf{k}',\mathbf{k}) B_0 \tag{2.116}$$

where $v_{\beta\alpha}^{ct}(\mathbf{k}',\mathbf{k})$ and $v_{\beta\alpha}^{cs}(\mathbf{k}',\mathbf{k})$ stand for the vertex functions corresponding to the *time* and *spatial* derivative parts of the H_c interaction.

We start from the simpler one, the time derivative part $v_{\beta\alpha}^{ct}(\mathbf{k}',\mathbf{k})$ and write it out explicitly

$$v_{\beta\alpha}^{ct}(\mathbf{k}',\mathbf{k}) = \frac{1}{4f^2}\frac{-i}{\sqrt{(2\pi)^3 2\omega_k}\sqrt{(2\pi)^3 2\omega_{k'}}} \times {}^{sf}\langle B'| \int d^3x \theta_v \bar{q}_{1s} f_{i'ij}\lambda_j(\omega_k+\omega_{k'})\gamma^0 e^{i(\mathbf{k}-\mathbf{k}')\cdot\mathbf{r}} q_{1s}|B\rangle^{sf} \tag{2.117}$$

Notice that the initial and final quarks are in are $1s$ state. Using the $1s$ state quark wavefunction (2.71) and the partial-wave expansion of plane wave (2.89), we have

$$\begin{aligned} & v_{\beta\alpha}^{ct}(\mathbf{k}',\mathbf{k}) \\ &= \frac{1}{4f^2}\frac{N_s^2}{4\pi}\frac{-i(\omega_k+\omega_{k'})}{\sqrt{(2\pi)^3 2\omega_k}\sqrt{(2\pi)^3 2\omega_{k'}}} \\ &\quad \times {}^{sf}\langle B'|f_{i'ij}\lambda_j|B\rangle^{sf} \int d^3x\, \theta_v [j_0^2(\omega_s r)+j_1^2(\omega_s r)] \\ &\quad \times \sum_{lm}\sum_{l'm'} i^l (i^*)^{l'} j_l(kr) j_{l'}(k'r) Y_{lm}^*(\hat{k}) Y_{l'm'}(\hat{k}') Y_{l'm'}^*(\hat{r}) Y_{lm}(\hat{r}) \end{aligned} \tag{2.118}$$

Integrating over the solid angle produces

$$\begin{aligned} & v_{\beta\alpha}^{ct}(\mathbf{k}',\mathbf{k}) \\ &= \frac{1}{2f^2}\frac{(\omega_k+\omega_{k'})}{2\pi^2\sqrt{2\omega_k 2\omega_{k'}}} {}^{sf}\langle B'| -\frac{i}{2} f_{i'ij}\lambda_j |B\rangle^{sf} \sum_{lm} Y_{lm}^*(\hat{k}) Y_{lm}(\hat{k}') \\ &\quad \times N_s^2 \int_0^R dr\, r^2 [j_0^2(\omega_s r)+j_1^2(\omega_s r)] j_l(kr) j_l(k'r) \end{aligned} \tag{2.119}$$

We have already seen the spin-flavor matrix elements in Subsection 2.3.2. They can be expressed as

$$\begin{aligned} &{}^{sf}\langle B'| -\frac{i}{2} f_{i'ij}\lambda_j |B\rangle^{sf} \\ &= \sum_I \lambda^{t,I}_{\beta\alpha} \langle I_B i_B; I_M i_M | I_B I_M; I0\rangle \langle I_{B'} i_{B'}; I_{M'} i_{M'} | I_{B'} I_{M'}; I0\rangle \end{aligned} \quad (2.120)$$

with the values of $\lambda^{t,I}_{\beta\alpha}$ listed in Table 2. Finally we put the spin indices back in, which merely add another $\delta_{\mu'\mu}$ on the expression of $v^{ct}_{\beta\alpha}(\mathbf{k}', \mathbf{k})$

$$\begin{aligned} v^{ct}_{\beta\alpha}(\mathbf{k}'\mu', \mathbf{k}\mu) &= \delta_{\mu'\mu} \frac{(\omega_k + \omega_{k'})}{2\pi^2 \sqrt{2\omega_k 2\omega_{k'}}} \sum_I \frac{\lambda^{t,I}_{\beta\alpha}}{2f^2} \sum_{lm} Y^*_{lm}(\hat{k}) Y_{lm}(\hat{k}') \\ &\quad \times \langle I_B i_B; I_M i_M | I_B I_M; I0\rangle \langle I_{B'} i_{B'}; I_{M'} i_{M'} | I_{B'} I_{M'}; I0\rangle \\ &\quad \times N_s^2 \int_0^R dr\, r^2 [j_0^2(\omega_s r) + j_1^2(\omega_s r)] j_l(kr) j_l(k'r) \end{aligned} \quad (2.121)$$

The angular momentum makes the derivation of $v^{cs}_{\beta\alpha}(\mathbf{k}', \mathbf{k})$ a little more complicated. We first write

$$\begin{aligned} &v^{cs}_{\beta\alpha}(\mathbf{k}', \mathbf{k}) \\ &= -\frac{1}{4f^2} \frac{-i}{\sqrt{(2\pi)^3 2\omega_k}\sqrt{(2\pi)^3 2\omega_{k'}}} \\ &\quad \times {}^{sf}\langle B'| \int d^3x\, \theta_v \bar{q}_{1s} f_{i'ij} \lambda_j (\mathbf{k}' + \mathbf{k}) \cdot \boldsymbol{\gamma} e^{i(\mathbf{k}-\mathbf{k}')\cdot\mathbf{r}} q_{1s} |B\rangle^{sf} \end{aligned} \quad (2.122)$$

where q_{1s} and $\bar{q_1}_s$ are the initial and final quark wave functions involved in the process. Substituting in the explicit form of q_{1s} (2.71), and using the identity

$$[\boldsymbol{\sigma}\cdot\mathbf{A}, \boldsymbol{\sigma}\cdot\mathbf{B}] = 2i\boldsymbol{\sigma}\cdot(\mathbf{A}\times\mathbf{B}) \quad (2.123)$$

we reduce $v^{cs}_{\beta\alpha}(\mathbf{k}', \mathbf{k})$ to

$$v^{cs}_{\beta\alpha}(\mathbf{k}', \mathbf{k}) = \frac{1}{2f^2} \frac{i}{\sqrt{(2\pi)^3 2\omega_k}\sqrt{(2\pi)^3 2\omega_{k'}}}$$

$$\times \frac{N_s^2}{4\pi}\int_0^R dr d\Omega_r\, r j_0(\omega_s r) j_1(\omega_s r)\, {}^{sf}\langle B'|f_{i'ij}\lambda_j\sigma|B\rangle^{sf}$$
$$\cdot\left[e^{-i\mathbf{k}'\cdot\mathbf{r}}(\mathbf{r}\times\mathbf{k})e^{i\mathbf{k}\cdot\mathbf{r}} + (\mathbf{r}\times\mathbf{k}')e^{-i\mathbf{k}'\cdot\mathbf{r}}e^{i\mathbf{k}\cdot\mathbf{r}}\right] \qquad (2.124)$$

Notice that $\mathbf{r}\times\mathbf{k}$ and $\mathbf{r}\times\mathbf{k}'$ are just the angular momentum operators acting on $e^{i\mathbf{k}\cdot\mathbf{r}}$ and $e^{i\mathbf{k}\cdot\mathbf{r}}$. So, by applying the partial wave expansion (2.89), we obtain

$$\begin{aligned} v^{cs}_{\beta\alpha}(\mathbf{k}',\mathbf{k}) &= \frac{1}{2f^2}\frac{8\pi i N_s^2}{\sqrt{(2\pi)^3 2\omega_k}\sqrt{(2\pi)^3 2\omega_{k'}}} \\ &\times \sum_{lmm'} Y^*_{lm}(\hat{k})Y_{lm'}(\hat{k}')\int_0^R dr\, j_0(\omega_s r) j_1(\omega_s r) j_l(kr) j_l(k'r) \\ &\times {}^{sf}\langle B'|f_{i'ij}\lambda_j\boldsymbol{\sigma}\cdot\int d\Omega_r Y^*_{lm'}(\hat{r})\mathbf{L}Y_{lm}(\hat{r})|B\rangle^{sf} \qquad (2.125) \end{aligned}$$

We put the spin indices in and call the last part of Eq. (2.125) $\mathcal{A}$:

$$\begin{aligned} \mathcal{A} &= {}^{sf}\langle B'(\mu')|f_{i'ij}\lambda_j\boldsymbol{\sigma}|B(\mu)\rangle^{sf}\int d\Omega_r Y^*_{lm'}\mathbf{L}Y_{lm} \\ &= \sum_q (-1)^q \int d\Omega_r Y^*_{lm'} L_q Y_{lm}\, {}^{sf}\langle B'(\mu')|f_{i'ij}\lambda_j\sigma_{-q}|B(\mu)\rangle^{sf} \qquad (2.126) \end{aligned}$$

where σ_{-q} is defined in Eq. (2.91) and Eq. (2.92). The operator L_q is defined as

$$L_{\pm 1} = \mp\frac{1}{\sqrt{2}}(L_x \pm L_y) \qquad (2.127)$$
$$L_0 = L_z \qquad (2.128)$$

By using the Wigner-Eckart theorem and pages of manipulations of the Clebsch-Gordan coefficients, $3j$ symbols and $6j$ symbols, we bring $\mathcal{A}$ into the form

$$\begin{aligned} \mathcal{A} &= {}^{f}\langle B'||f_{i'ij}\lambda_j\boldsymbol{\sigma}||B\rangle^{f}\sum_J (-1)^{\frac{1}{2}+J+l}\sqrt{l(l+1)(2l+1)}\begin{Bmatrix} \frac{1}{2} & \frac{1}{2} & 1 \\ l & l & J \end{Bmatrix} \\ &\times\langle\tfrac{1}{2}\mu; lm|\tfrac{1}{2}l; Jm'+\mu'\rangle\langle\tfrac{1}{2}\mu'; lm'|\tfrac{1}{2}l; Jm'+\mu'\rangle \qquad (2.129) \end{aligned}$$

	$\lambda^{s,I}_{\beta\alpha}$					
	$I=0$			$I=1$		
	$\bar{K}N$	$\pi\Sigma$	$\pi\Lambda$	$\bar{K}N$	$\pi\Sigma$	$\pi\Lambda$
$\bar{K}N$	$-\frac{3}{2}$	$\frac{1}{2\sqrt{6}}$	0	$\frac{1}{6}$	$\frac{1}{6}$	$\frac{\sqrt{6}}{4}$
$\pi\Sigma$	$\frac{1}{2\sqrt{6}}$	$-\frac{4}{3}$	0	$\frac{1}{6}$	$-\frac{2}{3}$	$-\frac{2}{\sqrt{6}}$
$\pi\Lambda$	0	0	0	$\frac{\sqrt{6}}{4}$	$-\frac{2}{\sqrt{6}}$	0

Table 4. The coupling constants $\lambda^{s,I}_{\beta\alpha}$ for different incoming and outgoing channels α and β.

In (2.129) ${}^f\langle B'||f_{i'i}f_{j'j}\lambda_j\sigma||B\rangle^f$ is obtained by applying the Wigner-Eckart theorem in the spin space:

$$ {}^{sf}\langle B'(\mu')|f_{i'i}f_{j'j}\lambda_j\sigma_{-q}|B\mu\rangle^{sf} = (-1)^{\frac{1}{2}-\mu'}\begin{pmatrix} \frac{1}{2} & 1 & \frac{1}{2} \\ -\mu' & -q & \mu \end{pmatrix} {}^f\langle B'||f_{i'i}f_{j'j}\lambda_j\sigma||B\rangle^f \tag{2.130} $$

The object with the big parentheses is the $3j$ symbol. Detailed calculations with SU(6) quark spin-flavor wave function reveals the relation

$$ \begin{aligned} &{}^{sf}\langle B'||f_{i'i}f_{j'j}\lambda_j\sigma||B\rangle^{sf} \\ &= \sum_I \lambda^{s,I}_{\beta\alpha}\langle I_B i_B; I_M i_M|I_B I_M; I0\rangle\langle I_{B'} i_{B'}; I_{M'} i_{M'}|I_{B'} I_{M'}; I0\rangle \end{aligned} \tag{2.131} $$

The values for the coupling constants $\lambda^{s,I}_{\beta\alpha}$ are calculated by the Mathematica package and double checked by careful hand calculations. The are listed in Table 4.

By substituting all these relations back into $v^{cs}_{\beta\alpha}(\mathbf{k}'\mu', \mathbf{k}\mu)$, we obtain

$$
\begin{aligned}
& v^{cs}_{\beta\alpha}(\mathbf{k}'\mu', \mathbf{k}\mu) \\
&= \frac{1}{2f^2}\frac{1}{2\pi^2\sqrt{2\omega_k 2\omega_{k'}}} \\
&\quad \times \sum_I \lambda^{s,I}_{\beta\alpha} \langle I_B i_B; I_M i_M | I_B I_M; I0\rangle \langle I_{B'} i_{B'}; I_{M'} i_{M'} | I_{B'} I_{M'}; I0\rangle \\
&\quad \times \sum_{JM} \sum_{lmm'} \langle \tfrac{1}{2}\mu; lm | \tfrac{1}{2} l; JM\rangle \langle \tfrac{1}{2}\mu'; lm' | \tfrac{1}{2} l; JM\rangle Y^*_{lm}(\hat{k}) Y_{lm'}(\hat{k}') \\
&\quad \times (-2)\sqrt{6l(l+1)(2l+1)}(-1)^{J+l+\frac{1}{2}} \left\{ \begin{array}{ccc} \frac{1}{2} & \frac{1}{2} & 1 \\ l & l & J \end{array} \right\} \\
&\quad \times \int_0^R dr\, r^2 \left[2N_s^2 \frac{1}{r} j_0(\omega_s r) j_1(\omega_s r) \right] j_l(kr) j_l(k'r) \qquad (2.132)
\end{aligned}
$$

The equations (2.121) and (2.132) have the same form as the equations (2.8) and (2.9) in Ref. [36], but as shown in the Table 2 and the Table 4, the coupling constants (or the spin-flavor matrix elements) are now different[58]. They have to be recalculated, in this case, by the Mathematica package.

Chapter 3

Explicit Equations

3.1 The Coupled $\bar{K}N$ System

The antikaon-nucleon interaction at low energy is not a simple one. Even at zero kinetic energy ($\bar{K}N$ threshold = 1432 MeV), K^-p couples to the open- or nearly open- strangeness -1 channels:

$$K^-p \rightarrow \begin{cases} K^-p & \\ \bar{K}^0n & -5 \text{ MeV} \\ \pi^+\Sigma^- & +95 \text{ MeV} \\ \pi^0\Sigma^0 & +104 \text{ MeV} \\ \pi^-\Sigma^+ & +103 \text{ MeV} \\ \pi^0\Lambda & +181 \text{ MeV} \end{cases} \tag{3.1}$$

There are also numbers of resonances in this energy range which makes things more complicated. These includes $\Lambda^*(1405)$, $\Sigma^{*0}(1385)$, and $\Lambda^*(1520)$. In the rest of this chapter, we will apply the Cloudy Bag Model to this complicated system and solve the resulting equations numerically.

We assume isospin symmetry and thus use the 2 isospin channels $\pi\Sigma(I = 0)$ and $\pi\Sigma(I = 1)$ instead of 3 charge channels $\pi^{\pm}\Sigma^{\mp}$ and $\pi^0\Sigma^0$. As long as there is no isospin breaking, we can express the 3 charge channels in terms of isospin channels. The $\pi\Sigma(I = 2)$ channel is not included since it does not couple to the $\bar{K}N$ system. The relation between charge channels and isospin channels are

$$|K^-p\rangle = \frac{1}{\sqrt{2}}|0,0\rangle + \frac{1}{\sqrt{2}}|1,0\rangle) \tag{3.2}$$

$$|\bar{K}^0n\rangle = -\frac{1}{\sqrt{2}}|0,0\rangle + \frac{1}{\sqrt{2}}|1,0\rangle) \tag{3.3}$$

$$|\pi^+\Sigma^-\rangle = \frac{1}{\sqrt{6}}|2,0\rangle' - \frac{1}{\sqrt{2}}|1,0\rangle' + \frac{1}{\sqrt{3}}|0,0\rangle' \tag{3.4}$$

$$|\pi^0\Sigma^0\rangle = \frac{\sqrt{2}}{\sqrt{3}}|2,0\rangle' - \frac{1}{\sqrt{3}}|0,0\rangle' \tag{3.5}$$

$$|\pi^-\Sigma^+\rangle = \frac{1}{\sqrt{6}}|2,0\rangle' + \frac{1}{\sqrt{2}}|1,0\rangle' + \frac{1}{\sqrt{3}}|0,0\rangle' \tag{3.6}$$

$$|\pi^0\Lambda\rangle = |1,0\rangle'' \tag{3.7}$$

When do use charge channel, we include the mass difference between K^-p and $\bar{K}^0n$. So in this thesis, when we need to consider the mass difference of K^-p and $\bar{K}^0n$, we use explicit charge channel for them, otherwise we use isospin channel for them. We call the former "charge basis" and the later "isospin basis" even though the $\pi\Sigma$ channels are always in isospin basis throughout this thesis.

We list the channel assignment in Table 5.

α	1	2	3	4	5
Charge Basis	K^-p	$\bar{K}^0n$	$\Sigma\pi$ $(I=0)$	$\Sigma\pi$ $(I=1)$	$\Lambda\pi^0$
Isospin Basis	$\bar{K}N(I=0)$	$\bar{K}N(I=1)$	$\Sigma\pi$ $(I=0)$	$\Sigma\pi$ $(I=1)$	$\Lambda\pi^0$

Table 5. Channel assignment with "charge basis" and "isospin basis".

3.2 The CBM Interaction for the $\bar{K}N$ System

In Chapter 2 we studied the basic interaction vertices of the to $\bar{K}N$ interaction in the CBM. The potential between incoming channel α and outgoing channel β can be written as a sum of 5 terms

$$\begin{aligned} v_{\beta\alpha}(\mathbf{k}'\mu',\mathbf{k}\mu) &= v^{(a)}_{\beta\alpha}(\mathbf{k}'\mu',\mathbf{k}\mu)+v^{(b)}_{\beta\alpha}(\mathbf{k}'\mu',\mathbf{k}\mu)+v^{(c)}_{\beta\alpha}(\mathbf{k}'\mu',\mathbf{k}\mu) \\ &\quad +v^{(d)}_{\beta\alpha}(\mathbf{k}'\mu',\mathbf{k}\mu)+v^{(e)}_{\beta\alpha}(\mathbf{k}'\mu',\mathbf{k}\mu) \end{aligned} \tag{3.8}$$

Where $\mathbf{k}$ is momentum and μ is spin. The Feynman diagram representation of these potentials are shown as Fig. 4.

The potential $v^{(a)}$ is composed of two H_s vertices with a $\Lambda^*_{1/2}$ as an intermediate state:

$$v^{(a)}_{\beta\alpha}(\mathbf{k}'\mu',\mathbf{k}\mu)=\langle\beta|H_s|\Lambda^*_{1/2}\rangle\frac{1}{E-M^*_s}\langle\Lambda^*_{1/2}|H_s|\alpha\rangle \tag{3.9}$$

where the form factor $u_{\Lambda^*_{1/2}\alpha}$ is defined in Eq. (2.77). After we substitute the expression of the $BM\Lambda^*_{1/2}$ vertex, Eq. (2.76), we find the potential to be

$$\begin{aligned} v^{(a)}_{\beta\alpha}(\mathbf{k}'\mu',\mathbf{k}\mu) &= \frac{\delta_{\mu\mu'}}{4f^2}\frac{\lambda^\Lambda_\beta\lambda^\Lambda_\alpha}{E-M^*_s}\langle I_{B'}i_{B'};I_{M'}i_{M'}|I_{B'}I_{M'};00\rangle \\ &\quad\times\langle I_Bi_B;I_Mi_M|I_BI_M;00\rangle\frac{u_{\Lambda^*_{1/2}\beta}(k)u_{\Lambda^*_{1/2}\alpha}(k)}{\sqrt{(2\pi)^32\omega_{k'}}\sqrt{(2\pi)^32\omega_k}} \end{aligned} \tag{3.10}$$

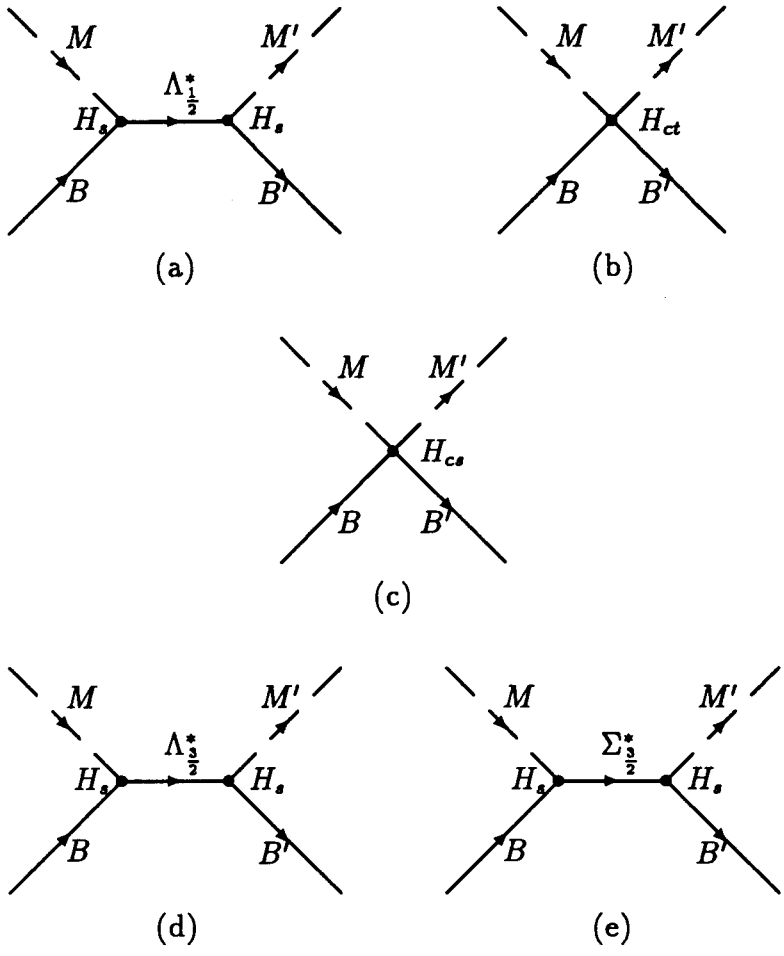

Figure 4. The full Feynman diàgrams of 5 CBM potentials for the S-, P-, and D-wave $\bar{K}N$ system interactions.

The partial wave expansion of this potential is

$$
\begin{aligned}
v^{(a),lJ}_{\beta\alpha}(k',k) &= \sum_{m+\mu=M}\sum_{m'+\mu'=M}\int d\Omega_k d\Omega_{k'}\,\frac{\pi}{2}Y^*_{lm'}(\hat{k}')Y_{lm}(\hat{k})v^{(a)}_{\beta\alpha}(\mathbf{k}'\mu',\mathbf{k}\mu) \\
&\quad\times\langle lm';\tfrac{1}{2}\mu'|l\tfrac{1}{2};JM\rangle\langle lm;\tfrac{1}{2}\mu|l\tfrac{1}{2};JM\rangle \\
&= \delta_{l0}\delta_{J\frac{1}{2}}\frac{1}{2f^2}\frac{u_{\Lambda^*_{1/2}\beta}(k')u_{\Lambda^*_{1/2}\alpha}(k)}{4\pi\sqrt{2\omega_{k'}2\omega_k}}\frac{1}{E-M^*_s}\frac{\lambda^{\Lambda}_{\beta}\lambda^{\Lambda}_{\alpha}}{2} \\
&\quad\times\langle I_{B'}i_{B'};I_{M'}i_{M'}|I_{B'}I_{M'};00\rangle\langle I_Bi_B;I_Mi_M|I_BI_M;00\rangle \quad (3.11)
\end{aligned}
$$

The Kronecker symbol in Eq. (3.11) shows this diagram contributes to S-wave interaction only, while the Clebsch-Gordan coefficients shows it is an isospin-0 interaction.

The potential $v^{(b)}$ in (3.8) consists of the time derivative part of H_c. It can be written as

$$
\begin{aligned}
&v^{(b)}_{\beta\alpha}(\mathbf{k}'\mu',\mathbf{k}\mu) \\
&= \langle\beta\mu'|H_{ct}|\alpha\mu\rangle \\
&= \frac{\delta_{\mu'\mu}(\omega_k+\omega_{k'})}{2\pi^2\sqrt{2\omega_k 2\omega_{k'}}}\sum_I\frac{\lambda^{t,I}_{\beta\alpha}}{2f^2}\langle I_Bi_B;I_Mi_M|I_BI_M;Ii\rangle\langle I_{B'}i_{B'};I_{M'}i_{M'}|I_{B'}I_{M'};Ii\rangle \\
&\quad\times\sum_{lm}Y^*_{lm}(\hat{k})Y_{lm}(\hat{k}')N_s^2\int_0^R dr\,r^2[j_0^2(\omega_s r)+j_1^2(\omega_s r)]j_l(kr)j_l(k'r) \quad (3.12)
\end{aligned}
$$

The partial wave expansion of potential $v^{(b)}$ is

$$
\begin{aligned}
v^{(b),lJ}_{\beta\alpha}(k',k) &= \sum_{m+\mu=M}\sum_{m'+\mu'=M}\int d\Omega_k d\Omega_{k'}\,\frac{\pi}{2}Y^*_{lm'}(\hat{k}')Y_{lm}(\hat{k})v^{(b)}_{\beta\alpha}(\mathbf{k}'\mu',\mathbf{k}\mu) \\
&\quad\times\langle lm';\tfrac{1}{2}\mu'|l\tfrac{1}{2};JM\rangle\langle lm;\tfrac{1}{2}\mu|l\tfrac{1}{2};JM\rangle \quad (3.13)
\end{aligned}
$$

The integration in (3.13) is quite straight forward. Using the orthogonality relationship of Y_{lm} and Y^*_{lm}, we obtain:

$$
v^{(b),lJ}_{\beta\alpha}(k',k) = \frac{(\omega_k+\omega'_k)}{4\pi\sqrt{2\omega_{k'}2\omega_k}}N_s^2\int_0^R dr\,r^2[j_0^2(\omega_s r)+j_1^2(\omega_s r)]j_l(kr)j_l(k'r)
$$

$$\times \sum_I \langle I_{B'} i_{B'}; I_{M'} i_{M'} | I_{B'} I_{M'}; Ii \rangle \frac{\lambda^{t,I}_{\beta\alpha}}{2f^2} \langle I_B i_B; I_M i_M | I_B I_M; Ii \rangle \tag{3.14}$$

The potential $v^{(c)}$ is the spatial derivative part of H_c. It is

$$\begin{aligned}
& v^{(c)}_{\beta\alpha}(\mathbf{k}'\mu', \mathbf{k}\mu) \\
&= \langle \beta\mu' | H_{cs} | \alpha\mu \rangle \\
&= \frac{1}{2\pi^2\sqrt{2\omega_k 2\omega_{k'}}} \sum_I \langle I_{B'} i_{B'}; I_{M'} i_{M'} | I_{B'} I_{M'}; Ii \rangle \frac{\lambda^{cs,I}_{\beta\alpha}}{2f^2} \langle I_B i_B; I_M i_M | I_B I_M; Ii \rangle \\
&\quad \times \sum_{JM} \sum_{lmm'} \langle \tfrac{1}{2}\mu; lm | \tfrac{1}{2} l; JM \rangle \langle \tfrac{1}{2}\mu'; lm' | \tfrac{1}{2} l; JM \rangle Y^*_{lm}(\hat{k}) Y_{lm'}(\hat{k}') \\
&\quad \times (-2)\sqrt{6l(l+1)(2l+1)}\,(-1)^{J+l+\frac{1}{2}} \begin{Bmatrix} \frac{1}{2} & \frac{1}{2} & 1 \\ l & l & J \end{Bmatrix} \\
&\quad \times \int_0^R dr\, r^2 \left[2N_s^2 \frac{1}{r} j_0(\omega_s r) j_1(\omega_s r) \right] j_l(kr) j_l(k'r)
\end{aligned} \tag{3.15}$$

Unlike the previous potentials $v^{(a)}$ and $v^{(b)}$, the partial wave expansion of $v^{(c)}$ is complicated. By definition,

$$\begin{aligned}
v^{(c),lJ}_{\beta\alpha}(k', k) &= \sum_{m+\mu=M} \sum_{m'+\mu'=M} \int d\Omega_k d\Omega_{k'} \frac{\pi}{2} Y^*_{lm'}(\hat{k}') Y_{lm}(\hat{k}) v^{(c)}_{\beta\alpha}(\mathbf{k}'\mu', \mathbf{k}\mu) \\
&\quad \times \langle lm'; \tfrac{1}{2}\mu' | l\tfrac{1}{2}; JM \rangle \langle lm; \tfrac{1}{2}\mu | l\tfrac{1}{2}; JM \rangle
\end{aligned} \tag{3.16}$$

Using the orthogonal relations of the spherical harmonics and the properties of the Clebsch-Gordan coefficients, after some lengthy manipulations, we obtain

$$v^{(c),lJ}_{\beta\alpha}(k', k) = \frac{-2}{4\pi\sqrt{2\omega_{k'} 2\omega_k}} \sqrt{6l(l+1)(2l+1)}\,(-1)^{J+l+\frac{1}{2}} \begin{Bmatrix} \frac{1}{2} & \frac{1}{2} & 1 \\ l & l & J \end{Bmatrix}$$

l	0	1	2
$J = \lvert l - \frac{1}{2} \rvert$	0	4	6
$J = \lvert l + \frac{1}{2} \rvert$	0	-2	-4

Table 6. The values of quantity A^{lJ} for $l \leq 2$.

$$\times \sum_I \langle I_{B'} i_{B'}; I_{M'} i_{M'} | I_{B'} I_{M'}; Ii \rangle \frac{\lambda^{s,I}_{\beta\alpha}}{2f^2} \langle I_B i_B; I_M i_M | I_B I_M; Ii \rangle$$
$$\times \int_0^R dr\, r^2 \left[2N_s^2 \frac{1}{r} j_0(\omega_s r) j_1(\omega_s r) \right] j_l(kr) j_l(k'r) \tag{3.17}$$

We define A^{lJ} as

$$A^{lJ} = (-2)\sqrt{6l(l+1)(2l+1)}\,(-1)^{J+l+\frac{1}{2}} \begin{Bmatrix} \frac{1}{2} & \frac{1}{2} & 1 \\ l & l & J \end{Bmatrix} \tag{3.18}$$

The values of A^{lJ} for $l \leq 2$ are tabulated in Table 6 and they are summarized as

$$A^{lJ} = \begin{cases} 2(l+1) & J = l - \frac{1}{2} \\ -2l & J = l + \frac{1}{2} \end{cases} \tag{3.19}$$

The final form of partial wave expansion of $v^{(c)}$

$$v^{(c),lJ}_{\beta\alpha}(k', k)$$
$$= \frac{2A^J_l}{4\pi\sqrt{2\omega_{k'} 2\omega_k}} \int_0^R dr\, r^2 \left[2N_s^2 \frac{1}{r} j_0(\omega_s r) j_1(\omega_s r) \right] j_l(kr) j_l(k'r)$$
$$\times \sum_I \langle I_{B'} i_{B'}; I_{M'} i_{M'} | I_{B'} I_{M'}; Ii \rangle \frac{\lambda^{s,I}_{\beta\alpha}}{2f^2} \langle I_B i_B; I_M i_M | I_B I_M; Ii \rangle \tag{3.20}$$

The potential $v^{(d)}$ corresponds to the incoming baryon absorbing a meson, becoming a virtual $\Lambda^*_{3/2}$ and then the $\Lambda^*_{3/2}$ emitting a meson, and becoming

the outgoing baryon. The potential $v^{(d)}$ has the form

$$\begin{aligned} & v^{(d)}_{\beta\alpha}(\mathbf{k}'\mu', \mathbf{k}\mu) \\ &= \sum_{\nu} \langle \beta(\mu') | H_s | \Lambda^*_{3/2}(\nu) \rangle \frac{1}{E - M^*_d} \langle \Lambda^*_{3/2}(\nu) | H_s | \alpha(\mu) \rangle \\ &= \frac{1}{2\pi^2} \langle I_{B'} i_{B'}; I_{M'} i_{M'} | I_{B'} I_{M'}; 00 \rangle \frac{\lambda^{\Lambda}_{\beta} \lambda_{\alpha} \Lambda}{(2f)^2} \langle I_B i_B; I_M i_M | I_B I_M; 00 \rangle \\ &\quad \times \frac{u^{(2)}_{\Lambda^*_{3/2}\beta}(k') u^{(2)}_{\Lambda^*_{3/2}\alpha}(k)}{\sqrt{2\omega_{k'} 2\omega_k}} \frac{1}{E - M^*_d} \sum_{\nu} Y^*_{2(\nu-\mu)}(\hat{k}) Y_{2(\nu-\mu')}(\hat{k}') \\ &\quad \times \langle \tfrac{1}{2}\mu; 2\nu - mu | \tfrac{1}{2} 2; \tfrac{3}{2}\nu \rangle \langle \tfrac{1}{2}\mu'; 2\nu - mu' | \tfrac{1}{2} 2; \tfrac{3}{2}\nu \rangle \end{aligned} \tag{3.21}$$

We define the partial wave expansion of $v^{(d)}$ as

$$\begin{aligned} v^{(d),lJ}_{\beta\alpha}(k', k) &= \sum_{m+\mu=M} \sum_{m'+\mu'=M} \int d\Omega_k d\Omega_{k'} \frac{\pi}{2} Y^*_{lm'}(\hat{k}') Y_{lm}(\hat{k}) v^{(d)}_{\beta\alpha}(\mathbf{k}'\mu', \mathbf{k}\mu) \\ &\quad \times \langle lm'; \tfrac{1}{2}\mu' | l\tfrac{1}{2}; JM \rangle \langle lm; \tfrac{1}{2}\mu | l\tfrac{1}{2}; JM \rangle \end{aligned} \tag{3.22}$$

The final form of $v^{(d)}$, reached after a few pages of integration and Clebsch-Gordan coefficient re-coupling, is:

$$\begin{aligned} & v^{(d),lJ}_{\beta\alpha}(k', k) \\ &= \delta_{l2} \delta_{J\frac{3}{2}} \frac{u^{(2)}_{\Lambda^*_{3/2}\beta}(k') u^{(2)}_{\Lambda^*_{3/2}\alpha}(k)}{4\pi \sqrt{2\omega_{k'} 2\omega_k}} \frac{1}{E - M^*_d} \frac{\lambda^{\Lambda}_{\beta} \lambda^{\Lambda}_{\alpha}}{4f^2} \\ &\quad \times \langle I_{B'} i_{B'}; I_{M'} i_{M'} | I_{B'} I_{M'}; 00 \rangle \langle I_B i_B; I_M i_M | I_B I_M; 00 \rangle \end{aligned} \tag{3.23}$$

The potential $v^{(e)}$ is similar to $v^{(d)}$ except now the virtual particle is a $\Sigma^*_{3/2}$ instead of a $\Lambda^*_{3/2}$, and for $v^{(e)}$ the potential is in P-wave instead of D-wave for $v^{(d)}$:

$$v^{(e)}_{\beta\alpha}(\mathbf{k}'\mu', \mathbf{k}\mu) = \sum_{\nu} \langle \beta(\mu') | H_s | \Sigma^*_{3/2}(\nu) \rangle \frac{1}{E - M^*_p} \langle \Sigma^*_{3/2}(\nu) | H_s | \alpha(\mu) \rangle \tag{3.24}$$

Recall the Eq. (2.96), we obtain

$$
\begin{aligned}
& v^{(e)}_{\beta\alpha}(\mathbf{k}'\mu', \mathbf{k}\mu) \\
&= \frac{(2N_s^2R^2)^2}{6\pi^2}\frac{(j_0(\omega_s R)j_1(\omega_s R))^2}{E-M_p^*}\frac{j_1(k'R)j_1(kR)}{\sqrt{2\omega_{k'}2\omega_k}} \\
&\quad \times \sum_{\nu} Y^*_{1(\nu-\mu)}(\hat{k})Y_{1(\nu-\mu')}(\hat{k}')\langle \tfrac{1}{2}\mu; 1\nu-mu|\tfrac{1}{2}1; \tfrac{3}{2}\nu\rangle\langle \tfrac{1}{2}\mu'; 1\nu-mu'|\tfrac{1}{2}1; \tfrac{3}{2}\nu\rangle \\
&\quad \times \langle I_{B'}i_{B'}; I_{M'}i_{M'}|I_{B'}I_{M'}; 10\rangle \frac{\lambda^{\Sigma}_{\beta}\lambda^{\Sigma}_{\alpha}}{4f^2}\langle I_B i_B; I_M i_M|I_B I_M; 10\rangle \qquad (3.25)
\end{aligned}
$$

In a similar manner, we carry out the partial wave expansion for $v^{(e)}$:

$$
\begin{aligned}
v^{(e),lJ}_{\beta\alpha}(k',k) &= \delta_{l1}\delta_{J\frac{3}{2}}\frac{(N_s R j_0(\omega_s R))^4}{3\pi}\frac{1}{E-M_p^*}\frac{j_1(k'R)j_1(kR)}{\sqrt{2\omega_{k'}2\omega_k}} \\
&\quad \times \langle I_{B'}i_{B'}; I_{M'}i_{M'}|I_{B'}I_{M'}; 10\rangle \frac{\lambda^{\Sigma}_{\beta}\lambda^{\Sigma}_{\alpha}}{4f^2}\langle I_B i_B; I_M i_M|I_B I_M; 10\rangle \qquad (3.26)
\end{aligned}
$$

where the relation $j_1(\omega_s R) = j_0(\omega_s R)$ has been used in the derivation.

3.3 The Coupled-Channel Lippman-Schwinger Equation

In the previous section we discussed the potential describing $\bar{K}N$ system in the CBM. In this section, we show how to solve for $\bar{K}N$ scattering using the Lippman-Schwinger equation.

The operator form of the Lippman-Schwinger equation is

$$T = V + VGT \qquad (3.27)$$

where V is the potential operator, T is the T-matrix operator and G is the Green's function operator defined as

$$G = \frac{1}{E^{(+)} - H_0} \qquad (3.28)$$

The superscript $(+)$ means that the energy E approaches the real axis from above the above of the cut on the first E sheet.

Taking the matrix element between states $|\beta, \mathbf{k}'\mu'\rangle$ and $|\alpha, \mathbf{k}'\mu\rangle$, and using the completeness relations of the quantum states $|\gamma, \mathbf{p}\nu\rangle$, we obtain

$$T_{\beta\alpha}(\mathbf{k}'\mu', \mathbf{k}\mu) = V_{\beta\alpha}(\mathbf{k}'\mu', \mathbf{k}\mu) + \sum_{\gamma,\nu} \int d^3p \, \frac{V_{\beta\gamma}(\mathbf{k}'\mu', \mathbf{p}\nu) T_{\gamma\alpha}(\mathbf{p}\nu, \mathbf{k}\mu)}{E^{(+)} - E_\gamma(p)} \quad (3.29)$$

Here α and β are the indices for incoming and outgoing channels, $\mathbf{k}$ and $\mathbf{k}'$ are the COM momenta, and μ and μ' are the spin quantum numbers for the incoming and outgoing channels. The energy of intermediate channel γ at COM momentum p is $E_\gamma(k)$. The matrix elements are defined as

$$T_{\beta\alpha}(\mathbf{k}'\mu', \mathbf{k}\mu) = \langle \beta, \mathbf{k}'\mu' | T | \alpha, \mathbf{k}\mu \rangle \quad (3.30)$$

and

$$V_{\beta\alpha}(\mathbf{k}'\mu', \mathbf{k}\mu) = \langle \beta, \mathbf{k}'\mu' | V | \alpha, \mathbf{k}\mu \rangle \quad (3.31)$$

Substituting the partial wave expansions of T and V into (3.29) enables us to reduce the Lippman-Schwinger equation to a one dimensional form instead of the original 3 dimensional form. We define the partial wave expansion form of the T and V as

$$\begin{aligned} T^{lJ}_{\beta\alpha}(k', k) &= \sum_{m+\mu=M} \sum_{m'+\mu'=M} \langle lm'; \tfrac{1}{2}\mu' | l\tfrac{1}{2}; JM \rangle \langle lm; \tfrac{1}{2}\mu | l\tfrac{1}{2}; JM \rangle \\ &\quad \times \left(\frac{\pi}{2}\right) \int d\Omega_{k'} d\Omega_k Y^*_{lm'}(\hat{k}') Y_{lm}(\hat{k}) T_{\beta\alpha}(\mathbf{k}'\mu', \mathbf{k}\mu) \quad (3.32) \\ V^{lJ}_{\beta\alpha}(k', k) &= \sum_{m+\mu=M} \sum_{m'+\mu'=M} \langle lm'; \tfrac{1}{2}\mu' | l\tfrac{1}{2}; JM \rangle \langle lm; \tfrac{1}{2}\mu | l\tfrac{1}{2}; JM \rangle \\ &\quad \times \left(\frac{\pi}{2}\right) \int d\Omega_{k'} d\Omega_k Y^*_{lm'}(\hat{k}') Y_{lm}(\hat{k}) V_{\beta\alpha}(\mathbf{k}'\mu', \mathbf{k}\mu) \quad (3.33) \end{aligned}$$

where $T^{l\pm}$ ($V^{l\pm}$) is sometimes used as a shorthand for $J = l \pm \frac{1}{2}$.

Notice that we have carried out the partial wave expansion for all the potential terms in Section 3.2. Substituting Eq. (3.32) and Eq. (3.33) into the full space Lippman-Schwinger equation (3.29), we obtain the one-dimensional, coupled-channel integral equations:

$$T^{lJ}_{\beta\alpha}(k',k) = V^{lJ}_{\beta\alpha}(k',k) + \frac{2}{\pi}\sum_{\gamma}\int_0^\infty dp\, \frac{p^2 V^{lJ}_{\beta\gamma}(k',p)T^{lJ}_{\gamma\alpha}(p,k)}{E^{(+)} - E_\gamma(k)} \tag{3.34}$$

All of our scattering calculations are based on Eq. (3.34).

3.3.1 Scattering Equations

The one-dimensional Lippman-Schwinger Equation (3.34) can be solved analytically only for very limited cases—such as single-channel separable potential. We solve it numerically for the coupled-channel $\bar{K}N$ system in the CBM. The $i\epsilon$ prescription in (3.34) is handled with the Haftel-Tabakin method[59] extended to coupled-channel case. The Haftel-Tabakin method uses a principle value subtraction to remove the singularity of the (3.34) at $E = E_\gamma(p)$. We let $k_{0\gamma}$ be the "on-shell" momentum of channel γ, that is

$$E_\gamma(k_{0\gamma}) = E \tag{3.35}$$

we thus write

$$\begin{aligned}
&\frac{2}{\pi}\int_0^\infty dp\, \frac{p^2 V_{\beta\gamma}(k',p)T_{\gamma\alpha}(p,k)}{E^{(+)} - E_\gamma(p)} \\
&= \frac{2}{\pi}\int_0^\infty dp\, \left[\frac{p^2 V_{\beta\gamma}(k',p)T_{\gamma\alpha}(p,k)}{E^{(+)} - E_\gamma(p)} - \frac{2\rho_\gamma k^2_{0\gamma} V_{\beta\gamma}(k',k_{0\gamma})T_{\gamma\alpha}(k_{0\gamma},k)}{k^2_{0\gamma} - p^2 + i\epsilon}\right] \\
&\quad + \frac{2}{\pi} \times 2\rho_\gamma k^2_{0\gamma} V_{\beta\gamma}(k',k_{0\gamma})T_{\gamma\alpha}(k_{0\gamma},k)\int_0^\infty dp\, \frac{1}{k^2_{0\gamma} - p^2 + i\epsilon}
\end{aligned} \tag{3.36}$$

where ρ_γ is the "reduced mass" in a relativistic sense

$$2\rho_\gamma = \left.\frac{dp^2}{dE_\gamma}\right|_{E_\gamma=E} \tag{3.37}$$

The second integral in Eq. (3.36) can be carried analytically

$$\int_0^\infty dp \, \frac{1}{k_{0\gamma}^2 - p^2 + i\epsilon} = -\frac{i\pi}{2k_{0\gamma}} \tag{3.38}$$

Since the integrand in the first integral in Eq. (3.36) now vanishes at the on shell point, it is no longer singular and the $i\epsilon$ is not needed. We can now use the Gaussian quadrature method to approximate the integral by a summation over a set of grid points:

$$\int_0^\infty dp \Longrightarrow \sum_{i=1}^{N} \omega_i \tag{3.39}$$

Applying Gaussian method to the first part of Eq. (3.36), and with Eq. (3.34), we obtain

$$\begin{aligned}
&T_{\beta\alpha}(k',k) \\
&= V_{\beta\alpha}(k',k) \\
&\quad + \sum_\gamma \frac{2}{\pi} \int_0^\infty dp \left[\frac{p^2 V_{\beta\gamma}(k',p) T_{\gamma\alpha}(p,k)}{E - E_\gamma(p)} - \frac{2\rho_\gamma k_{0\gamma}^2 V_{\beta\gamma}(k',k_{0\gamma}) T_{\gamma\alpha}(k_{0\gamma},k)}{k_{0\gamma}^2 - p^2} \right] \\
&\quad + \sum_\gamma \frac{2}{\pi} \times 2\rho_\gamma k_{0\gamma}^2 V_{\beta\gamma}(k',k_{0\gamma}) T_{\gamma\alpha}(k_{0\gamma},k) \int_0^\infty dp \, \frac{1}{k_{0\gamma}^2 - p^2 + i\epsilon} \qquad (3.40) \\
&= V_{\beta\alpha}(k',k) \\
&\quad + \sum_\gamma \frac{2}{\pi} \sum_{i=1}^{N} w_i \left[\frac{p_i^2 V_{\beta\gamma}(k',p_i) T_{\gamma\alpha}(p_i,k)}{E - E_\gamma(p_i)} - \frac{2\rho_\gamma k_{0\gamma}^2 V_{\beta\gamma}(k',k_{0\gamma}) T_{\gamma\alpha}(k_{0\gamma},k)}{k_{0\gamma}^2 - p_i^2} \right] \\
&\quad - \sum_\gamma 2i\rho_\gamma k_{0\gamma} V_{\beta\gamma}(k',k_{0\gamma}) T_{\gamma\alpha}(k_{0\gamma},k) \qquad (3.41)
\end{aligned}$$

Here $\{p_i | i = 1, N\}$ are the Gaussian grid points and $\{w_i | i = 1, N\}$ are the corresponding weight factors.

We define

$$V_{n\beta,m\alpha} = \begin{cases} V_{\beta\alpha}(p_n, p_m) & \text{for } n = 1 \ldots N \quad and \quad m = 1 \ldots N \\ V_{\beta\alpha}(k_{0\beta}, p_m) & \text{for } n = N+1 \quad and \quad m = 1 \ldots N \\ V_{\beta\alpha}(p_n, k_{0\alpha}) & \text{for } n = 1 \ldots N \quad and \quad m = N+1 \\ V_{\beta\alpha}(k_{0\beta}, k_{0\alpha}) & \text{for } n = N+1 \quad and \quad m = N+1 \end{cases} \tag{3.42}$$

$$T_{n\beta,m\alpha} = \begin{cases} T_{\beta\alpha}(p_n, p_m) & \text{for } n = 1 \ldots N \quad and \quad m = 1 \ldots N \\ T_{\beta\alpha}(k_{0\beta}, p_m) & \text{for } n = N+1 \quad and \quad m = 1 \ldots N \\ T_{\beta\alpha}(p_n, k_{0\alpha}) & \text{for } n = 1 \ldots N \quad and \quad m = N+1 \\ T_{\beta\alpha}(k_{0\beta}, k_{0\alpha}) & \text{for } n = N+1 \quad and \quad m = N+1 \end{cases} \tag{3.43}$$

and

$$G_{n\gamma} = \begin{cases} \frac{2}{\pi} \frac{w_n p_n^2}{E - E_\gamma(p_n)} & \text{for } n = 1 \ldots N \\ -\sum_{i=1}^{N} \frac{2}{\pi} \frac{w_i k_{0\gamma}^2}{k_{0\gamma}^2 - p_i^2} \left.\frac{dp^2}{dE}\right|_{k_{0\gamma}} - ik_{0\gamma} \left.\frac{dp^2}{dE}\right|_{k_{0\gamma}} & \text{for } n = N+1 \end{cases} \tag{3.44}$$

Now using Eq. (3.41) produces the set of linear equations

$$T_{n\beta,m\alpha} = V_{n\beta,m\alpha} + \sum_{\gamma} \sum_{i=1}^{N+1} V_{n\beta,i\gamma} G_{i\gamma} T_{i\gamma,m\alpha} \tag{3.45}$$

where $T_{n\beta,m\alpha}$ are unknowns. We have now $n^2(N+1)^2$ unknowns and $n^2(N+1)^2$ equations (n is number of channels and N is the number of Gaussian grid points). We can therefore solve these equations for the T-matrix elements. We line up the elements of T, V, and G up an orderly fashion and obtain a matrix equation

$$(1 - VG)T = V \tag{3.46}$$

The set of linear equations (3.46) can be solved using Gaussian elimination method (the inverse of the matrix $(1 - VG)$ is not actually calculated). In

our case, the potential V is taken as the sum of 5 individual terms (shown in Fig. 4). We thus solve for $\bar{K}N$ scattering as a 5 channel problem with 24 or 32 Gaussian grid points used in each channel.

3.3.2 Bound State and Resonance

If a physical system has a bound state or pole at some energy, the T-matrix must have a pole at the energy (although not all poles of T will be bound state or resonances). From matrix version of Lippman-Schwinger Equation (3.46), we can see there are two occasions in which T-matrix can have poles. Either the potential matrix V has a pole, or the matrix $(1 - VG)$ is singular. The first type of pole is called a "fixed, or potential pole" ("fixed" since it is independent of potential strength). We are not interested in this type of pole because it depends on details of the model as opposed to the dynamic characteristic of the model. The second type of pole, the so-called "dynamic pole", occurs where $(1 - VG)$ is singular. It depends on the potential's strength and it what we are interested in. Mathematically, the equations for a dynamic pole, a singular $(1 - VG)$, is equivalent to equation

$$\det(1 - VG) = 0 \tag{3.47}$$

This type pole is called "moving pole" because its position varies with the strength of the coupling. The position of the pole on the complex energy plane directly reflects the character of the bound state or resonance of the system. We look for the position of the pole by searching for the solution of Eq. (3.47) on the complex energy plane[60, 61]. The search with the nuclear potential alone is quite straight forward. We will concentrate on the nuclear

plus Coulomb interaction. The nuclear case can be treated as a special case of that (with zero Coulomb potential).

3.3.3 Bound State With Coulomb Interaction

The bound state problem with the Coulomb interaction in addition to the hadronic interaction raises some special difficulty due to the singularity of the Coulomb potential at $\mathbf{q} = 0$ in the momentum space:

$$V^C(\mathbf{k}'\mu', \mathbf{k}\mu) = \frac{Z_1 Z_2 e^2}{2\pi^2} \frac{\delta_{\mu'\mu}}{|\mathbf{k}' - \mathbf{k}|^2} \tag{3.48}$$

The Kwon-Tabakin-Lande method[62] is used to remove this singularity, along with Landau's extension to the couple channel problems[60, 61].

Due to the limitation of this method in the open channel, which we will show later, we assume that there is *no Coulomb interaction in the open channels.* This does not propose too big of a problem in our case because the $\bar{K}^0 n$ has no Coulomb interaction at all and the $\Sigma\pi$ and $\Lambda\pi$ thresholds are far below the $K^- p$ threshold, the particles in these channels are quite energetic therefor not affected much by Coulomb forces. This will however limit the applicability of the calculation when applied to branching ratios.

We start from the partial wave decomposition of the Coulomb potential

$$\begin{aligned} V_C^{lJ}(k', k) &= \sum_{m+\mu=M} \sum_{m'+\mu'=M} \int d\Omega_k d\Omega_{k'} \frac{\pi}{2} Y^*_{lm'}(\hat{k}') Y_{lm}(\hat{k}) V_C(\mathbf{k}'\mu', \mathbf{k}\mu) \\ &\quad \times \langle lm'; \tfrac{1}{2}\mu' | l\tfrac{1}{2}; JM \rangle \langle lm; \tfrac{1}{2}\mu | l\tfrac{1}{2}; JM \rangle \qquad (3.49) \\ &= \frac{Z_1 Z_2 e^2}{2k'k} Q_l(z_{k'k}) \qquad (3.50) \end{aligned}$$

where $z_{k'k} = (k'^2 + k^2)/2k'k$ and $Q_l(z_{k'k})$ is the Legendre function of the

second kind

$$Q_l(z) = \frac{1}{2}\int_{-1}^{1} \frac{P_n(t)}{z-t} dt \tag{3.51}$$

As we see from the the first few l values,

$$Q_0(z) = \frac{1}{2}\log\left|\frac{z+1}{z-1}\right| \tag{3.52}$$

$$Q_1(z) = \frac{z}{2}\log\left|\frac{z+1}{z-1}\right| - 1 \tag{3.53}$$

$$Q_2(z) = \frac{1}{4}\left(3z^2-1\right)\log\left|\frac{z+1}{z-1}\right| - \frac{3z}{2} \tag{3.54}$$

all of them have singularities at $z = 1$.

We look back at the integral term in Eq. (3.34), and notice that the potential V is the sum of the nuclear potential V^N and the Coulomb potential V^C (we omit the indices lJ with the understanding that all the computation is done in the partial-wave basis). The explicit form of the integral term is

$$\int_0^\infty dp \left\{ \frac{p^2 V^N_{\beta\gamma}(k',p) T_{\gamma\alpha}(p,k)}{E^{(+)} - E_\gamma(p)} + \frac{p^2 V^C_{\beta\gamma}(k',p) T_{\gamma\alpha}(p,k)}{E^{(+)} - E_\gamma(p)} \right\} = I^N + I^C \tag{3.55}$$

The nuclear part I^N can be easily approximated by Gaussian quadrature method as we did in solving the T matrix case. The Coulomb part, however, has two possible singularities. One of the possibility is $E_\gamma(p) = E$ and the other is $p = k'$. The Kwon-Tabakin-Lande method[62] can only remove the second singularity. One way to avoid the first singularity is to deal with closed channel. That way, the energy E is below the threshold and the $E_\gamma(p)$ is always above threshold therefore there is no singularity. That is why we assumed from very beginning that there is *no Coulomb interaction in the open channels.*

The Kwon-Tabakin-Lande method[62] removes the $p = k'$ singularity by subtracting the singular part out of the original integral

$$\begin{aligned} I^C &= \int_0^\infty dp \frac{p^2 V^C_{\beta\gamma}(k',p) T_{\gamma\alpha}(p,k)}{E - E_\gamma(p)} \\ &= \int_0^\infty dp\, V^C_{\beta\gamma}(k',p) \left[\frac{p^2 T_{\gamma\alpha}(p,k)}{E - E_\gamma(p)} - \frac{k'^2 T_{\gamma\alpha}(k',k)}{(E - E_\gamma(k')) P_l(z_{k'p})} \right] \\ &\quad + \frac{k'^2 S^l_{\beta\gamma}(k') T_{\gamma\alpha}(k',k)}{E - E_\gamma(k')} \end{aligned} \tag{3.56}$$

We understand that $V^C_{\beta\gamma}$ and $S^l_{\beta\gamma}$ vanish except when the channel β is the same as γ and there is a Coulomb interaction in that channel. The function $S^l_{\beta\gamma}(k')$ is defined as[2]

$$S^l_{\beta\gamma}(k') = \int_0^\infty dp \frac{V^C_{\beta\gamma}(k',p)}{P_l(z_{k'p})} \tag{3.57}$$

and for a closed channel

$$\begin{aligned} S^l_{\gamma\gamma}(k') &= \frac{\pi Z_1 Z_2 e^2}{2k'} \left[\frac{\pi}{2} - \int_0^\infty \frac{dp}{p} \frac{W_{l-1}(z_{k'p})}{P_l(z_{k'p})} \right] \\ &= \frac{\pi Z_1 Z_2 e^2}{2k'} \left[\frac{\pi}{2} - I_l \right] \end{aligned} \tag{3.58}$$

where

$$W_l(z) = \sum_{l'=1} \frac{1}{l'} P_{l'-1}(z) P_{l-l'}(z) \tag{3.59}$$

We take $W_{-1} = 0$ and the Lande's subtraction integral I_l as

$$I_l = \frac{1}{\pi} \int_0^\infty \frac{dp}{p} \frac{W_{l-1}(z_{k'p})}{P_l(z_{k'p})} \tag{3.60}$$

The values of I_l for the first few l has been calculated and tabulated in Ref. [62]. We list their results in Table 7.

[2]The definition of a non-vanishing $S^l_{\gamma\gamma}$ here is different from the S_l in Ref. [62] by a constant factor.

l	0	1	2
I_l	0	1	$\sqrt{\frac{3}{2}}$

Table 7. The values of Lande's subtraction integral I_l.

Notice that the integrand in the first term on the r.h.s of Eq. (3.56) has no singularity any more. We now can apply the Gaussian quadrature method to it along with the nuclear part I_N:

$$\begin{aligned} I^C + I^N &= \sum_{i=1}^{N} w_i V^C_{\beta\gamma}(k', p_i) \left[\frac{p_i^2 T_{\gamma\alpha}(p_i, k)}{E - E_\gamma(p_i)} - \frac{k'^2 T_{\gamma\alpha}(k', k)}{(E - E_\gamma(k')) P_l(z_{k'p_i})} \right] \\ &+ \sum_{i=1}^{N} w_i \left[\frac{p_i^2 V^N_{\beta\gamma}(k', p_i) T_{\gamma\alpha}(p_i, k)}{E - E_\gamma(p_i)} - \Theta_\gamma \frac{2\rho_\gamma k_{0\gamma}^2 V^N_{\beta\gamma}(k', k_{0\gamma}) T_{\gamma\alpha}(k_{0\gamma}, k)}{k_{0\gamma}^2 - p_i^2} \right] \\ &+ \frac{k'^2 S_{\beta\gamma}(k') T_{\gamma\alpha}(k', k)}{E - E_\gamma(k')} - i\Theta_\gamma \pi \rho_\gamma k_{0\gamma} V^N_{\beta\gamma} T_{\gamma\alpha}(k_{0\gamma}, k) \end{aligned} \tag{3.61}$$

The step-function Θ_γ, which equals to 1 for the open channels and 0 for the close channels, is inserted because we do not make the principle value subtraction in the closed channels. The superscript l of $S^l_{\beta\gamma}$ is suppressed with the understanding we always solve the Lippman-Schwinger Equation in the one-dimensional form.

With this subtraction method, Eq. (3.34) becomes

$$\begin{aligned} T_{\beta\alpha}(k', k) &= V^C_{\beta\gamma}(k', k) + V^N_{\beta\gamma}(k', k) + \frac{2}{\pi} \frac{k'^2 S_{\beta\gamma}(k') T_{\gamma\alpha}(k', k)}{E - E_\gamma(k')} \\ &+ \frac{2}{\pi} \sum_\gamma \sum_{i=1}^{N} w_i V^C_{\beta\gamma}(k', p_i) \left[\frac{p_i^2 T_{\gamma\alpha}(p_i, k)}{E - E_\gamma(p_i)} - \frac{k'^2 T_{\gamma\alpha}(k', k)}{(E - E_\gamma(k')) P_l(z_{k'p_i})} \right] \end{aligned}$$

$$+\frac{2}{\pi}\sum_{i=1}^{N} w_i \left[\frac{p_i^2 V^N_{\beta\gamma}(k',p_i)T_{\gamma\alpha}(p_i,k)}{E-E_\gamma(p_i)} - \Theta_\gamma \frac{2\rho_\gamma k_{0\gamma}^2 V^N_{\beta\gamma}(k',k_{0\gamma})T_{\gamma\alpha}(k_{0\gamma},k)}{k_{0\gamma}^2 - p_i^2}\right]$$
$$-2i\Theta_\gamma\rho_\gamma k_{0\gamma} V^N_{\beta\gamma} T_{\gamma\alpha}(k_{0\gamma},k) \tag{3.62}$$

Next we define the matrix elements of V^C as

$$V^C_{n\gamma,m\gamma} = \begin{cases} V^C_{\gamma\gamma}(p_n,p_m) & n,m=1\ldots N \text{ and } n\neq m \\ \left(S_{\gamma\gamma}(p_n) - \sum_{i\neq n}\frac{w_i V^C_{\gamma\gamma}(p_n,p_i)}{P_l(z_{p_i p_n})}\right)\Big/ w_i & n=m=1\ldots N \\ 0 & n=N+1 \text{ or } m=N+1 \end{cases} \tag{3.63}$$

and use Eq. (3.42) as the definition of V^N, Eq. (3.43) as the definition of T, and Eq. (3.44) as the definition of G. We obtain

$$T_{n\beta,m\alpha} = V^N_{n\beta,m\alpha} + V^C_{n\beta,m\alpha} + \sum_\gamma \sum_{i=1}^{N+1} \left(V^N_{n\beta,i\gamma} + V^C_{n\beta,i\gamma}\right) G_{i\gamma} T_{i\gamma,m\alpha} \tag{3.64}$$

Eq. (3.64) can be expressed in the matrix form

$$(1-VG)T = V \tag{3.65}$$

$$V = V^C + V^N \tag{3.66}$$

The condition for T having a pole at energy E is the complex equation

$$\det(1-VG) = 0 \tag{3.67}$$

In practice, the real part and the imaginary part of this equation are solved simultaneously for the position of the pole on the complex energy plane. We use the "charge basis" (see Table 5 for the meaning of each channel) for the Coulomb plus the CBM potential. The Coulomb potential only occurs in K^-p channel, or channel 1.

For the case of nuclear potential only, we use the same procedure but without the Kwon-Tabakin-Lande subtraction in any of the channels.

3.4 Numerical Method

The computation for T-matrix elements or searching for the pole positions is very numerically intensive. Therefore, it is valuable to find a more economical method for the task. We have done that by noticing that the potential matrix V is often symmetric due to the symmetry principle in the physics. Special methods are developed to take the advantage of the symmetry of the potential matrix. We will discuss the new methods in the rest of this section.

3.4.1 Searching for Pole Positions

When searching for pole positions, the computation time can be saved dramatically by utilizing the symmetric property of potential matrix V[63]. To start, we write Eq. (3.67) as

$$\det\left[\delta_{ij} - V_{ij}G_j\right]_{M\times M} = 0 \tag{3.68}$$

where V and G were defined before. We take $M = nch\times(N+1)$ as the size of our "super" matrices. First we notice that the matrix G is a diagonal matrix. If none of the elements of G are zero, the reformulation is particularly simple. After we factor out all elements of G, Eq. (3.68) becomes

$$P \times D = 0 \tag{3.69}$$

where

$$P = \prod_j G_j \tag{3.70}$$

and

$$D = \det\left[\delta_{ij}G_j^{-1} - V_{ij}\right]_{N\times N} \tag{3.71}$$

If needed, the calculation of P would be very easy. More important, the calculation of D—which is all that is needed to determine the eigenenergies—now requires only the evaluation of a *symmetric* complex matrix instead of a general complex matrix.

If there are some elements of G which vanish, the reformulation is more complicated, but still possible. For example, consider the case in which the lth element of G vanishes while none of the others do. In this case the lth column of the matrix in Eq. (3.68) looks like

$$\begin{bmatrix} 0 \\ \vdots \\ 1 \\ \vdots \\ 0 \end{bmatrix} \cdots\cdots l\text{th row} \tag{3.72}$$

We can thereby eliminate all other elements on the lth row without changing the value of the determinant. Specifically, we define

$$G'_j = \begin{cases} 1 & \text{if } j = l \\ G_j & \text{otherwise} \end{cases} \tag{3.73}$$

and

$$V'_{ij} = \begin{cases} 0 & \text{if } i = l \text{ or } j = l \\ V_{ij} & \text{otherwise} \end{cases} \tag{3.74}$$

Eq. (3.68) is then equivalent to

$$\det \left[\delta_{ij} - V'_{ij} G'_j\right]_{N \times N} = 0 \tag{3.75}$$

Since there are no elements of G'_j which vanish, and the potential is symmetric,

$$V'_{ij} = V'_{ji} \tag{3.76}$$

Eq. (3.75) is equivalent to Eq. (3.68) and the symmetric Eq. (3.71) $D = 0$ can be used.

3.4.2 Solving for T-Matrix Elements

Following the same line of reasoning as used in searching for pole positions, the computation time for solving the Lippman-Schwinger equation for the T-matrix elements can also be dramatically reduced.

The numerical solution of Lippman-Schwinger Eq. starts from Eq. (3.46). In the simplest case, if none of the elements of G is zero, everything is very easy. Eq. (3.46) can be reformulated as

$$(G^{-1} - V)(GT) = V \tag{3.77}$$

Since $G^{-1} - V$ is a symmetric matrix, we can now solve a symmetric linear system of equations for GT first, which is much faster than to solve a general system. From GT we can easily obtain the value of T since G is a diagonal matrix and its inverse is very quick to calculate on the computer.

If there are some elements of G which vanish, the reformulation is a little more complicated. For example, consider the case in which the last element of G vanishes when none of the others do (if the vanishing one is not the last element, we can always rearrange the order of the column and row to make

it last one without changing the final answer). The linear system looks like

$$\begin{bmatrix} 1-vg & 0 \\ -v_r g & 1 \end{bmatrix} \begin{bmatrix} t & t_c \\ t_r & t_M \end{bmatrix} = \begin{bmatrix} v & v_c \\ v_r & v_M \end{bmatrix} \tag{3.78}$$

Here the matrix v is an $(M-1)\times(M-1)$ *symmetric* matrix, the matrix g is a $(M-1)\times(M-1)$ diagonal matrix, the matrix t is a $(M-1)\times(M-1)$ matrix, v_r and t_r are $(M-1)\times 1$ row matrices, v_c and t_c are $(M-1)\times 1$ column matrices, and v_M and t_M are the lower right corner elements of V and T. We now split the system (3.78) into the following:

$$(1-vg)t = v \tag{3.79}$$

$$(1-vg)t_c = v_c \tag{3.80}$$

$$-v_r g t + t_r = v_r \tag{3.81}$$

$$-v_r g t_c + t_M = v_M \tag{3.82}$$

We can now solve for t and t_c first with *symmetric* v matrix first (which is also faster), and then come back to solve for t_r and t_M if needed.

If there are more than one elements in G which vanish, we can follow the procedure recursively and finally solve a symmetric system instead of a general system.

3.4.3 Timing Benchmark

The computing time saved by this new method are considerable. For instance, for calculating the energy of the kaonic hydrogen $1S$ level, the new method took 1716 seconds of CPU time on a Ridge Turbo computer whereas the old one took 2988 seconds. In both methods, the final result is the same,

$(-239.9, 1207.5)$ eV for shift and width. For the case of calculating T-matrix elements, the direct LU decomposition method took 1214 second on the RISC System/6000 Model-530 to calculate a set of scattering amplitudes while the new method took 493 seconds to give the same results.

Chapter 4

The Fitting Procedure

There are several parameters contained within the CBM description of the $\bar{K}N$ interactions. We determine these parameters by fitting the scattering and other observables predicted by this model to the experimental data. In this thesis work we studied different kinds of data including the K^-p scattering sections [37, 38, 39, 40, 41, 42, 43, 44, 45, 46], the K^-p threshold branching ratios, the $\pi\Sigma$ mass spectrum for $K^-p \to \pi^+\pi^-(\Sigma^-\pi^+)$, and the $\pi^0\Lambda$ mass spectrum for $K^-p \to \pi^+\pi^-(\pi^0\Lambda)$. In the rest of this chapter, we will first shown how to compute these experimental observables from the CBM theory. Then, we will introduce the procedures of fitting the model parameters against these data.

4.1 K^-p Scattering Cross Sections

Even at low energy, the K^-p scattering process has many different, coupled final states.

$$K^-p \longrightarrow \begin{cases} K^-p \\ \bar{K}^0 n \\ \pi^+\Sigma^- \\ \pi^0\Sigma^0 \\ \pi^-\Sigma^+ \\ \pi^0\Lambda \end{cases} \tag{4.1}$$

There are yet other channels, but their branching ratios are so small that we assume we can ignore their coupling without significantly change of the physics.

The low energy K^-p scattering cross sections have been measured for several decades. The most common method of measuring the cross sections are the bubble chamber experiments. For a typical bubble chamber experiment, a beam of antikaons is introduced into a superheated liquid hydrogen chamber. The charged particles (including the K^-, Σ's from the interaction) cause the liquid hydrogen to boil and forms bubble trails. The particles and accordingly the trails are bent in a magnetic field to assist particle identification. Tens of thousands of photographs of these trails are taken, and the path length of the antikaons are measured. The total cross section is calculated by the formula[38]

$$I = I_0 e^{-\sigma \rho x} \tag{4.2}$$

and

$$\sigma_i^j = \frac{n_i^j}{l_i}\left(\frac{A}{\rho N_0}\right) \tag{4.3}$$

where $(\rho N_0/A)$ is the number of protons per unit volume, l_i is the observed K^- path length in the ith momentum bin, n_i^j is the number of interactions of the jth event type in the ith momentum bin, and finally, σ_i^j is the cross section for the production of event type j averaged over momentum bin i.

Experimentally the small angle scattering is excluded since it is dominated by the Coulomb interaction. The cutoff angle varies from experiment to experiment with 10° a typical value.

Scattering with very low laboratory momentum is not included since the length of the final particles' trails are so small as to make them indistinguishable from "at rest" events.

We have extended the TRIUMF's CBM $\bar{K}N$ interaction from S-wave only[35] to the S-, P-, and D-wave and analyzed data up to 520 MeV/c. Correspondingly we do not have to limit ourself to the very low energy as occurring with only S-wave. This is important since it has been reported that even at K^- lab momenta as low as 150 MeV/c, there are P-wave contributions in the reactions $K^-p \rightarrow \pi^{\pm}\Sigma^{\mp}$[45]. Also, at K^- momenta around 390 MeV/c, there is a clear signal of $\Lambda(1520)$ which is a D-wave resonance[37]. The data (either read from tables or off graphs) are from references[37, 38, 39, 40, 41, 42, 43, 44, 45, 46] and are plotted in Fig. 5, 6, 7, 8, 9, and 10. We see from these plot that there are considerable errors, especially at low momenta where the tracks are short and the Coulomb correction large. This clearly indicates the need for a statistical fit.

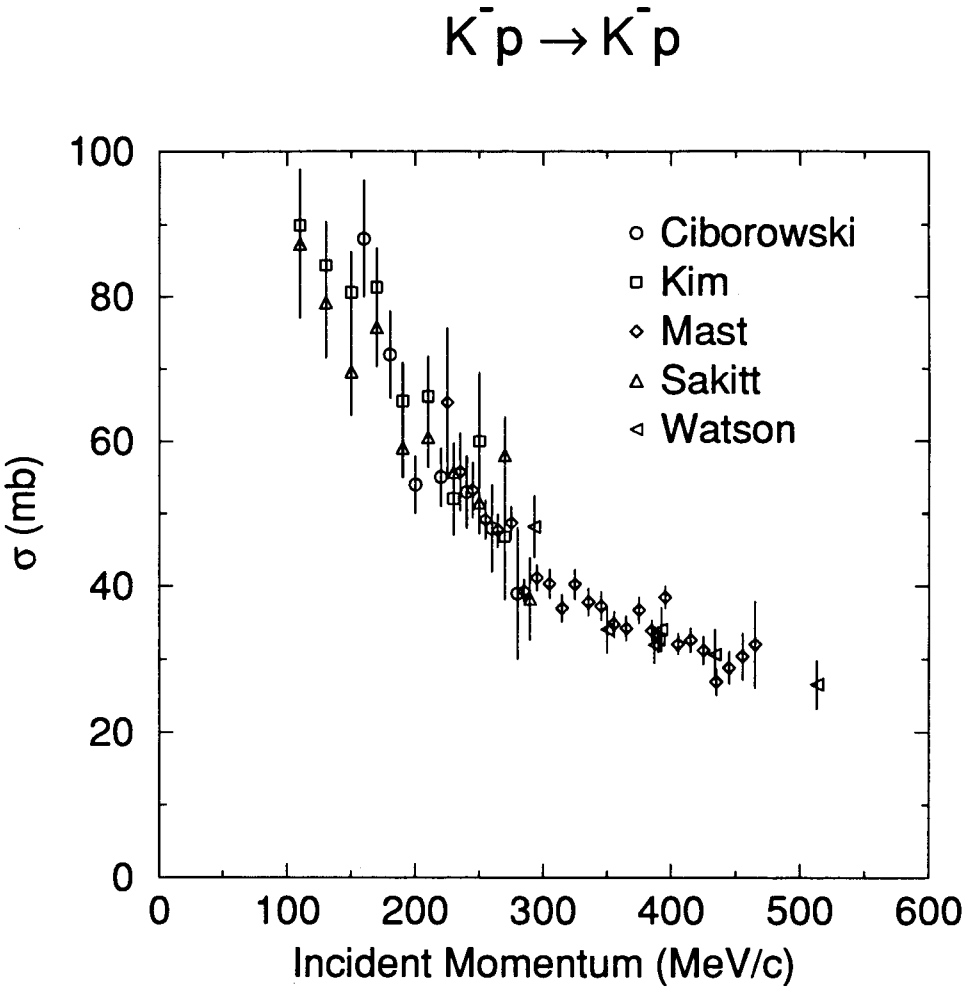

Figure 5. The $K^-p \rightarrow K^-p$ elastic scattering cross sections with incident momentum below 520 MeV/c.

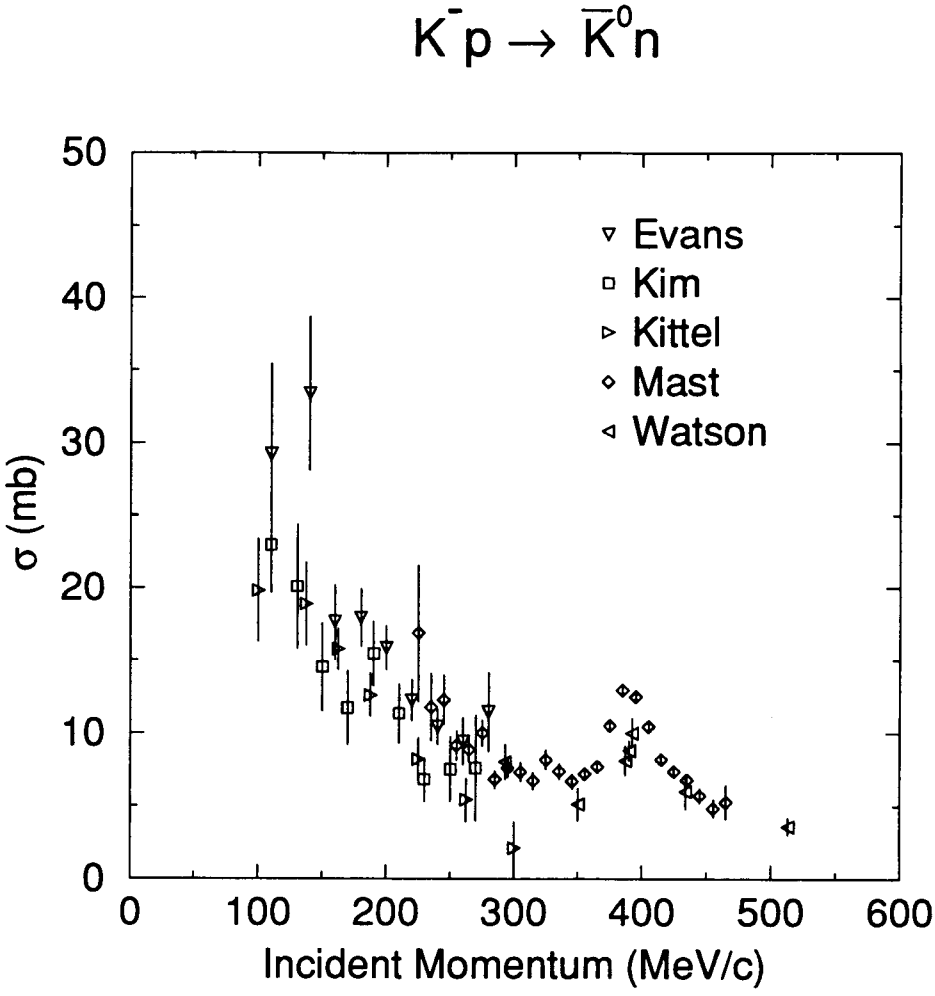

Figure 6. The $K^- p \rightarrow \bar{K}^0 n$ charge exchange scattering cross sections with incident momentum below 520 MeV/c.

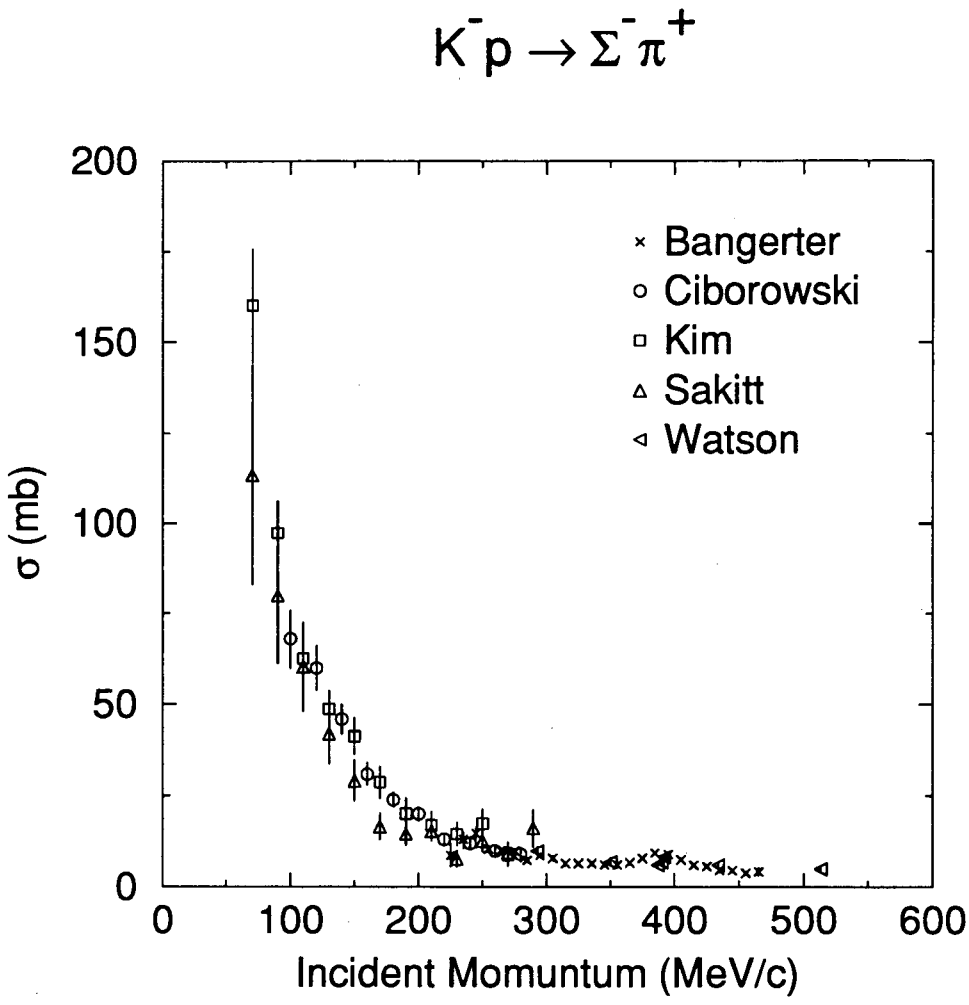

Figure 7. The $K^- p \rightarrow \pi^+ \Sigma^-$ reaction scattering cross sections with incident momentum below 520 MeV/c.

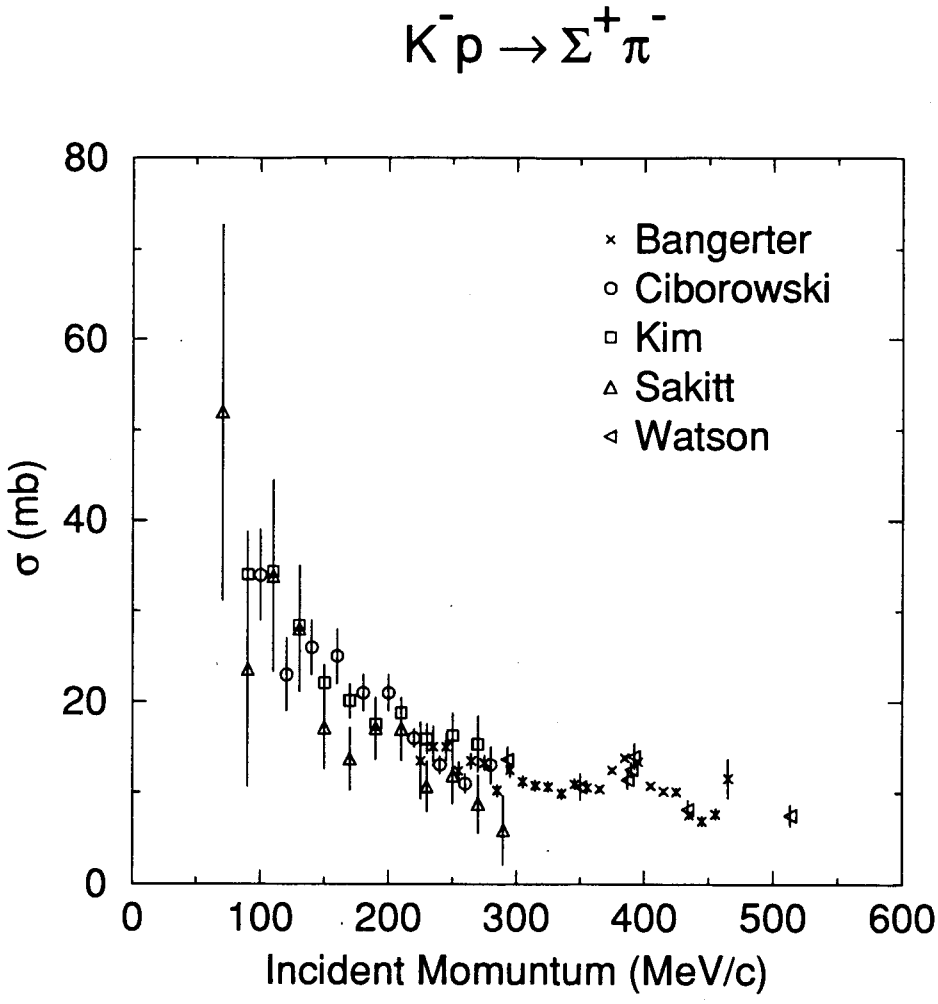

Figure 8. The $K^- p \rightarrow \pi^- \Sigma^+$ reaction scattering cross sections with incident momentum below 520 MeV/c.

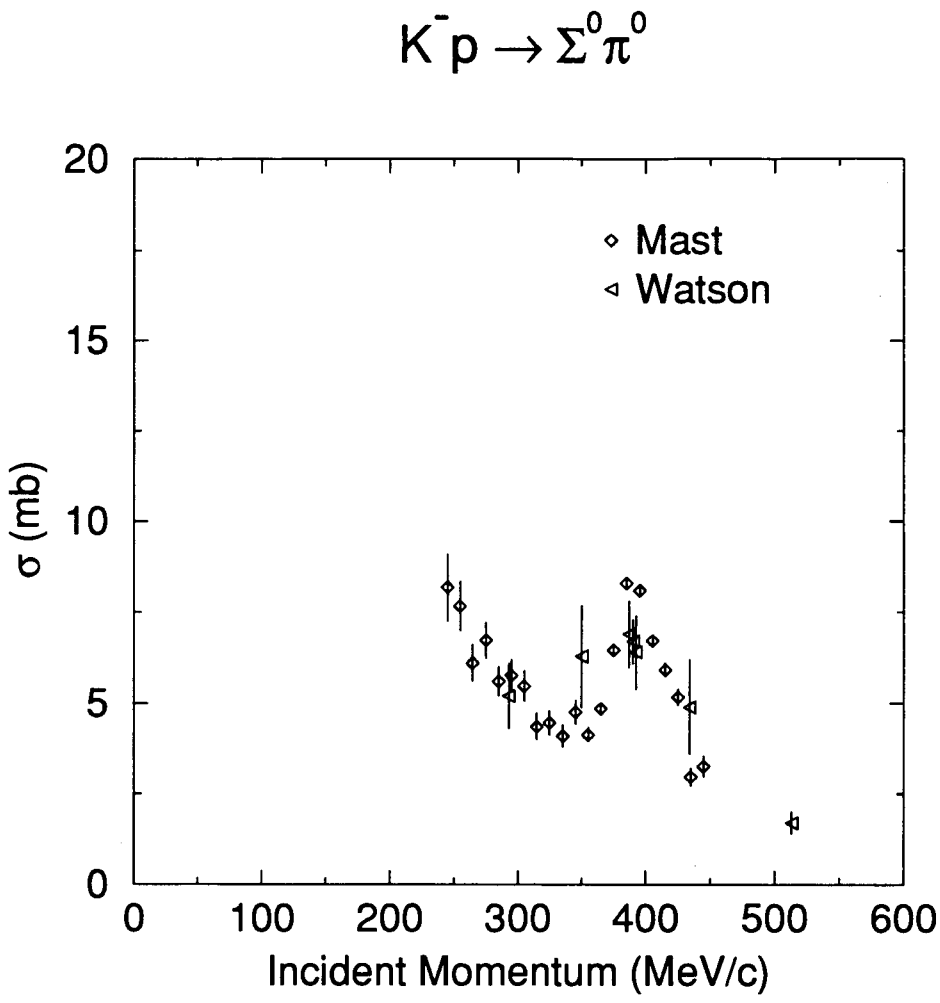

Figure 9. The $K^- p \rightarrow \pi^0 \Sigma^0$ reaction scattering cross sections with incident momentum below 520 MeV/c.

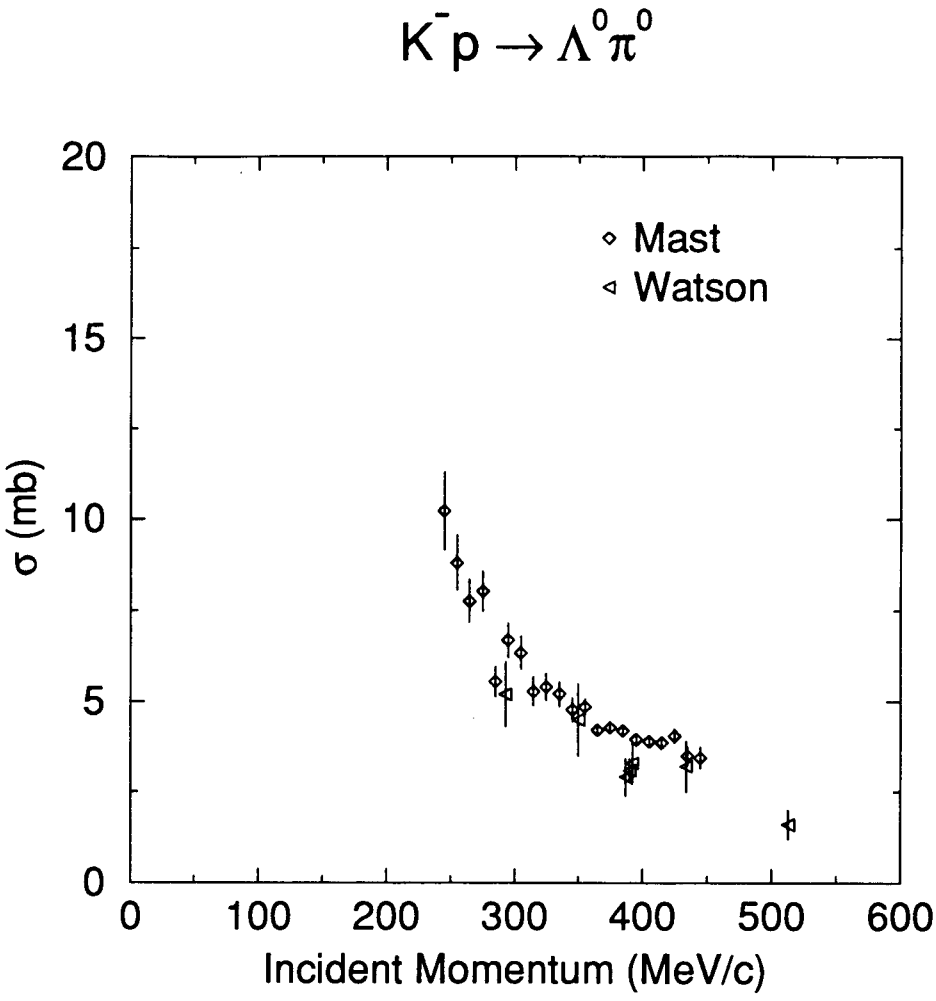

Figure 10. The $K^- p \rightarrow \pi^0 \Lambda$ reaction scattering cross sections with incident momentum below 520 MeV/c.

In Chapter 3, we have already described how we solved the coupled-channel Lippman-Schwinger equation (3.29) for the T-matrix elements. The differential cross sections are related to the T-matrix elements by

$$\frac{d\sigma_{\beta\alpha}}{d\Omega} = 16\pi^4 \rho_\beta \rho_\alpha \frac{k'}{k} \overline{\sum_{\mu',\mu}} |T_{\beta\alpha}(\mathbf{k}'\mu', \mathbf{k}\mu)|^2 \tag{4.4}$$

where the bar over the summation means that it is the sum over final spin states and average over the initial spin states. The ρ's are the "reduced mass" defined in Eq. (3.37). The momentum for incoming channel α and outgoing channel β are labeled as k and k'. The total cross sections, defined as the integral of differential cross sections over the solid angle, are

$$\sigma_{\beta\alpha} = \int d\Omega \, \frac{d\sigma}{d\Omega} \tag{4.5}$$

Using the reverse transformation of Eq. (3.32), we have

$$\begin{aligned} & T_{\beta\alpha}(\mathbf{k}'\mu', \mathbf{k}\mu) \\ &= \frac{1}{2\pi^2} \sum_l \left[(l+1) T^{l+}_{\beta\alpha}(k', k) + l T^{l-}_{\beta\alpha}(k', k) \right] \delta_{\mu'\mu} P_l(\cos\theta) \\ &\quad + \frac{1}{2\pi^2} \sum_l \left[T^{l+}_{\beta\alpha}(k', k) - T^{l-}_{\beta\alpha}(k', k) \right] \langle \mu' | i\boldsymbol{\sigma} \cdot (\hat{k} \times \hat{k}') | \mu \rangle P'_l(\cos\theta) \end{aligned} \tag{4.6}$$

Substituting the above relation into the total cross sections yields

$$\sigma_{\beta\alpha} = 16\pi \rho_\beta \rho_\alpha \frac{k'}{k} \sum_{l=0}^{\infty} \left[(l+1) \left| T^{l+}_{\beta\alpha}(k', k) \right|^2 + l \left| T^{l-}_{\beta\alpha}(k', k) \right|^2 \right] \tag{4.7}$$

In practice, the computation is always carried out in the "charge basis" to permit a direct comparison to data (See Table 5 for the channel assignment). The incoming channel is always $K^- p$, or channel number 1. The outgoing channel varies depending on the reaction measured. For the $K^- p$ elastic

scattering and $K^-p \to \bar{K}^0 n$ charge exchange reaction, the outgoing channels are 1 and 2:

$$\sigma(K^-p \leftarrow K^-p) = 16\pi\rho_1^2 \sum_{l=0}^{2} \left[(l+1)\left|T_{11}^{l+}(k',k)\right|^2 + l\left|T_{11}^{l-}(k',k)\right|^2\right] \quad (4.8)$$

$$\sigma(\bar{K}^0 n \leftarrow K^-p) = 16\pi\rho_1\rho_2\frac{k'}{k} \times \sum_{l=0}^{2} \left[(l+1)\left|T_{21}^{l+}(k',k)\right|^2 + l\left|T_{21}^{l-}(k',k)\right|^2\right] \quad (4.9)$$

The $\pi\Sigma$ channels requires a few more steps. Even though we solve the Lippman-Schwinger equation (3.34) in the "charge basis", the T-matrix elements related to $\pi\Sigma$ channels are always formulated in the isospin basis. To calculate the scattering cross section, we need first to add the amplitudes coherently, and then take the sum of the square of the moduli. With the explicit form of the Clebsch-Gordan coefficients, we have

$$\sigma(\Sigma^+\pi^- \leftarrow K^-p) = 16\pi\rho_3\rho_1\frac{k'}{k}\sum_{l=0}^{2}\left[(l+1)\left|\frac{1}{\sqrt{3}}T_{31}^{l+}(k',k) + \frac{1}{\sqrt{2}}T_{41}^{l+}(k',k)\right|^2 + l\left|\frac{1}{\sqrt{3}}T_{31}^{l-}(k',k) + \frac{1}{\sqrt{2}}T_{41}^{l-}(k',k)\right|^2\right] \quad (4.10)$$

$$\sigma(\Sigma^0\pi^0 \leftarrow K^-p) = 16\pi\rho_3\rho_1\frac{k'}{k}\sum_{l=0}^{2}\left[(l+1)\left|\frac{1}{\sqrt{3}}T_{31}^{l+}(k',k)\right|^2 + l\left|\frac{1}{\sqrt{3}}T_{31}^{l-}(k',k)\right|^2\right] \quad (4.11)$$

$$\sigma(\Sigma^-\pi^+ \leftarrow K^-p) = 16\pi\rho_3\rho_1\frac{k'}{k}\sum_{l=0}^{2}\left[(l+1)\left|\frac{1}{\sqrt{3}}T_{31}^{l+}(k',k) - \frac{1}{\sqrt{2}}T_{41}^{l+}(k',k)\right|^2 + l\left|\frac{1}{\sqrt{3}}T_{31}^{l-}(k',k) - \frac{1}{\sqrt{2}}T_{41}^{l-}(k',k)\right|^2\right] \quad (4.12)$$

The $\pi^0\Lambda$ T-matrix elements are computed in the charge basis with $\pi^0\Lambda$ being the channel number 5. Accordingly, the cross section for $K^-p \to \pi^0\Lambda$ is

$$\sigma(\pi^0\Lambda \leftarrow K^-p) = 16\pi\rho_5\rho_1\frac{k'}{k}\sum_{l=0}^{2}\left[(l+1)\left|T_{51}^{l+}(k',k)\right|^2 + l\left|T_{51}^{l-}(k',k)\right|^2\right] \tag{4.13}$$

4.2 The $\Lambda(1405)$ Resonance

Strongly coupled to $(\pi\Sigma)^0$ channels and lying about 30 MeV below the $\bar{K}N$ threshold, lies the $\Lambda(1405)$ resonance, an $I = 0$ state of the $S = -1$, and $J^P = \frac{1}{2}^-$[64]. Since $\pi\Sigma$ scattering is not directly accessible to experiment, this resonance can be observed directly only in the $(\pi\Sigma)^0$ system of the final states of production experiments. It was first reported by Alston in the reaction $K^-p \to \Sigma\pi\pi\pi$ at 1.15 GeV/c[65]. By now this resonance has been seen in many other experiments. Thomas[51] reported a respectable signal for $\Lambda(1405)$ in the reaction $\pi^-p \to (\Sigma^\pm\pi^\mp)K^0$ at 1.69 GeV/c. However, the cleanest and highest statistics sample of $\Lambda(1405)$ was obtained from the reaction $K^-p \to \pi^-\pi^+(\pi\Sigma)^0$ at 4.2 GeV/c by Hemingway[52]. In Hemingway's experiment, the K^- beam of 4.2 GeV/c is introduced to the CERN 2m hydrogen bubble chamber and the reactions $K^-p \to \Sigma^+(1660)\pi^-$, $\Sigma^+(1660) \to \Lambda(1405)\pi^+$, and $\Lambda(1405) \to (\pi\Sigma)^0$ are used to isolate the $\Lambda(1405)$ signal. The $\Sigma^+\pi^-$ mass distribution is read off the Fig. 4 of Ref. [52] and plotted in as Fig. 11 in this thesis. Notice that we did not plot the error bar in Fig. 11. In the original paper, only 7 error bars were given for the total of 14 energy bins. Only those data with error bar are used in the

fitting procedure. The rest of data are used for determine the total number of events (therefore the normalization of the theoretical curve).

Although the experimental signal of $\Lambda(1405)$ is clear, the theoretical interpretation of its nature is not totally clear. Due to its strong coupling to $\pi\Sigma$ channels and close proximity to the $\bar{K}N$ threshold, the $\Lambda(1405)$ resonance dominates the low energy $\bar{K}N$ system. Over the years, much theoretical works has been done on the description of $\Lambda(1405)$[66, 67, 68, 35, 69, 70, 71, 72]. The following are some of the possible interpretations of the nature of the $\Lambda(1405)$: The $\Lambda(1405)$ is (a) a three-quark s-channel resonance, (b) a quasi-bound-state of the $\bar{K}N$ system, (c) some kind combination of case (a) and (b). In this thesis, we follow the method used in Ref. [35]. We let the $\bar{K}N$ system couple to a three-quark bag with the correct quantum number of $\Lambda(1405)$, then fit the $\pi\Sigma$ mass spectrum for $K^-p \to \Sigma\pi\pi\pi$ at 4.2 GeV/c[52] within the model, and finally use the deduced fit to determine the nature of $\Lambda(1405)$.

In Chapter 3, we have already described how the bare three-quark state couples to the $\bar{K}N$ system via the interaction $v^{(a)}(\mathbf{k}'\mu', \mathbf{k}\mu)$ (the Feynman diagram is shown in Fig. 4). To calculate the $\pi\Sigma$ mass spectrum, we use the impulse approximation together with a Watson final-state-interaction model[37, 72] to obtain the necessary matrix elements. There are accordingly a good number of assumptions in this model and a detailed reproduction of the data is not expected.

In the final state interaction model, the relative S-wave two-particle subsystem of a multi-particle final state is assumed to have the asymptotic wave

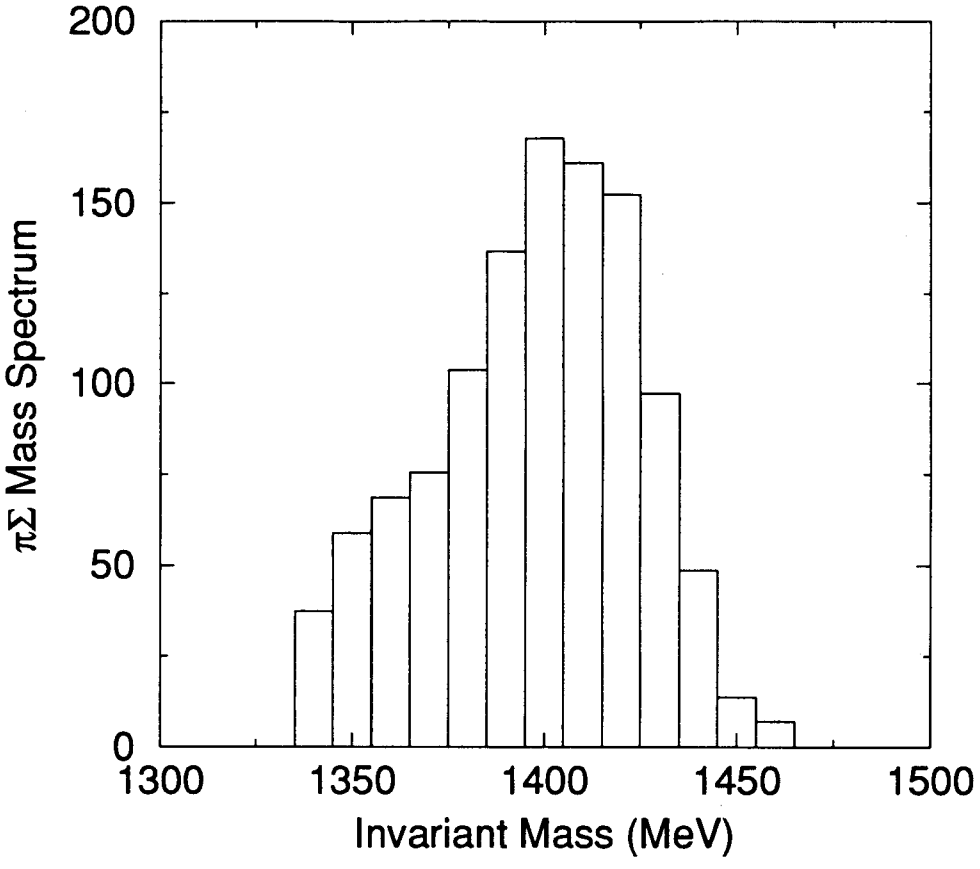

Figure 11. Hemingway's data of invariant mass distribution of the $\Sigma^+\pi^-$ system from the reaction $K^-p \to \Sigma^+\pi^-\pi^+\pi^-$ at 4.2 GeV/c.

function

$$\begin{aligned}\psi(\mathbf{r_1},\mathbf{r_2}) &\propto \exp[i\mathbf{Q}\cdot(\mathbf{r_1}+\mathbf{r_2})/2]\phi_{as}(\mathbf{r}) \\ &= \exp[i\mathbf{Q}\cdot(\mathbf{r_1}+\mathbf{r_2})/2]\sin(kr+\delta)\frac{e^{i\delta}}{kr} \qquad (4.14)\end{aligned}$$

where $r = |\mathbf{r_1} - \mathbf{r_2}|$ is the separation of the two particles, k is the relative momentum of the two particles in their COM system, and δ is the scattering phase shift. Inserting this wave function into the impulse approximation matrix element describing the reaction amplitude produces the matrix element

$$\begin{aligned}M &= \int d^3r_1 d^3r_2 \prod_a d^3r_a\, F(1,2;a)\psi(\mathbf{r_1},\mathbf{r_2}) \\ &= \int d^3r_1 d^3r_2 \prod_a d^3r_a\, F(1,2;a)\exp[i\mathbf{Q}\cdot(\mathbf{r_1}+\mathbf{r_2})/2] \\ &\quad \times\left(\frac{\sin kr}{kr}\cos\delta + \frac{\cos kr}{kr}\sin\delta\right)e^{i\delta} \qquad (4.15)\end{aligned}$$

where a includes all degrees of freedom other than particle pair $(1,2)$. The function $F(1,2;a)$ is a product of initial and final state wave functions for all particles except $(1,2)$.

If the $(1,2)$ interaction range is small relative to the size parameters in the wavefunction product $F(1,2;a)$, the momentum dependence of the integral (4.15) will be dominated by the second term. This means

$$M \propto \frac{\sin\delta e^{i\delta}}{k} \qquad (4.16)$$

This should be a good approximation to the k dependence of the matrix element if a resonance peaks in a narrow range of momentum.

Replacing the slowly-varying integral over F in the matrix element (4.15) by a constant, the rate of the $\pi\Sigma$ events, which is proportion to the square

of the matrix element, at energy E, is given by

$$\frac{dN}{dE} = C\frac{\sin^2\delta}{k^2}\rho(k,Q) \tag{4.17}$$

Here C is a factor independent to the momentum k, $\rho(k,Q)$ is the density of final states for particle $(1,2)$ with total momentum Q and it can be approximated by

$$\rho(k,Q) = kQ \tag{4.18}$$

Finally then, we have the number of events per unit energy interval as

$$\begin{aligned} \frac{dN}{dE} &\propto \frac{\sin^2\delta}{k} \\ &\propto k\,\sigma_{\pi\Sigma\leftarrow\pi\Sigma} && (4.19) \\ &\propto k\rho^2_{\pi\Sigma}\left|T^0_{33}(k,k)\right|^2 && (4.20) \end{aligned}$$

The overall normalization is not determined since, at best, the model gives the shape of the mass spectrum. In the practice, we fix the overall normalization by setting equal the area under the theoretical mass spectrum curve to the total event number in the experiment.

4.3 The $\Sigma(1385)$ Resonance

Discovered by Alston in 1960[73, 74], the $\Sigma(1385)$ is a P-wave resonance strongly coupled to the $\pi\Lambda$ channel. Similar to the $\Lambda(1405)$ resonance, the $\Sigma(1385)$ is below the $\bar{K}N$ threshold, and is best observed in the $\pi\Lambda$ system within the final states of production experiments. Aguilar-Benitez fitted the $\pi^0\Lambda$ mass spectrum for the reaction $K^-p \rightarrow \Lambda\pi^0\pi^+\pi^-$ at 4.2 GeV/c and gave five different fits to the $\Sigma(1385)$ resonance parameters[53]. In this thesis, we

are only interested in the neutral member of the $\Sigma(1385)$ triplet for the obvious reason that only it is reached by the K^-p scattering. The experimental $\pi^0\Lambda$ mass spectrum for the reaction $K^-p \to \Lambda\pi^0\pi^+\pi^-$ at 4.2 GeV/c is read off from the Fig. 10 of Ref. [53] and plotted as Fig. 12 in this thesis.

The theoretical calculation of the $\pi^0\Lambda$ mass spectrum is similar to the $\pi\Sigma$ mass spectrum of the $\Lambda(1405)$ resonance. We use again the Watson's final state interaction theorem. For the case of P-wave resonance, Eq. (4.16) becomes[37]

$$M \propto \frac{\sin\delta_l \, e^{i\delta_l}}{k^{l+1}} \tag{4.21}$$

where $l = 1$ for a P-wave resonance. The rate of production for $\pi^0\Lambda$ events now is

$$\frac{dN}{dE} = C\frac{\sin^2\delta_l}{k^{2(l+1)}}\rho(k,Q) \tag{4.22}$$

Replacing the density of states by kQ and letting $l = 1$, we obtain

$$\begin{aligned} \frac{dN}{dE} &\propto \frac{\sin^2\delta_1}{k^3} \\ &\propto \frac{\sigma_{\pi\Lambda\leftarrow\pi\Lambda}}{k} \qquad (4.23) \\ &\propto \frac{\rho^2_{\pi\Lambda}}{k}\left|T^{1+}_{55}(k,k)\right|^2 \qquad (4.24) \end{aligned}$$

One problem using the data from Ref. [53] is the large background. In the reference, the authors fitted the data with a polynomial background term and a resonance term, but they did not give the parameters of the background. We assumed a polynomial background as

$$f_{bk}(M) = a_0 + a_1\left(\frac{M}{M_0}\right) + a_2\left(\frac{M}{M_0}\right)^2 \tag{4.25}$$

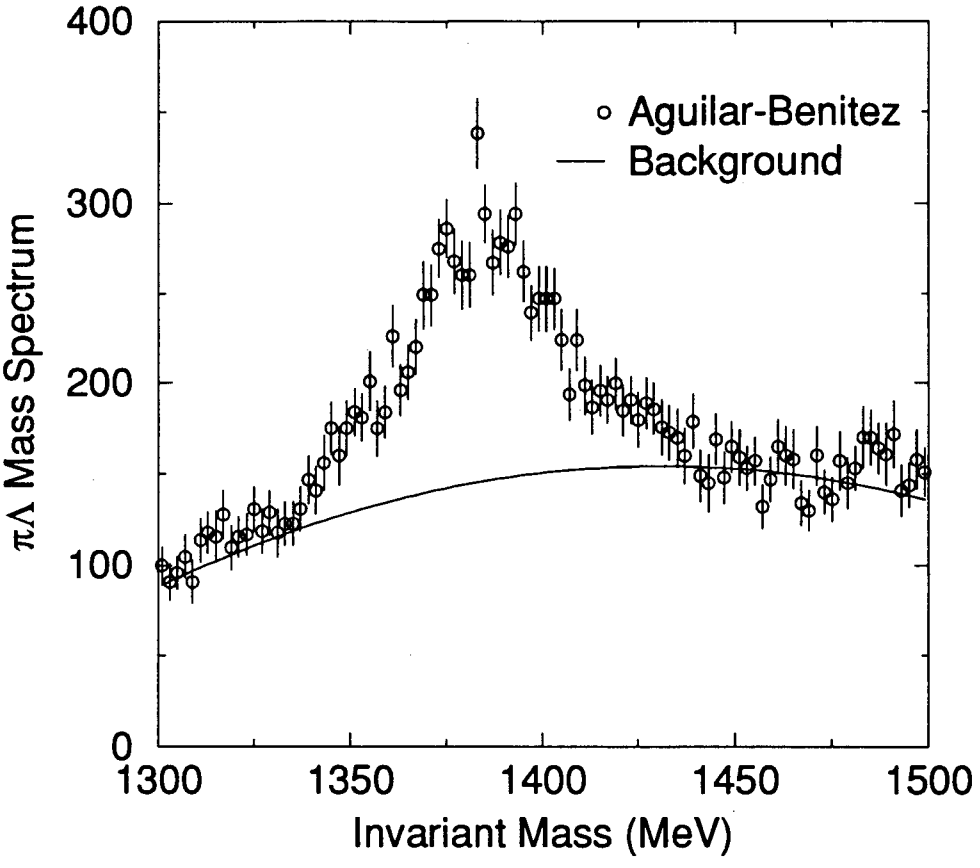

Figure 12. Aguilar-Benitez's data of invariant mass distribution of the $\pi^0\Lambda$ system from the reaction $K^-p \rightarrow \Lambda\pi^0\pi^+\pi^-$ at 4.2 GeV/c. The solid line is our polynomial fit to the background.

where M_0 is the mass of the resonance. To determine the background, a Breit-Wigner resonance form is added to it and the whole sum is used to fit the mass spectrum.

$$\frac{dN}{dM} = f_{bk}(M) + \frac{bM_0^2\Gamma_0^2}{(M-M_0)^2 + M_0^2\Gamma^2} \tag{4.26}$$

The mass and width of this Breit-Wigner form is given by the best fit of Ref. [53] with $M = 1384.1$ MeV and $\Gamma = 34.8$ MeV. The parameters are

$$\begin{aligned} a_0 &= -7754.73 \\ a_1 &= 15303.0 \\ a_2 &= -7402.42 \\ b &= 158.648 \end{aligned}$$

The background is subtracted from the original data and the output is used as the pure $\pi^0\Lambda$ spectrum for our final fitting program.

4.4 The K^-p Threshold Branching Ratios

Even at the zero momentum, the K^-p system is strongly coupled to the open channels, $\Sigma^{\pm,0}\pi^{\mp,0}$, $\pi^0\Lambda$, and K^-p itself. The threshold decay branching ratios of the K^-p atom are defined as

$$\gamma = \frac{\text{rate}(K^-p \to \Sigma^-\pi^+)}{\text{rate}(K^-p \to \Sigma^+\pi^-)} \tag{4.27}$$

$$R_c = \frac{\text{rate}(K^-p \to \text{charged particles})}{\text{rate}(K^-p \to \text{all final states})} \tag{4.28}$$

$$R_n = \frac{\text{rate}(K^-p \to \pi^0\Lambda)}{\text{rate}(K^-p \to \text{all neutral states})} \tag{4.29}$$

	γ	R_c	R_n
Humphrey		0.655 ± 0.011	0.186 ± 0.017
Tovee	2.34 ± 0.08		
Nowak	2.35 ± 0.07	0.664 ± 0.011	
Goossens			0.206 ± 0.015

Table 8. The K^-p zero momentum branching ratio data.

These branching ratios have been reported by different groups[47, 48, 49, 50]. Some of the data are tabulated in Table 8.

Numerically, it is not possible to calculate the decay rate of the K^-p system at zero energy. The method we used is to calculate the K^-p scattering cross section at very low energies E to find a set of branching ratio at finite energies. And then decreasing the absolute value of E until the the branching ratios stabilized on their limit, which is used as the theoretical values of the branching ratios.

The threshold branching ratios are very sensitive to the method for including isospin symmetry breaking. In our CBM, we assume isospin is good and only break it by using physical masses for the antikaons and nucleons at calculation stage. We thus do not expect our model to give the branching ratio close to the experimental data.

4.5 Fitting The Experimental Data

Earlier in this chapter, we discussed the experiments which studied the low energy $\bar{K}N$ interactions and how we would calculate these physical observables measured in the experiments. In this thesis, we tested how well the CBM could reproduce these data by actually searching for the best fit to the data.

There are four groups of experimental data included in our fitting. The first is K^-p scattering cross sections up to 520 MeV/c of K^- laboratory momentum, including elastic scattering, charge exchange, and reactions to $\pi\Sigma$, $\pi\Lambda$ channels [37, 45, 46, 41, 42, 43, 44, 38, 40]. This group contributes the largest number of data points to the fit.

The second data group is the $\Sigma^+\pi^-$ mass spectrum for the reaction $K^-p \rightarrow \Sigma^+\pi^-\pi^+\pi^-$ at 4.2 GeV/c[52]. These are the data which signal the existence of $\Lambda^*(1405)$.

The third group is the zero-energy decay branching ratios of the K^-p atom[47, 49, 50]. And the last group of data is the mass spectrum of $\pi^0\Lambda$ in the reaction $K^-p \longrightarrow \Lambda\pi^0\pi^+\pi^-$[53]. These data indicate the $\Sigma^0(1385)$ resonance .

There are 7 different independent parameters in the CBM. They are the radius of the bag R, the bare masses of the 3 resonances, m_s^* for $\Lambda(\frac{1}{2}^-)$, m_p^* for $\Sigma(\frac{3}{2}^+)$, and m_d^* for $\Lambda(\frac{3}{2}^-)$, and finally, the 3 coupling constants, $f_{I=0}$ for all isospin 0 channels, $f_{I=1}^K$ for all isospin 1 channels with kaons, and $f_{I=1}^\pi$ for isospin 1 channels with pions. It is quite a challenge to fit all these data well with only 7 parameters. The goodness of the fitting is a measure of how

Data Type	Number of Data Point
Scattering	300
$\pi\Sigma$ Spectrum	7
Branching Ratios	3
$\pi\Lambda$ Spectrum	200

Table 9. A list of different data type and number of data points in each of them.

good we understand the $\bar{K}N$ interaction and the CBM. Since we must solve coupled integral equation to calculate observables, it is also numerically very intensive to run these fit on a computer.

The chi-square is defined as

$$\chi^2 = \sum_g \sum_i \left(\frac{f_{g,i}^{th} - f_{g,i}^{exp}}{\sigma_{g,i}} \right)^2 \tag{4.30}$$

where g is the index for different data groups, $f_{g,i}^{exp}$ is the experimental value of ith point in data group g, $\sigma_{g,i}$ is the experimental error of this observable, and $f_{g,i}^{th}$ is the corresponding theoretical calculation of this observable from the CBM. We minimize the χ^2 by searching in a multidimensional parameter hyperspace using the 'snls1' subroutine of the Core Math Library (CMLIB) from National Institute of Standards and Technology.

Because of the large difference between the number of data points of different type of data, (7 points for $\pi\Sigma$ mass spectrum and 300 points for K^-p scattering data), and apparent inconsistency in the estimates of error

of different groups, we often find one type of data overwhelmed by others. To give a fair chance to different data types, we did some variations to the standard χ^2 fit. Basically, we manual adjusted the weight factors for various data groups and then repeated the chi-square minimization. The new chi-square, we call it χ^2_v is defined as

$$\chi^2_v = \sum_g \sum_i \left(\frac{f^{th}_{g,i} - f^{exp}_{g,i}}{w_g \sigma_{g,i}} \right)^2 \tag{4.31}$$

We can see that Eq. (4.30) is a special case of Eq. (4.31) with all $w_g = 1$.

4.5.1 Fit 1

First, we fit the low energy K^-p scattering cross sections with only the S-wave CBM. By "low energy", we mean the laboratory momentum for scattering below 250 MeV/c. This set of data has been used by most other groups in their study of the S-wave K^-p interactions. The center-of-momentum energies of the scattering system range from the K^-p threshold of 1432 MeV up to 1470 MeV. This set of data should not have much influence on the resonances such as $\Lambda^*(1405)$, $\Lambda^*(1520)$, and $\Sigma^*(1385)$. The parameters from this fit is listed in Table 11. The theoretical calculation of the different scattering cross sections and mass spectra are shown in Figures 13-19, and the branching ratios are listed in Table 10.

4.5.2 Fit 2

This is a straight χ^2 fit to the low energy scattering data and the $\pi\Sigma$ mass spectrum data of $K^-p \longrightarrow \Sigma\pi\pi\pi$[52], all within the S-wave only Cloudy Bag

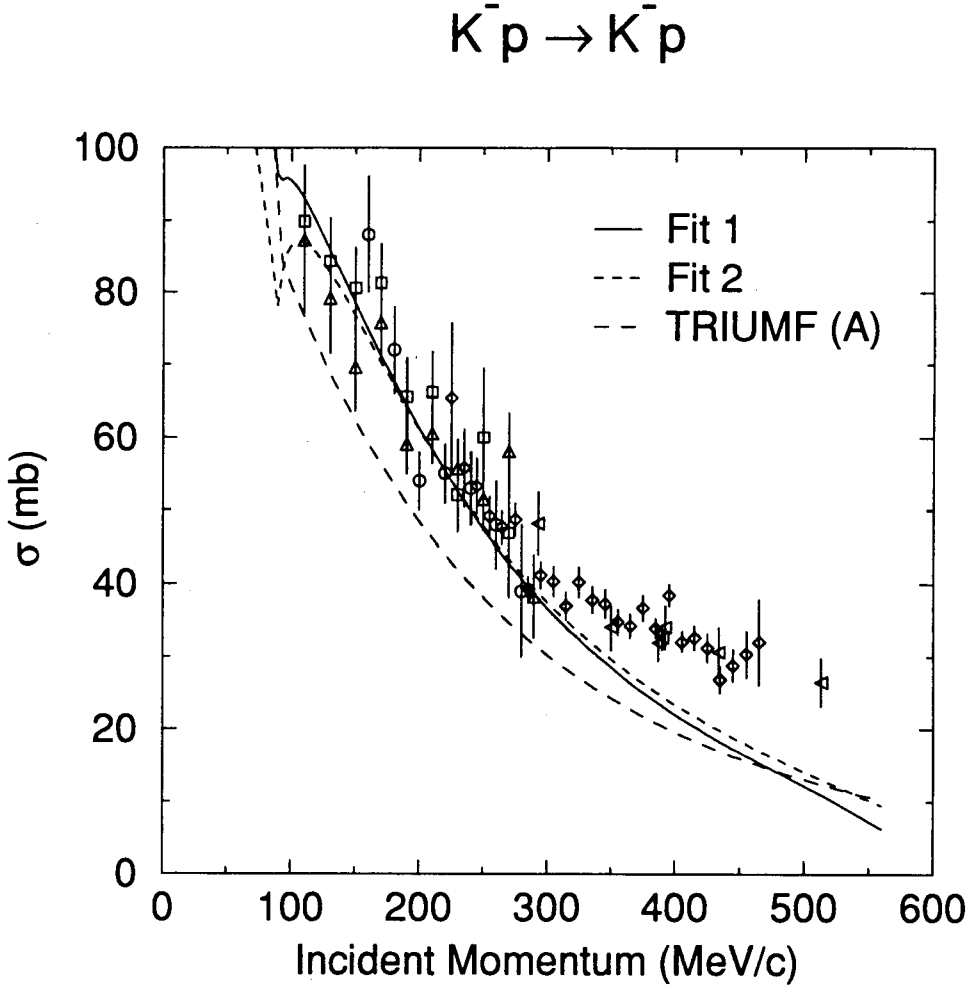

Figure 13. The $K^-p \rightarrow K^-p$ elastic scattering cross sections calculated by the CBM with the parameter sets from the low energy fits.

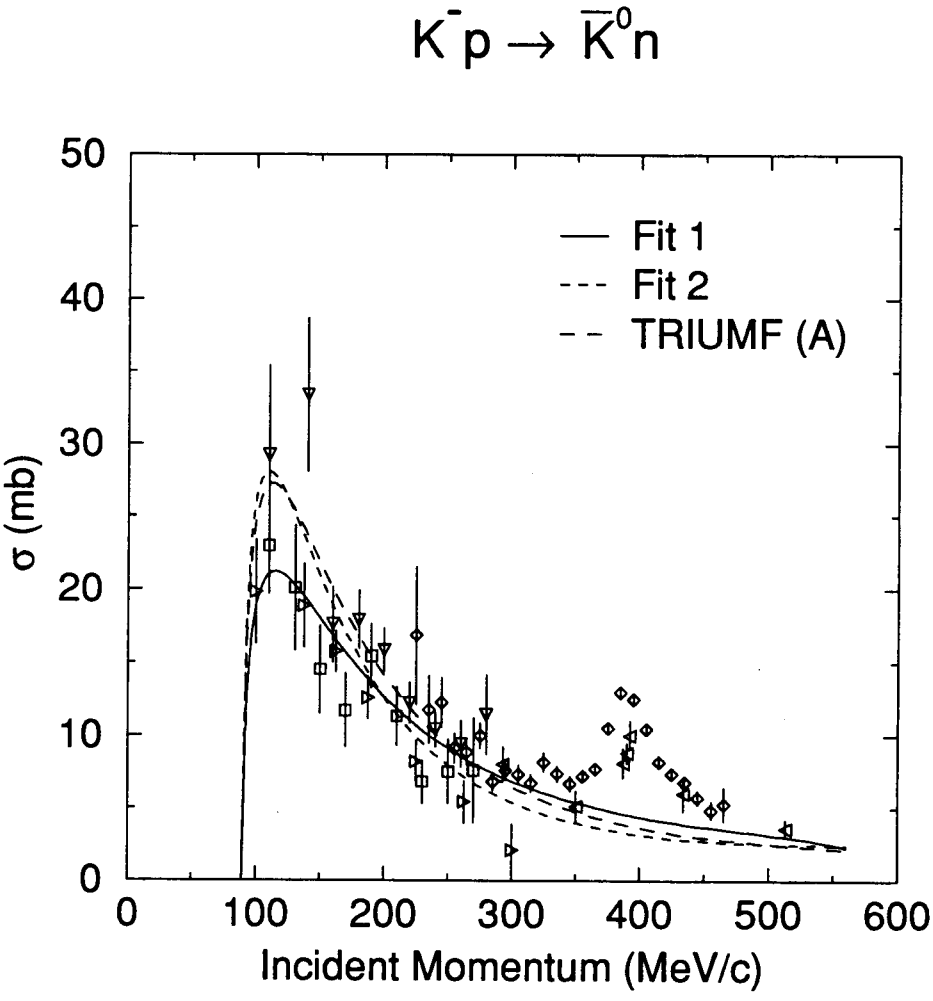

Figure 14. The $K^- p \rightarrow \bar{K}^0 n$ charge exchange cross sections calculated by the CBM with the parameter sets from the low energy fits.

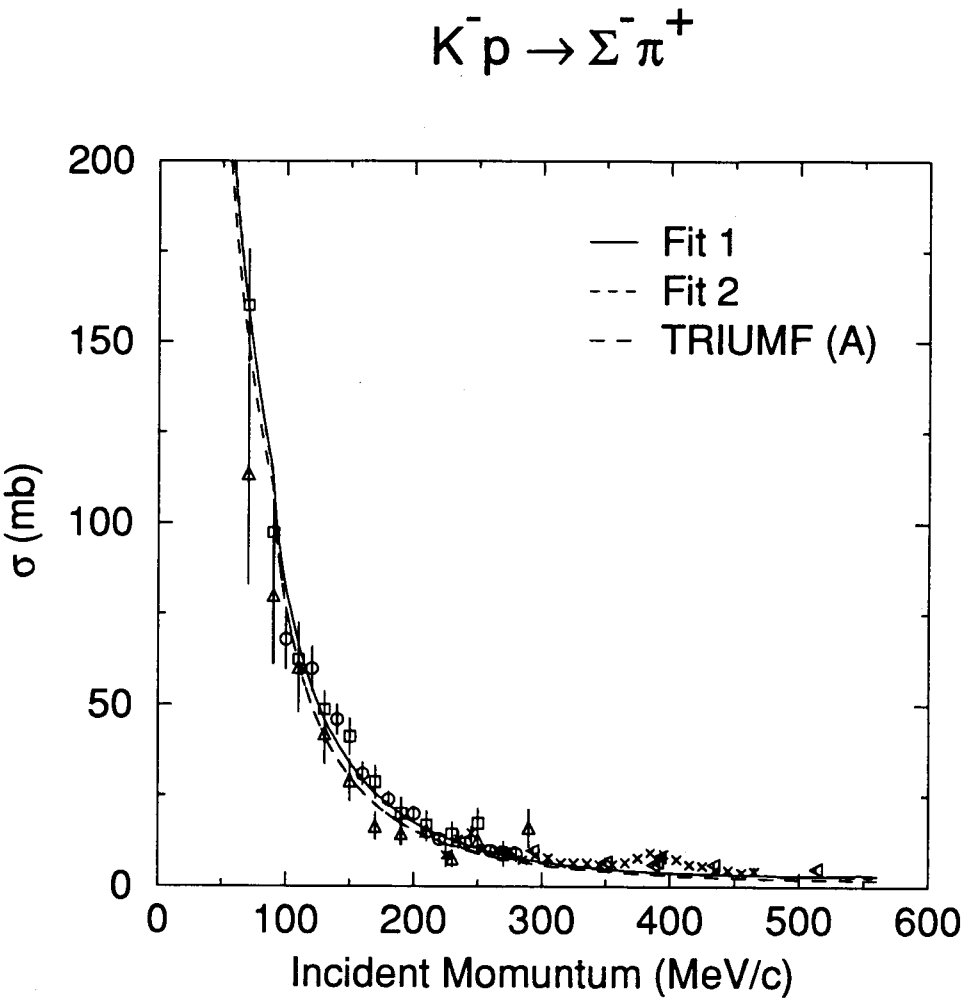

Figure 15. The $K^- p \rightarrow \pi^+ \Sigma^-$ reaction cross sections calculated by the CBM with the parameter sets from the low energy fits.

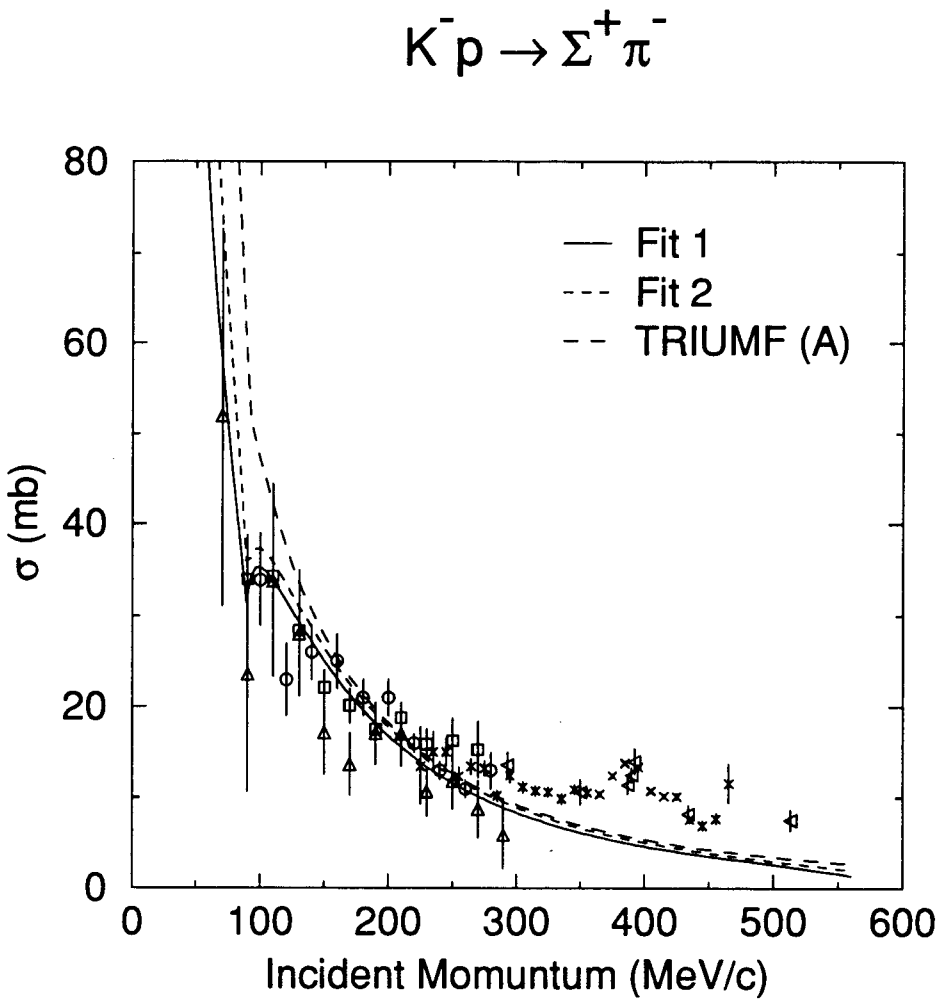

Figure 16. The $K^- p \rightarrow \pi^- \Sigma^+$ reaction cross sections calculated by the CBM with the parameter sets from the low energy fits.

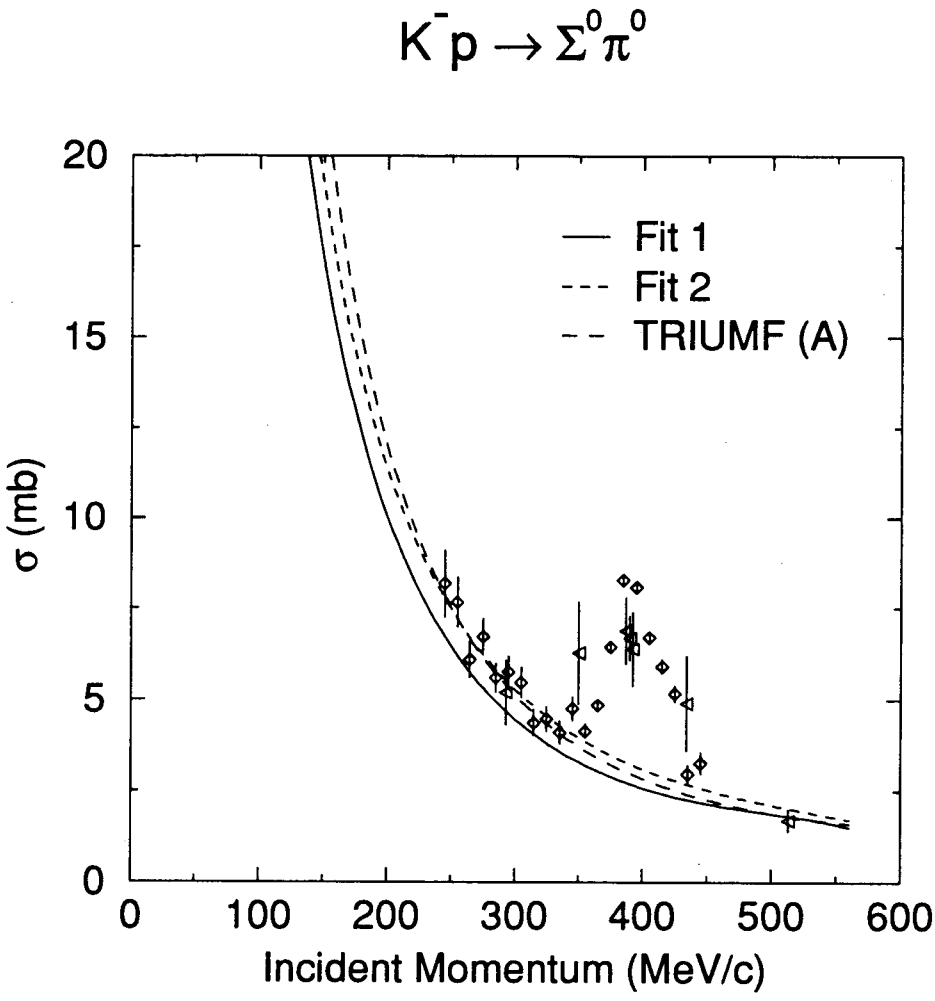

Figure 17. The $K^- p \rightarrow \pi^0 \Sigma^0$ reaction cross sections calculated by the CBM with the parameter sets from the low energy fits.

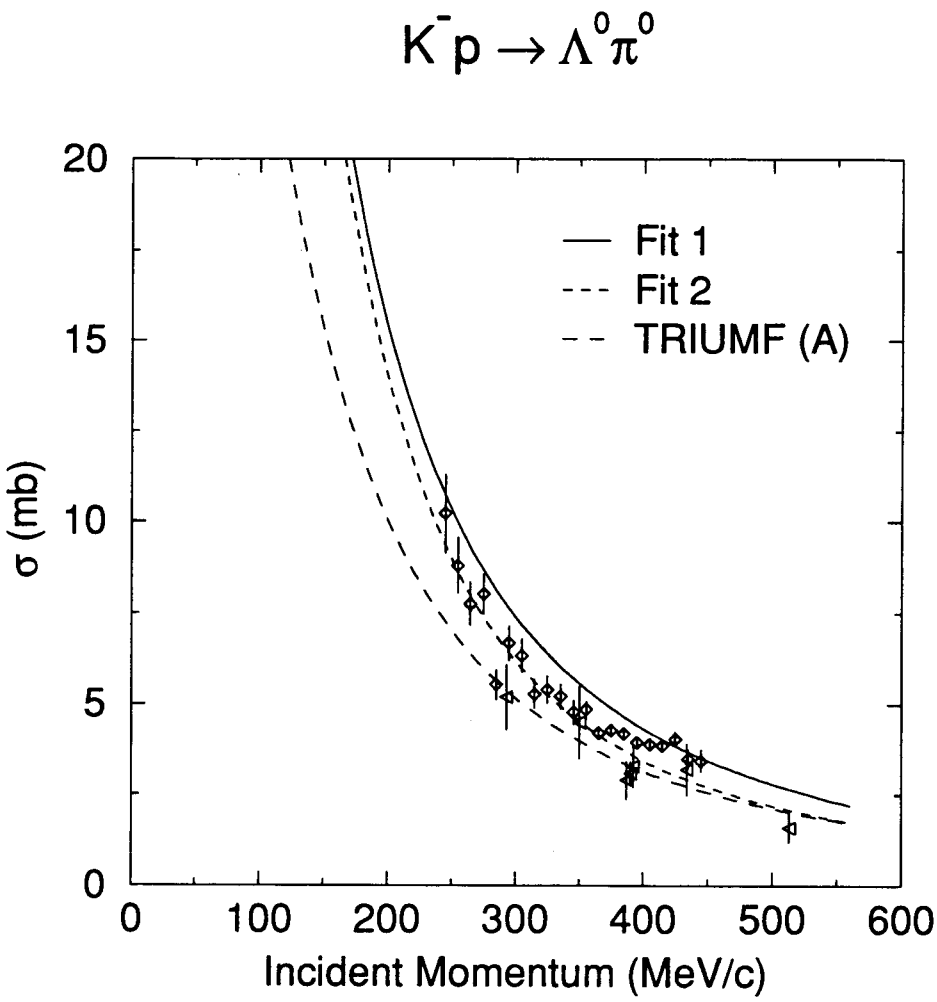

Figure 18. The $K^- p \rightarrow \pi^0 \Lambda$ reaction cross sections calculated by the CBM with the parameter sets from the low energy fits.

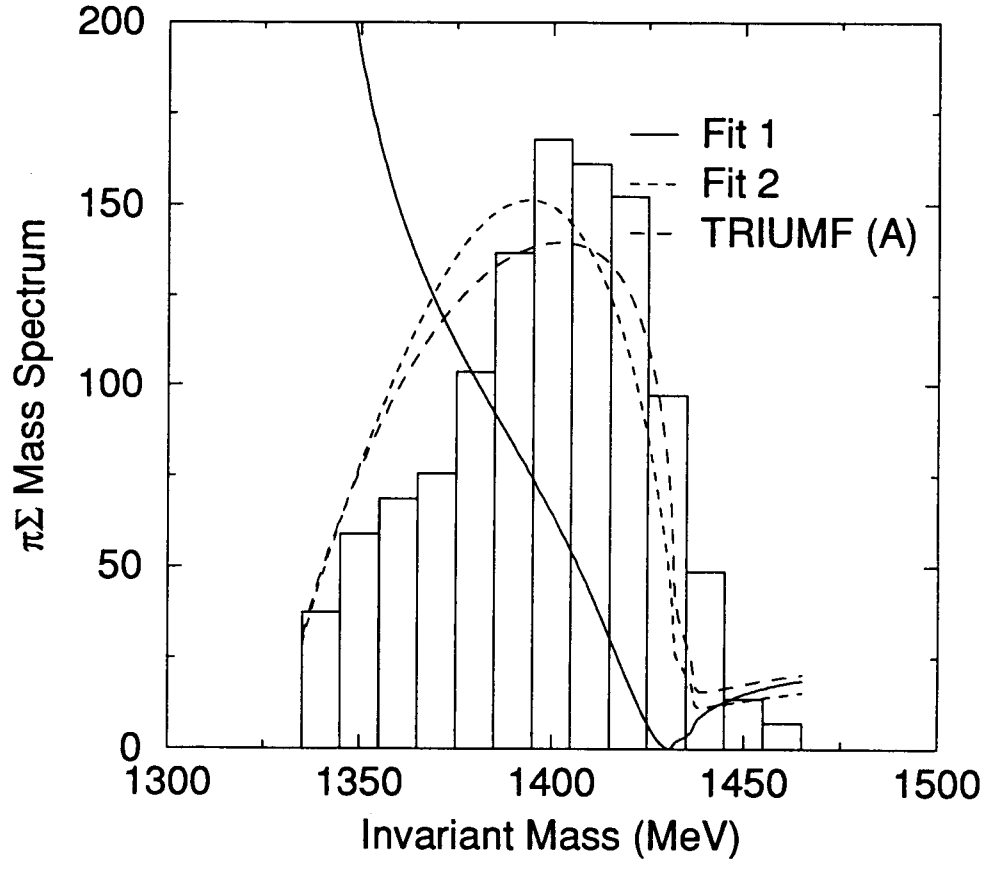

Figure 19. The $\pi\Sigma$ mass spectrum calculated by the CBM with parameter sets from the low energy fits. The histogram is Hemingway's data.

	γ	R_c	R_n
TRIUMF (A)	1.04	0.649	0.157
Fit 1	2.08	0.629	0.336
Fit 2	1.66	0.623	0.284
Fit 3	1.48	0.650	0.169
Fit 4	1.00	0.654	0.123

Table 10. The K^-p threshold branching ratios calculated by the CBM with different parameter sets.

Model. These are basically the same data used by the TRIUMF group[35]. The parameters of this fit, however, are different from the ones listed in the reference. This is no surprise because the numerical fitting procedures are not the same. And the experiment data used in two fits are not necessarily the same either. The parameters from this fit are listed in Table 11. The theoretical calculation of the different scattering cross sections and mass spectra are shown in Figures 13-19, and the branching ratios are listed in Table 10.

4.5.3 Fit 3

The major extension of this thesis beyond the TRIUMF's CBM is the P- and D-wave interactions. With the S-, P-, and D-wave interactions, it is possible for us to include the scattering cross sections with higher incident momentum and the $\Sigma(1385)$ resonance data. In this fit we include all of the four data groups (scattering cross sections, branching ratios, $\pi\Sigma$ mass

spectrum, and $\pi\Lambda$ mass spectrum) and run a straight χ^2 fit. The parameters are listed in Table 11, the theoretical curves are shown in Figures 20-27, and the branching ratios from this set of parameter are listed Table 10.

4.5.4 Fit 4

As we mentioned at the beginning of this chapter, due to the large difference of the number of data points in different data group, it is often to see one type of data overwhelmed by others if we simply do the standard χ^2 fit. To give a fair chance to all the data, we designed a fit with manually adjustable weighted χ^2_v (4.31). After adjusting the weight manually and examining dozens of fitting results, we picked the one we thought to be the best representing all the experimental constraints. The weight factors are

$$\begin{aligned} w_{scattering} &= 6 \\ w_{\pi\Sigma} &= 1 \\ w_{branchingratio} &= \infty \\ w_{\pi\Lambda} &= 6 \end{aligned}$$

We do not include the branching ratio data. This model does not produce reasonable branching ratio value for the reason we mentioned previously.

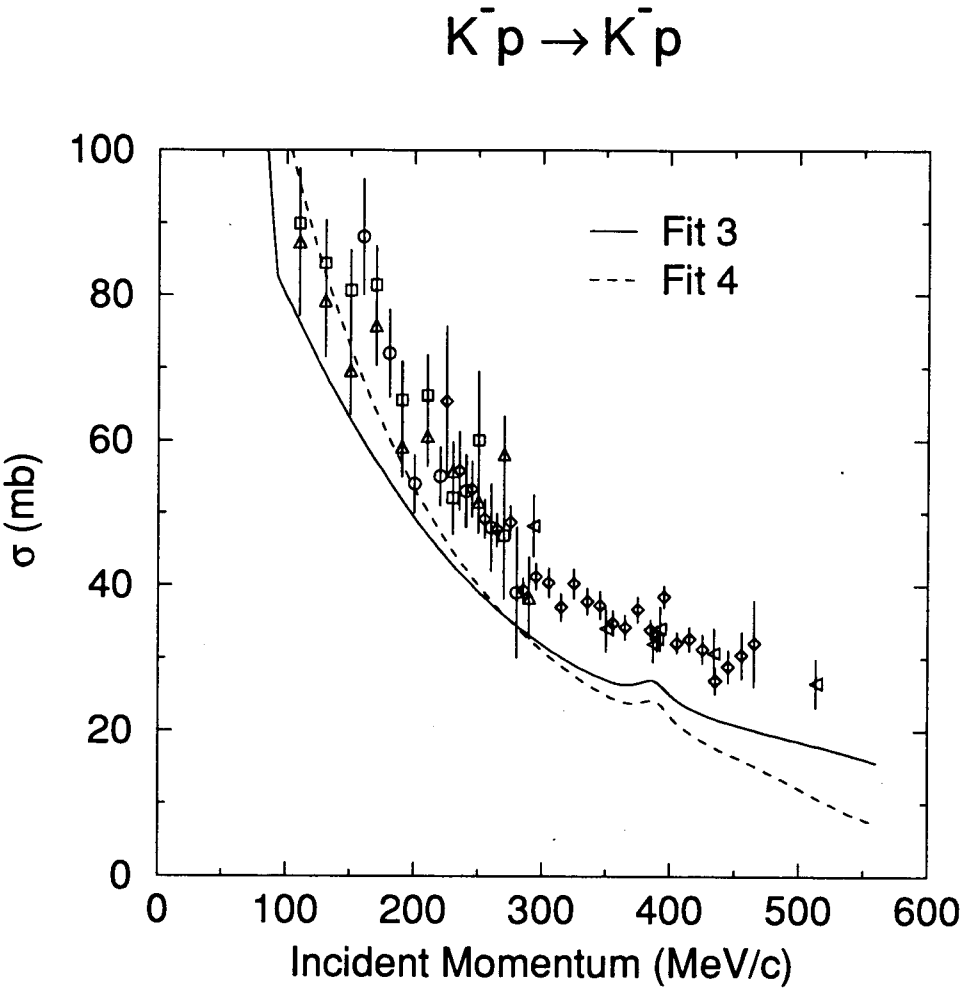

Figure 20. The $K^- p \rightarrow K^- p$ elastic scattering cross sections calculated by the CBM with the parameter sets from fitting all of the data.

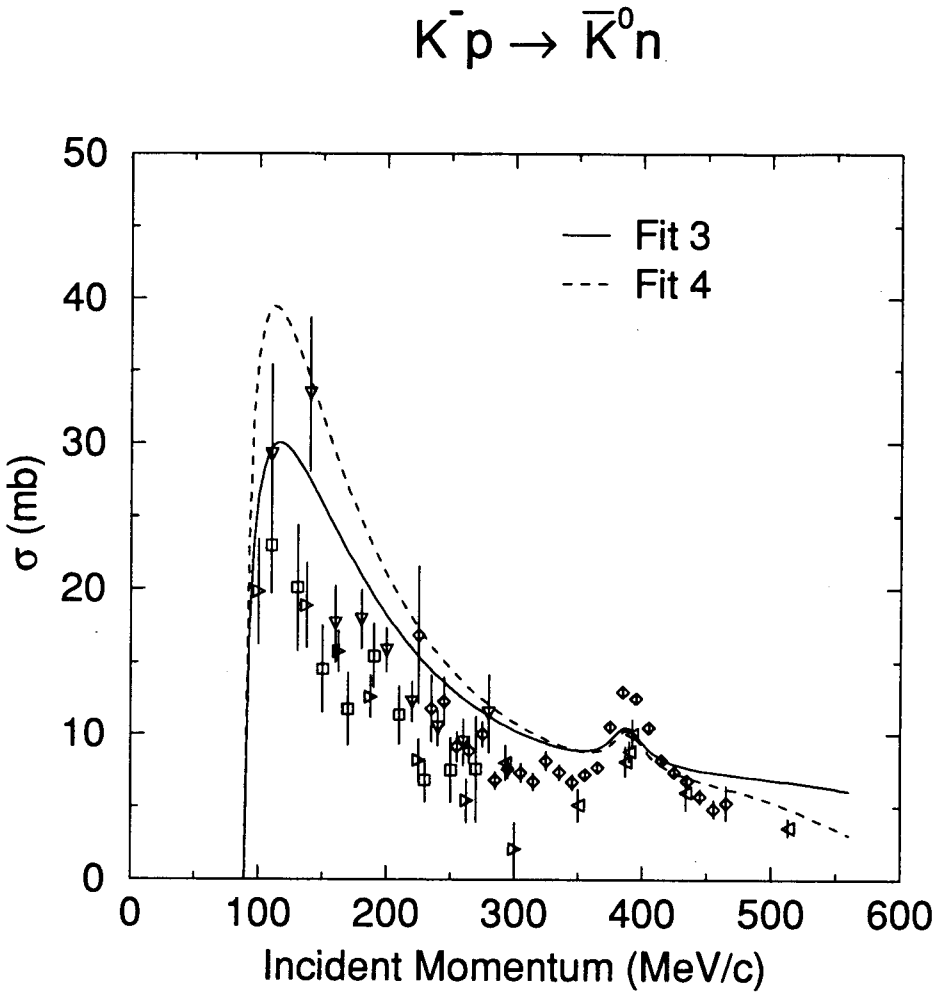

Figure 21. The $K^- p \rightarrow \bar{K}^0 n$ charge exchange cross sections calculated by the CBM with the parameter sets from fitting all of the data.

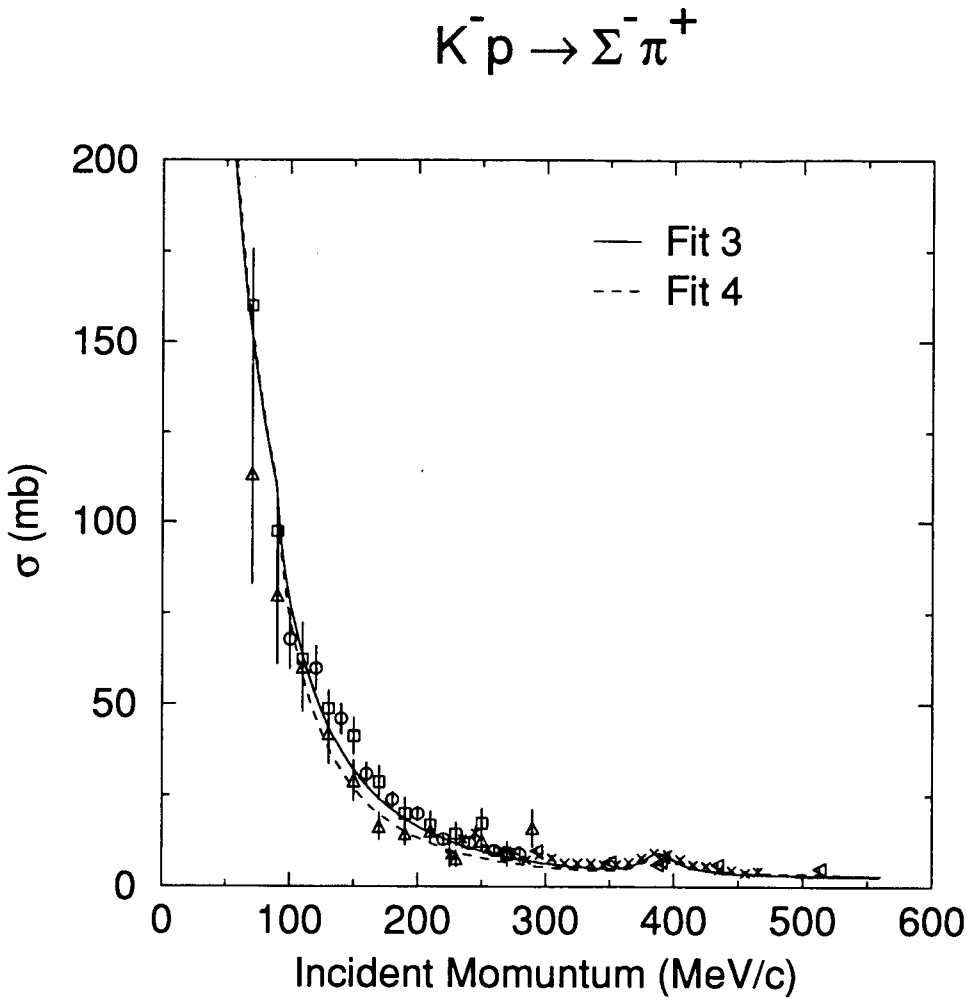

Figure 22. The $K^- p \rightarrow \pi^+ \Sigma^-$ reaction cross sections calculated by the CBM with the parameter sets from fitting all of the data.

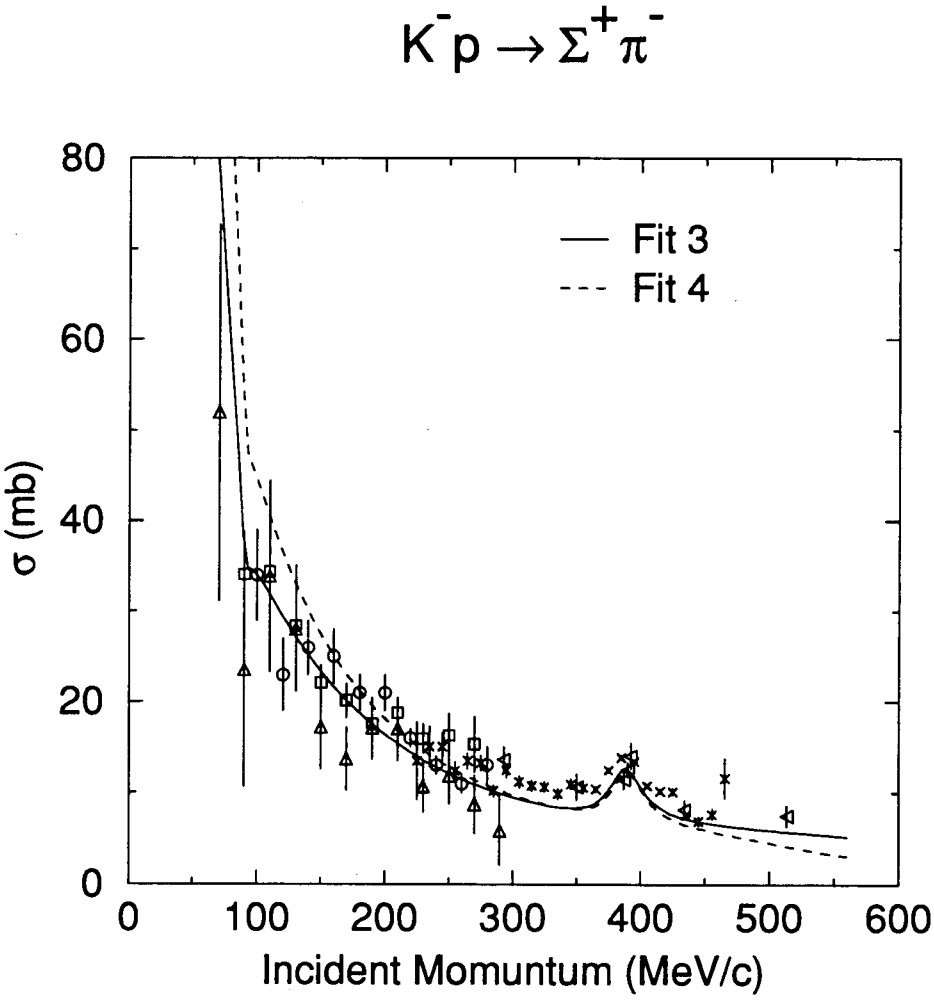

Figure 23. The $K^-p \rightarrow \pi^-\Sigma^+$ reaction cross sections calculated by the CBM with the parameter sets from fitting all of the data.

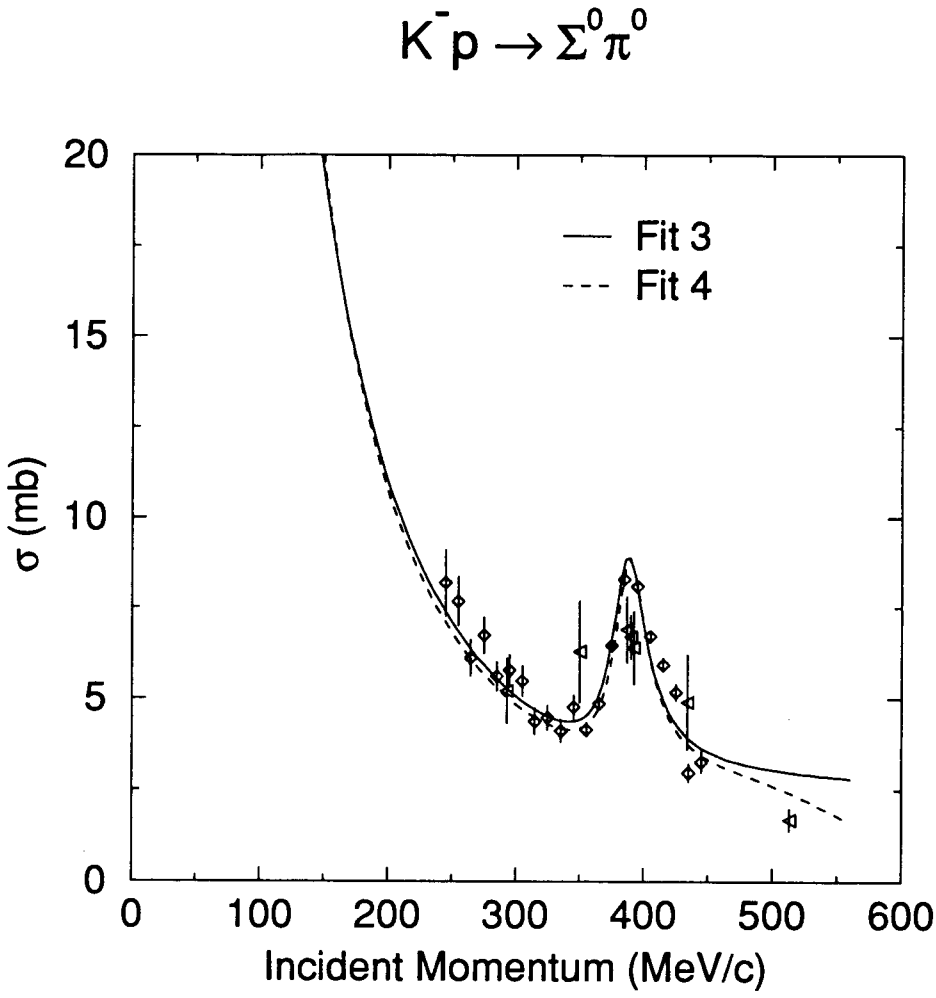

Figure 24. The $K^- p \rightarrow \pi^0 \Sigma^0$ reaction cross sections calculated by the CBM with the parameter sets from fitting all of the data.

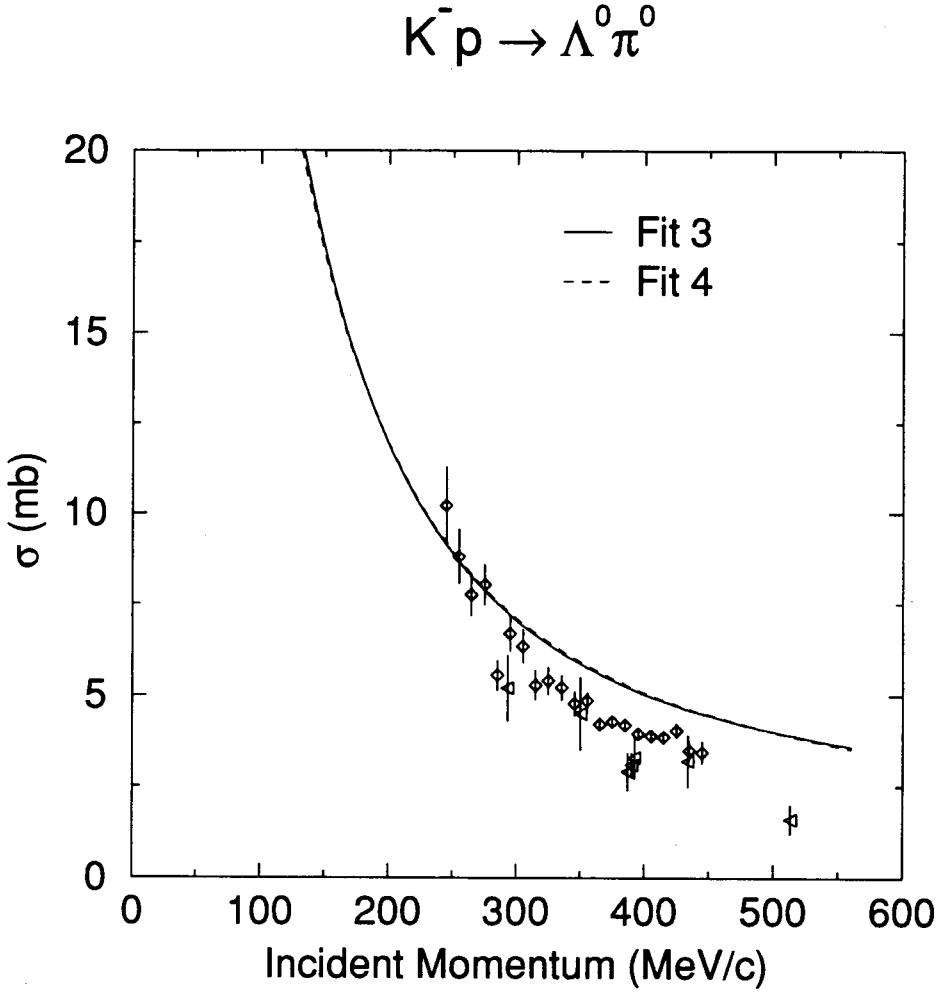

Figure 25. The $K^- p \rightarrow \pi^0 \Lambda$ reaction cross sections calculated by the CBM with the parameter sets from fitting all of the data.

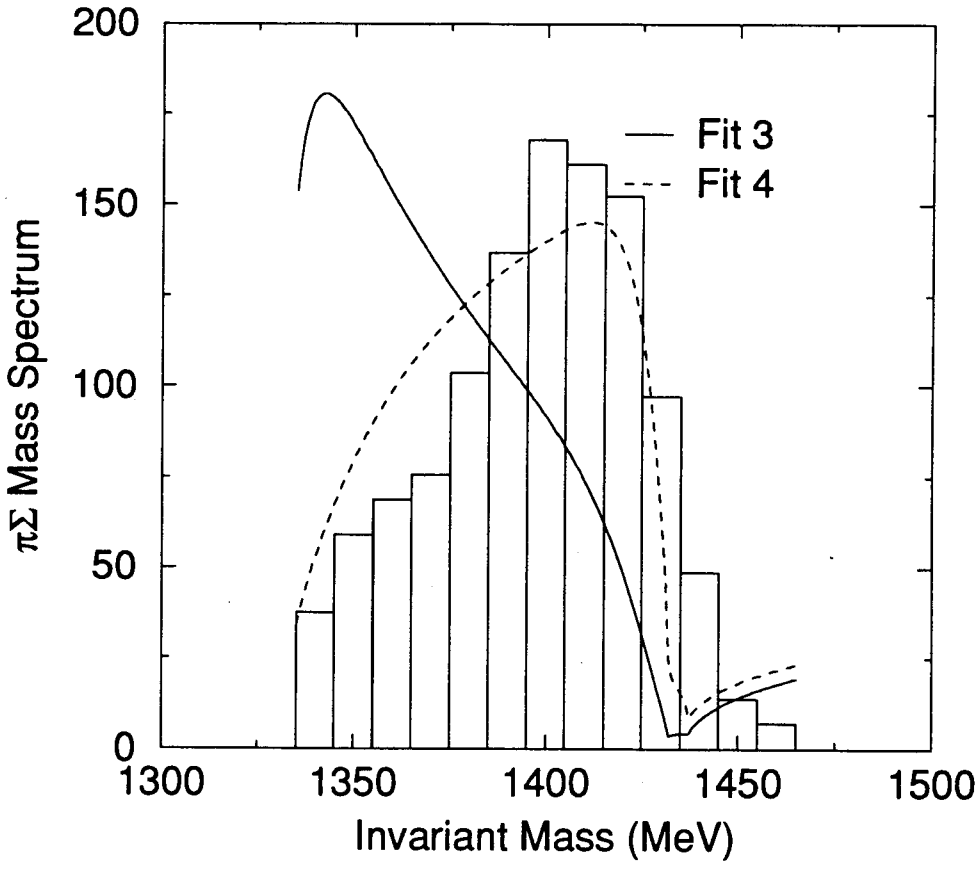

Figure 26. The $\pi\Sigma$ mass spectrum calculated by the CBM with parameter sets from fitting all of the data.

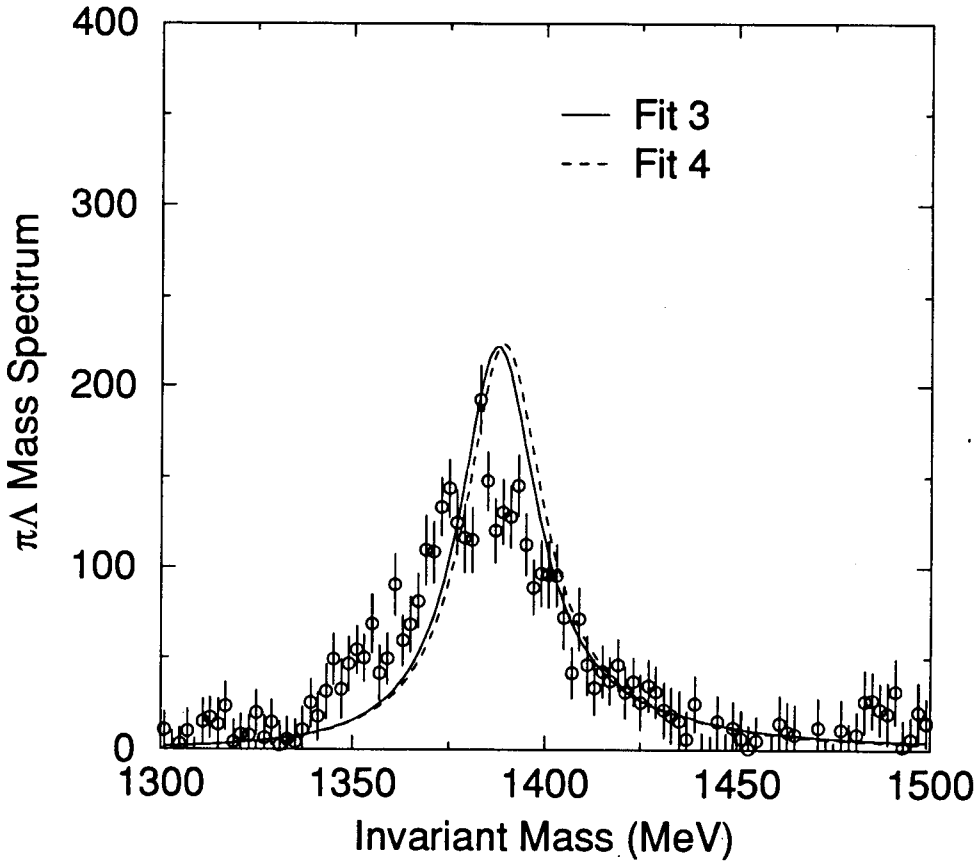

Figure 27. The $\pi\Lambda$ mass spectrum calculated by the CBM with the parameters from fitting all of data. The "data" points shown in the plot is Aguilar-Benitez's data after background subtraction.

	R	M_s^*	M_p^*	M_d^*	$f^{I=0}$	$f_K^{I=1}$	$f_\pi^{I=1}$
TRIUMF (A)	1.00	1630	N/A	N/A	120	100	110
Fit 1	1.29	1554	N/A	N/A	87	80	75
Fit 2	0.95	1588	N/A	N/A	126	82	146
Fit 3	1.23	1577	1421	1558	96	100	79
Fit 4	1.32	1542	1417	1546	103	96	78

Table 11. Final parameters of different fits. The radius R is in fm. Others parameters are in MeV.

Chapter 5

Applications of the Cloudy Bag Model

5.1 The T-matrix Elements on the Complex Energy Plane

In Chapter 4, we have shown the numerical methods used for solving the coupled-channel Lippmann-Schwinger Equation (3.29) for T-matrix elements. We study the detail of CBM T-matrix behavior in this section. The $I = 0$, S-wave $\bar{K}N$ T-matrix elements of 4 different fits are plotted in Fig. 28 and Fig. 29.

Fit 1 fits only low energy $K^- p$ scattering cross sections. It does not match the $\pi\Sigma$ mass spectrum at all. We do not expect it having any resonance structure in the $I = 0$, S-wave channels. The real part of its T-matrix element changes sign once at near above the $\pi\Sigma$ threshold and once at near below the $\bar{K}N$ threshold. The imaginary part shows a sharp peak near the $\pi\Sigma$ threshold and a big 'shoulder'. The big 'shoulder' peaks slightly at some place between 1400 MeV and the $\bar{K}N$ threshold. It does not show any sign of having a resonance at 1405 MeV. However, from Fig. 30, the 3D plot of the

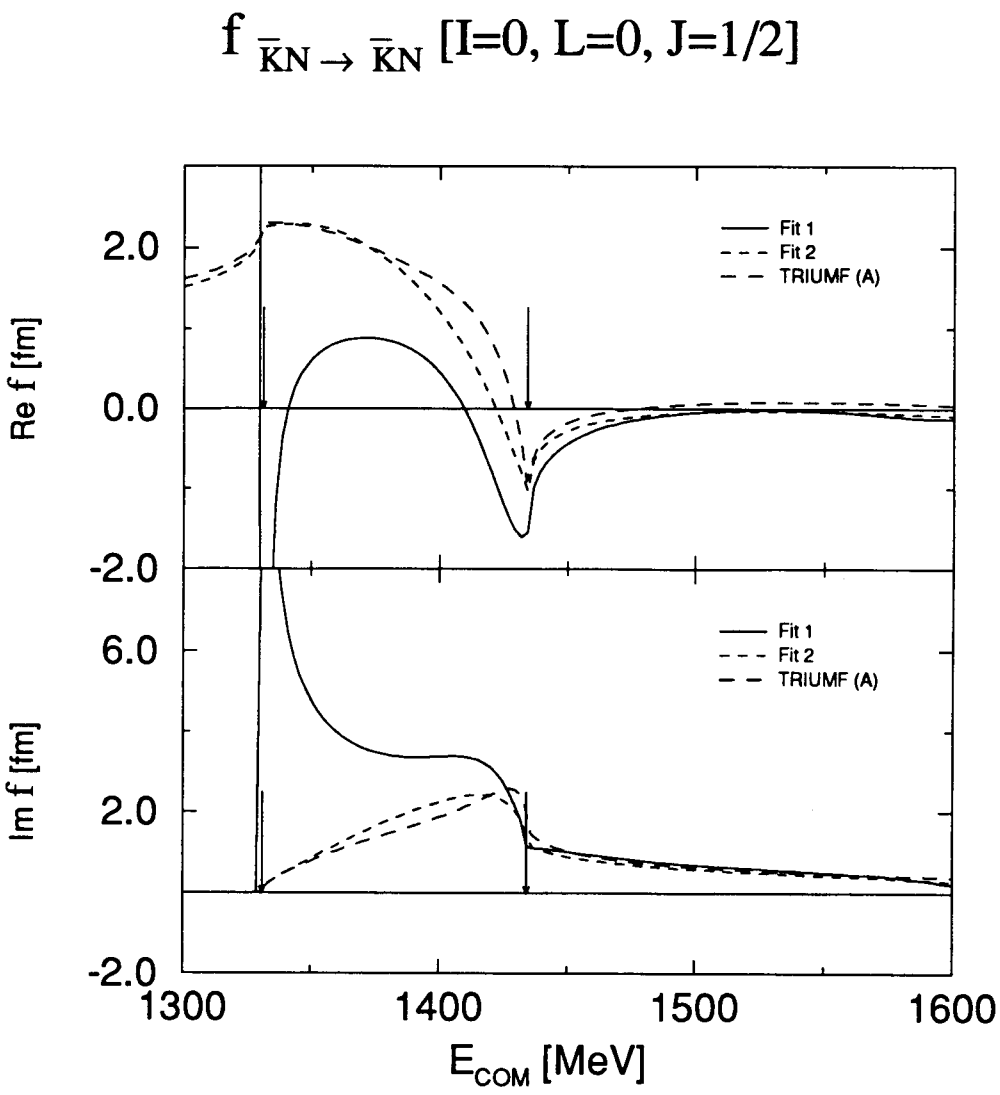

Figure 28. The $\bar{K}N$ S_{01} T-matrix elements of low energy fits. The TRIUMF's T-matrix elements are shown for comparison. The arrows show the $\pi\Sigma$ and $\bar{K}N$ thresholds.

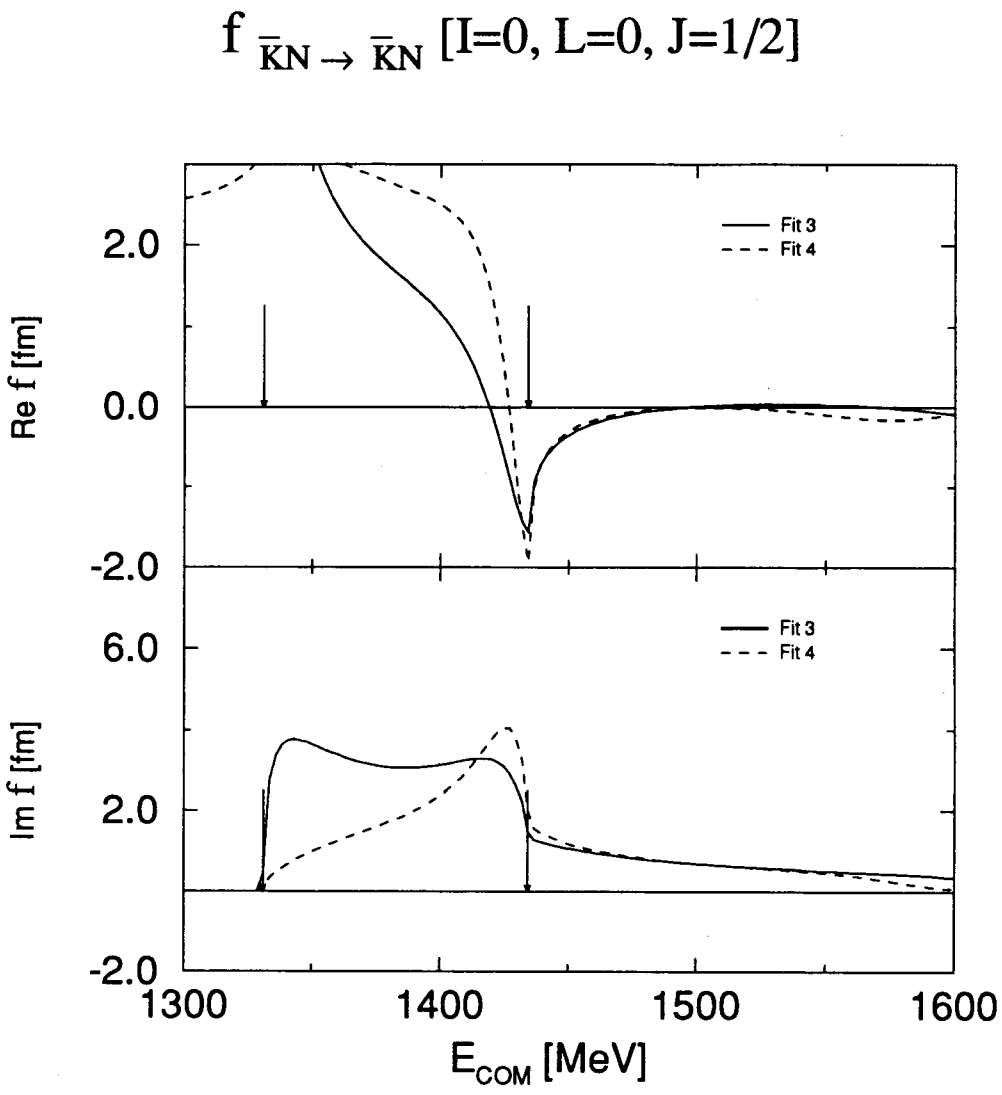

Figure 29. The $\bar{K}N$ S_{01} T-matrix elements of full fits. The TRIUMF's T-matrix elements are shown for comparison. The arrows show the $\pi\Sigma$ and $\bar{K}N$ thresholds.

T-matrix elements on the complex plane, it shows that there are two poles of the T-matrix elements. One is very close to the $\pi\Sigma$ threshold and the other is very near $\bar{K}N$ threshold (the search routine shows that the position is above the threshold). The first pole causes the rapid change of the T-matrix elements near $\pi\Sigma$ threshold. But the second pole is too far away from the real energy axis and too weak to cause a big peak on the real energy axis. It, however, causes the sign change of the real part T-matrix elements below $\bar{K}N$ threshold.

Fit 2 fits low energy scattering and the $\pi\Sigma$ mass spectrum. Just as we mentioned in Chapter 4, it behaves very much like TRIUMF's fit. The real part changes sign below $\bar{K}N$ threshold and the imaginary part peaks (with an asymmetric shape) at the same position. The 3D plot (Fig. 31) shows that it also has a pole above $\bar{K}N$ threshold.

Fit 3 fits all the data. But due to the large number of scattering and $\pi\Lambda$ data points, the constraint of $\pi\Sigma$ mass spectrum is not very significant. Actually, the fit does not give a good mass spectrum shape, as we saw in Chapter 4. The real part of the T-matrix elements also changes sign below $\bar{K}N$ threshold. But, the imaginary part shows two broad, asymmetric peaks, one below $\bar{K}N$ threshold and the other above the $\pi\Sigma$ threshold. The 3D plot (Fig. 32) shows that there are two poles on the complex energy plane. One near $\bar{K}N$ threshold and the other near $\pi\Sigma$ threshold. Both of them are very close to the real energy axis.

Fit 4 is our "best" fit of the new CBM. It gives good scattering cross sections, good $\pi\Sigma$ mass spectrum, and good $\pi\Lambda$ mass spectrum. The shape of the T-matrix curves on the real energy axis are very similar to the one of

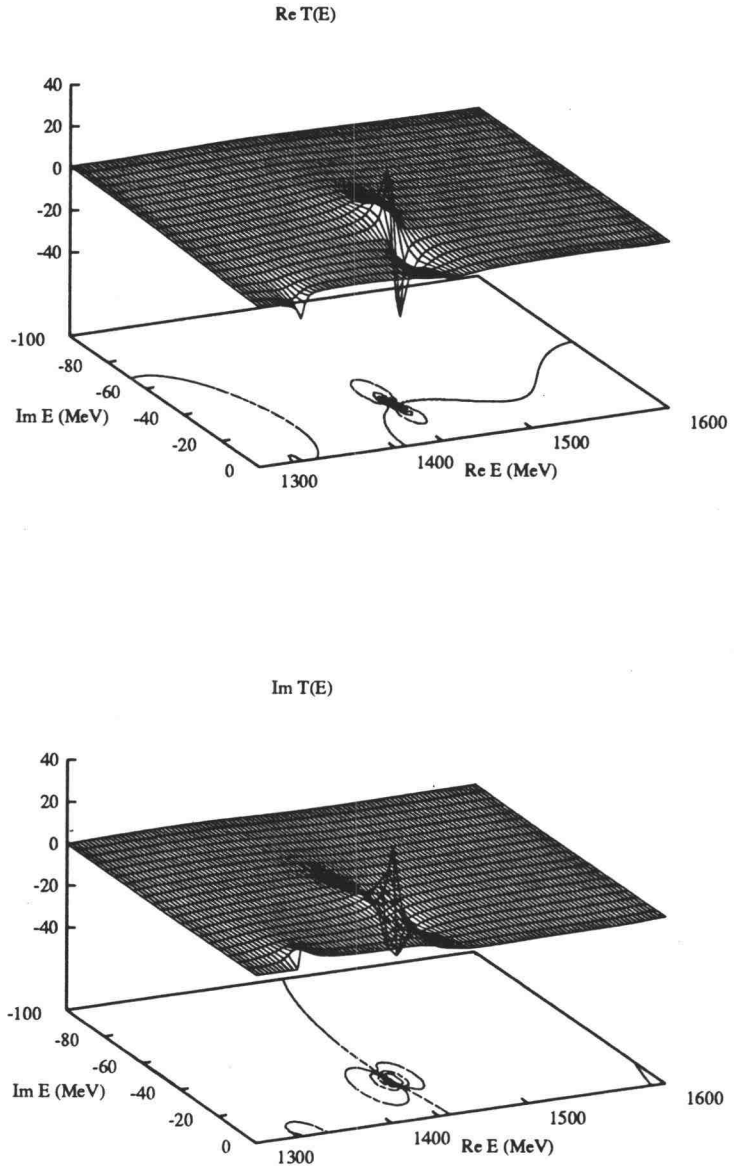

Figure 30. The $\bar{K}N$ S_{01} T-matrix elements of fit 1 on complex energy plane.

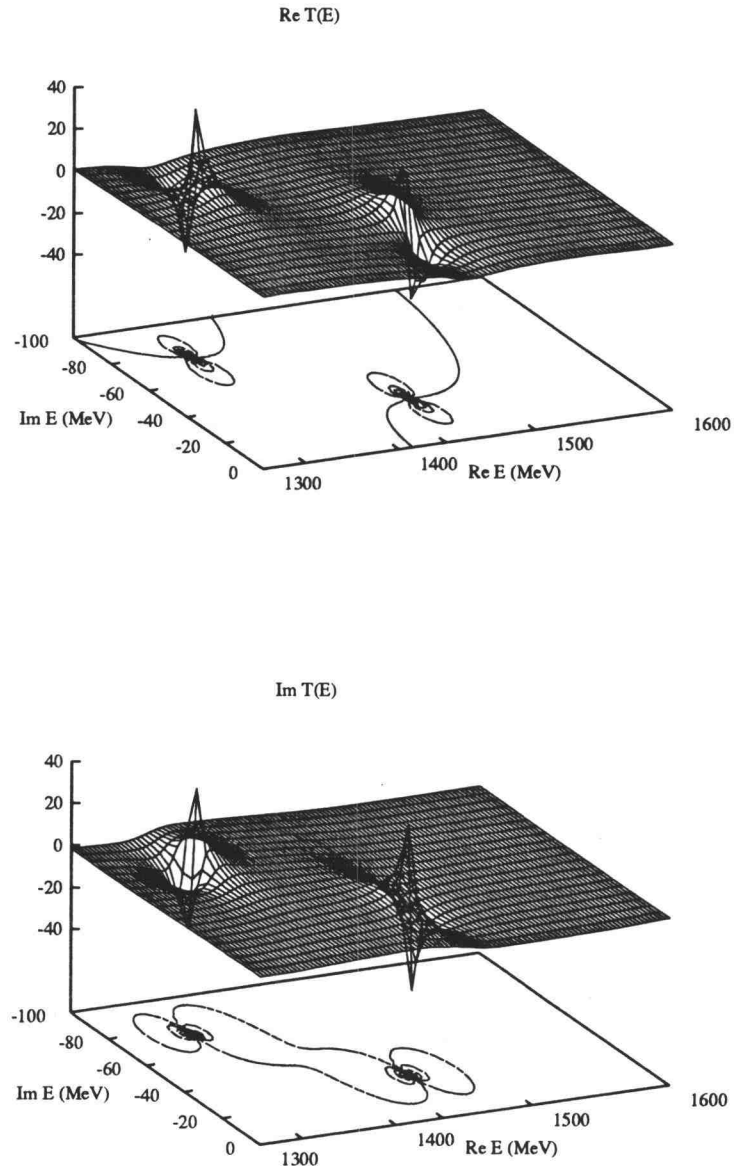

Figure 31. The $\bar{K}N$ S_{01} T-matrix elements of fit 2 on complex energy plane.

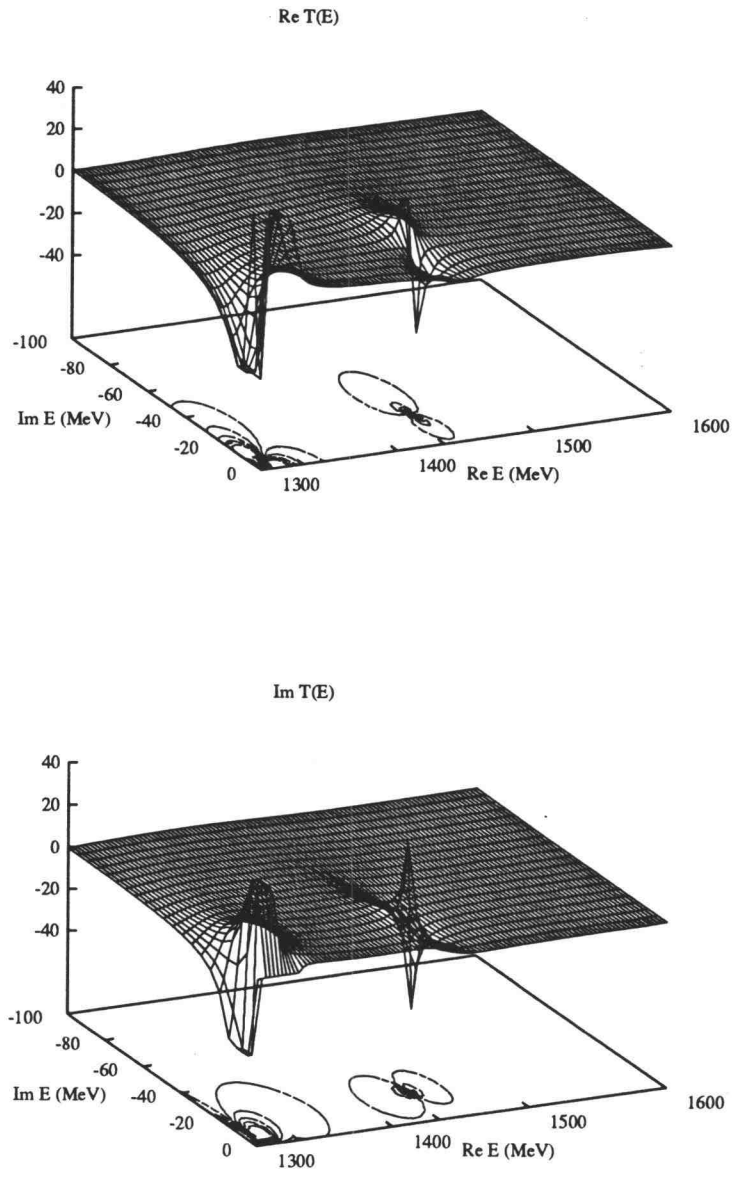

Figure 32. The $\bar{K}N$ S_{01} T-matrix elements of fit 3 on complex energy plane.

fit 2 and the one of TRIUMF's. The magnitude are about 30% larger. But since we only calculate the shape of $\pi\Sigma$ mass spectrum, not the magnitude, this fit is also very good on the $\pi\Sigma$ mass spectrum.

There are other resonances in the coupled $\bar{K}N$, $\pi\Sigma$, and $\pi\Lambda$ system. The $\Sigma(1385)$ is in the channel $I = 1$, $L = 1$, $J = 3/2$ and the $\Lambda(1520)$ is in the channel $I = 0$, $L = 2$, $J = 3/2$. The plots of T-matrix elements of these channels (Fig. 34 and Fig. 35) show clearly the resonance shape at the energies we expected.

5.2 The Pole Positions in the CBM

In the energy range from 1300 to 1550 MeV, the $\bar{K}N$ system couples to several resonances, including $\Lambda(1405)$ in S, $\Sigma(1385)$ in $P_{3/2}$, and $\Lambda(1520)$ in $D_{3/2}$. In this thesis, we extended the original $\bar{K}N$ CBM interaction from S-wave to P- and D-wave. In this section, we apply the extended Cloudy Bag Model to explore the classic question of the relation between the properties of a resonance and the poles of the corresponding T-matrix[75, 76]. Experimentally, physics is conducted along the real energy axis, and it is there that a resonance produces a characteristic signature in T. Conventionally, (for theory), physical values of energy are those obtained by approaching the real axis of the first (physical) energy sheet from above, with bound state and resonance poles appearing as poles of T off the positive energy axis[75, 76]. Convention and experiment concur that a pole in T on the second (unphysical) energy sheet near the real positive axis produces a narrow resonance along the positive real axis. And from a theoretical point of view, one of

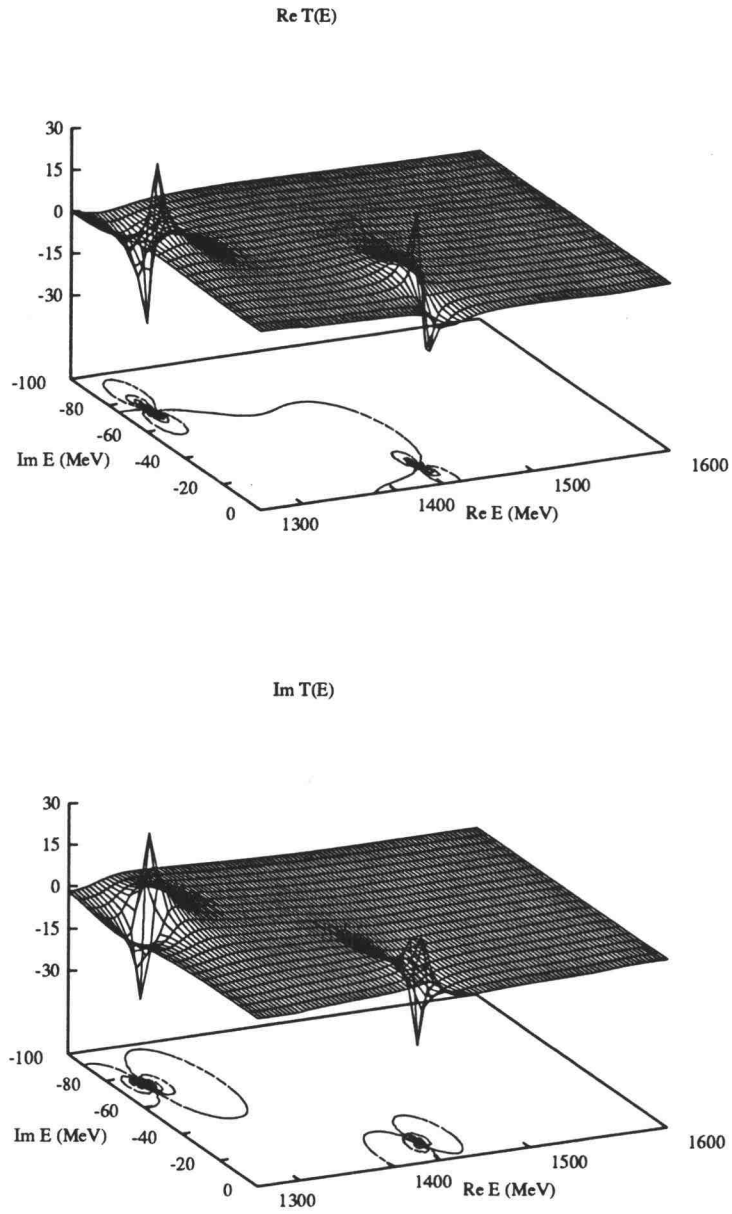

Figure 33. The $\bar{K}N$ S_{01} T-matrix elements of fit 4 on complex energy plane.

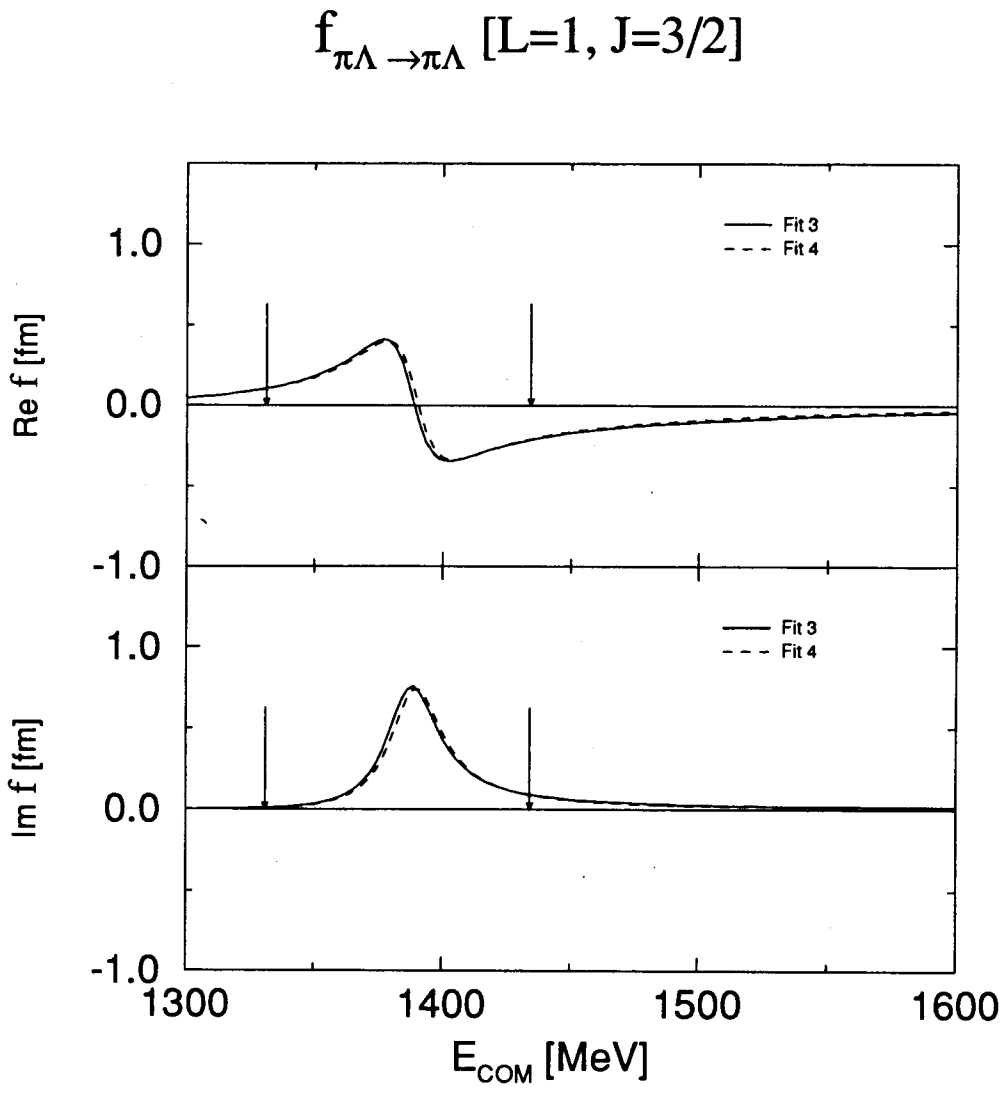

Figure 34. The P_{13} $\pi\Lambda$ T-matrix elements of fit 4.

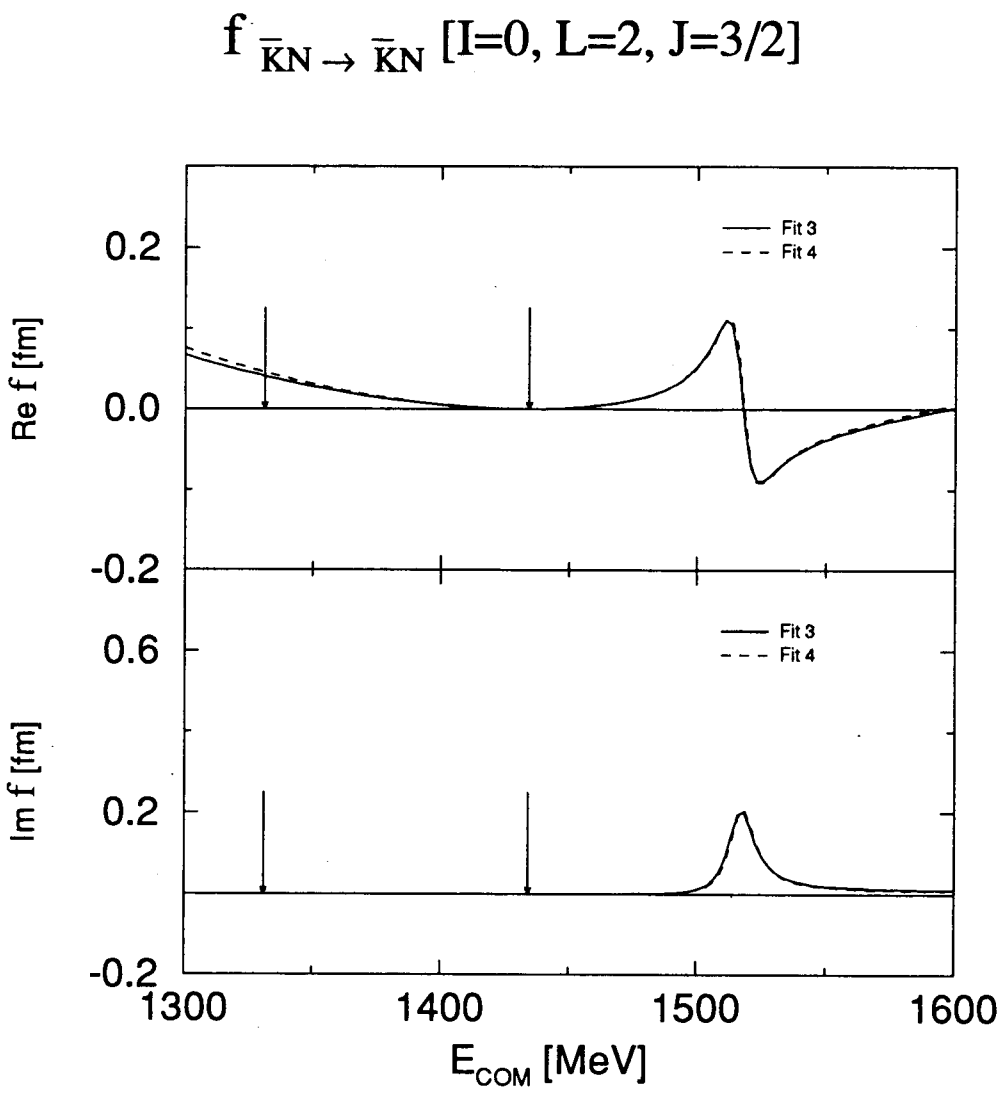

Figure 35. The D_{03} $\bar{K}N$ T-matrix elements of fit 4.

the best ways to characterize a model of $\bar{K}N$ scattering is by knowing the singularities, poles, and branch cuts of T in the complex energy plane. As a matter of convention[75, 76], we consider poles of T to be either resonant poles (on the second energy sheet) or bound state poles (on the first energy sheet)—even if they are not near the real energy axis. The conditions for which a pole on the second energy sheet may actually cause a resonance depend on a number of factors, such as the existence and proximity of other poles, different channel openings, etc. Nevertheless, we search for poles even far from the real energy axis in an effort to understand better the sometimes puzzling behavior of T along the real axis.

In Chapter 3, we already studied the numerical methods for searching the pole positions. In this case, it is nuclear interactions only (the CBM interactions). The pole positions are determined by

$$\det(1 - VG) = 0 \tag{5.1}$$

with V being the CBM potential.

5.2.1 $S_{1/2}$ Resonances

In the $S_{1/2}$ channel, the $\bar{K}N$ system couples to the $\Lambda(1405)$ $I = 0$ resonance. The plots of T-matrix elements on the complex plane in last section clearly shows there are poles in this channel. However, there are two poles in this channel, the position of both poles are listed in Table 12. As a comparison, we list the resonance parameters deduced from real axis T-matrix behavior. Results from other models are also listed as a comparison.

Parameter set	(E_r, E_i) (MeV)
Fit 1	(+2, -27)
Fit 1	(-104, -0.6×10^{-4})
Fit 2	(+17, -31)
Fit 2	(-80, -76)
Fit 3	(+5, -21)
Fit 3	(-129, -4)
Fit 4	(1.2, -13)
Fit 4	(-114, -74)
TRIUMF (A)	(+13, -12)
TRIUMF (A)	(-95, -76)
r1[77]	(-58, -32)
nr1[77]	(-8, -14)
AHW[68]	(-14, -25)

Table 12. The S-wave resonance pole positions in complex energy plane. The numerical uncertainty is approximately ± 2 MeV.

Parameter set	(E_r, E_i) (MeV)
Fit 3	(-48, -12)
Fit 4	(-46, -12)

Table 13. The $P_{3/2}$ resonance pole positions in complex energy plane. The energy given in the table is relative to the $\bar{K}N$ threshold which is at 1435 MeV.

5.2.2 $P_{3/2}$ Resonance

The $\Sigma(1385)$ is a $P_{3/2}$ resonance. The positions of the pole is listed in Table 13. The published result of mass and width for $\Sigma^0(1385)$ is $(1383.7 \pm 1.0, 36 \pm 5)$ MeV[64].

5.2.3 $D_{3/2}$ Resonance

The $\Lambda(1520)$ is a $D_{3/2}$ resonance. The pole positions are listed in the Table 14. The published result of the resonance mass and width is $(1519.5 \pm 1.0, 15.6 \pm 1.0)$ MeV[64].

5.3 Kaonic Hydrogen

With its negative charge and heavy mass, the K^- can slip inside of the electron orbit in a ordinary hydrogen and form a "kaonic hydrogen" with the Coulomb interaction between the negative charged K^- and the positive charged proton. A hydrogen-like atom can be described semi-classically by

Parameter set	(E_r, E_i) (MeV)
Fit 3	(+81, -6)
Fit 4	(+83, -6)

Table 14. The $D_{3/2}$ resonance pole positions in complex energy plane. The energy is the relative to the $\bar{K}N$ threshold which is at 1435 MeV.

the Bohr model and its Bohr radius are

$$R_n = \frac{n^2}{me^2} \tag{5.2}$$

where m is the reduced mass and n is the principle quantum number of the state. The mass of the K^- (493.646 MeV) is about 1000 times the mass of the electron and the reduced mass of the kaonic hydrogen is about 650 times the reduced mass of the ordinary hydrogen. From Eq. (5.2), the Bohr radius of the kaonic hydrogen is about 650 times smaller than the hydrogen for the same principle quantum number. For the $1s$ level, the Bohr radius of the kaonic hydrogen is about 83 fm. At such a short range, the strong interaction causes a significant shift to the energy level from its value of the Bohr energy level. Also the coupling to other channels gives the energy level a significant width. However, the shift and width of the $2p$ level is negligible because the Bohr radius of the level is too large for the strong interaction to have a significant effect to this state. Therefore, the shift and width of the $1s$ level can be effectively measured by measuring the X-ray emitted from the kaonic hydrogen transition from $2p$ to $1s$ level.

Experimentally, antikaons from the beam are stopped in the liquid hy-

drogen and the X-ray lines from kaonic hydrogen atoms are identified. The results of the shift and width measured by three different groups[78, 79, 80] are shown in Fig. 36.

Theoretically, the Coulomb plus nuclear bound state problem is solved for different parameter sets. With the bound state energy (relative to $\bar{K}N$ threshold) as (E_R, E_I), the shift and width are defined as

$$\epsilon = -E_R - E_B \tag{5.3}$$

$$\Gamma = -2E_I \tag{5.4}$$

where E_B is the Bohr energy for the kaonic hydrogen with pure Coulomb interaction. The shift and width are plot in Fig 36 alone with experimental data.

We note that in all cases the calculated shift ϵ is toward the less bound (negative) while the experimental shifts are toward the more bound (positive).

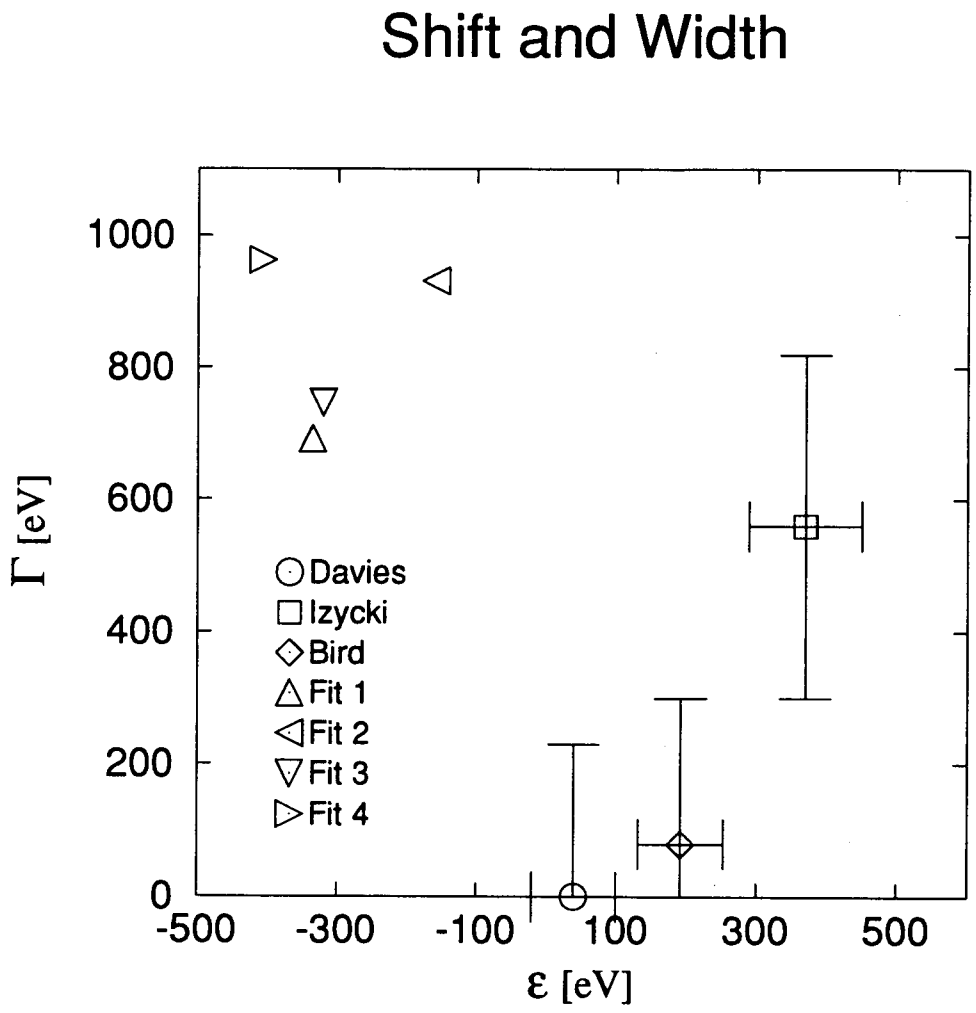

Figure 36. The experimental values and theoretical prediction of the CBM of the $1s$ kaonic hydrogen shifts and widths.

Chapter 6

Summary and Conclusions

6.1 Summary

We have extended the Cloudy quark Bag Model (CBM) from S- to S-D-waves for the coupled ($\bar{K}N$, $\pi\Sigma$, $\pi\Lambda$) system. The parameters of this extended CBM are determined by fitting to the K^-p scattering cross section (6 different channels of a total of 300 data points), the $\pi\Sigma$ mass spectrum from the $K^-p \to \Sigma\pi\pi\pi$ reaction (7 data points), the K^-p threshold branching ratio (3 data points), and the $\pi\Lambda$ mass spectrum from the $K^-p \to \Lambda\pi\pi\pi$ reaction (200 data points). Four sets of CBM parameters are obtained by fitting different combinations of data. The low-energy fits, 1 and 2, show a small χ^2 per degree of freedom (1.5 for fit 1 and 2.0 for fit 2). Actually, if we compare our fit 2 (Fig. 13 and Fig. 14) to Schnick's potential model[81], (Fig. 37) we can see they are equally good at momenta less than 250 MeV/c. This is because the error bars of the scattering data are very large at low energy. The data are derived from the photographic pictures of the particle trails of bubble chamber experiments, and at low momenta, the trails are very short,

order of millimeters, and are very hard to measure accurately. While tens of thousands of photographs are analyzed but only hundreds of events are used to determine the cross sections.

The overall quality of the fit differs when higher momentum scattering data are included. Fit 3, which include higher energy scattering data as well as all other data, shows a large χ^2 per degree of freedom. Mixing the low and higher momenta data together tends to make the higher momenta data dominate the fit. This is because at higher energy, the $\Lambda(1520)$ resonance data are very well determined, in fact the error bars look *tiny* compared to low energy ones. Other data ($\pi\Sigma$ mass spectrum, branching ratio) are overwhelmed by them as well. A weighted χ^2_v fit (4) is designed to give a more balanced fit by giving less emphasis to the $\Lambda(1520)$ data.

As described in the thesis, our model was not constructed to provide an accurate description of isospin-breaking effects. Therefore it is not surprising to see it fail to produce the K^-p threshold branching ratio. In fact, in fit 4, which we considered to be our best fit, was not fit to branching ratio data at all. And yet even when the branching ratio data are included in the fit 3, it does not have much influence on the fit due to the large number and small error of scattering data. From our experience with a weighted χ^2_v fit, the fit to the scattering data turns out bad if we try to increase the importance of the branching ratio.

We have used the extended CBM to study resonances to which the $\bar{K}N$ system couple, specifically, the $\Lambda(1405)$, $\Sigma(1385)$ and $\Lambda(1520)$. In fit 4's description of the $\Lambda(1405)$, the scattering amplitudes show an asymmetric peak in the imaginary part and a sign change in the real part between 1400

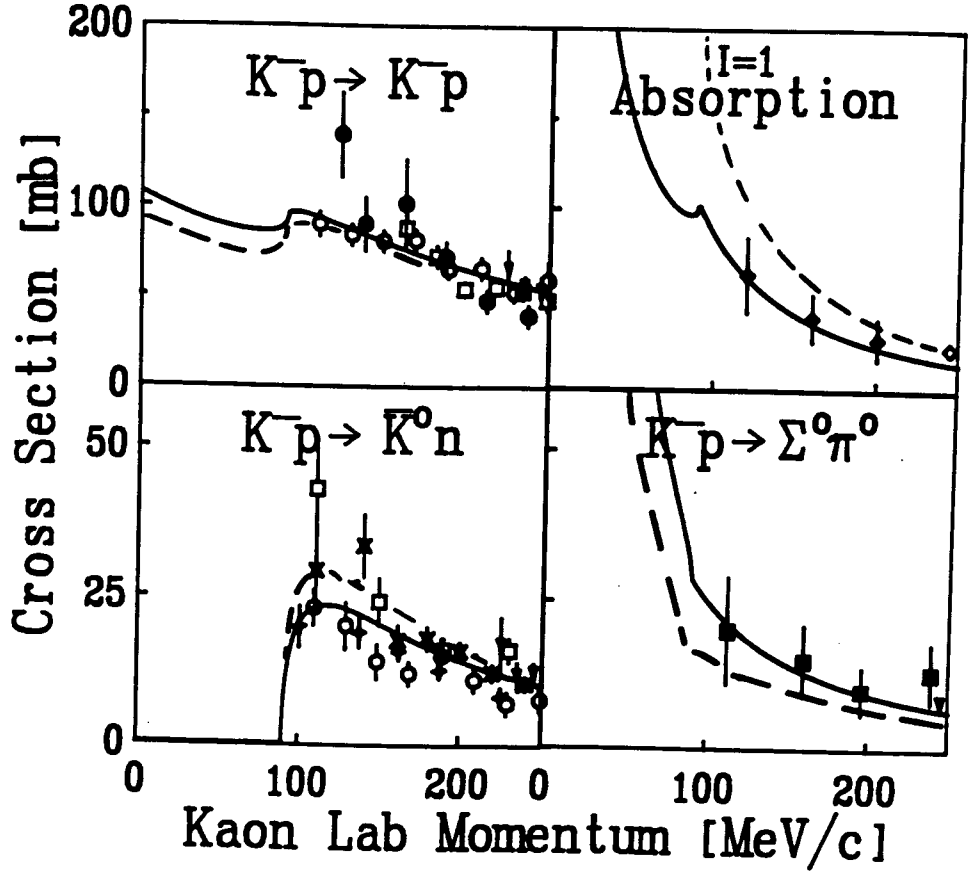

Figure 37. Scattering cross sections of Schnick's potential model.

MeV and the $\bar{K}N$ threshold 1435 MeV. However, the position of the pole in the complex energy plane found by the search routine is above the $\bar{K}N$ threshold. The asymmetry peak and sign change are a consequence of the interference between the pole and the threshold itself. This is a unique feature of the coupled-channel system.

For the other two resonances, $\Sigma(1395)$ and $\Lambda(1520)$, the scattering amplitudes show standard resonance shape. The poles in these cases are at the locations consistent with the energies deduced from the study of the T-matrices.

The kaonic hydrogen shift and width calculation are consistent with those found by others. While all the experiment shows the shift towards more bound, $\epsilon > 0$, all conventional theoretical calculations show shift towards the less bound, $\epsilon < 0$. The accepted view now is that experiment might well be in error.

6.2 Future Directions

To obtain better understanding of the low energy $\bar{K}N$ system, more high quality data are needed. Perhaps the commissioning of the KAON accelerator will provide more experimental results in near future. Also, a definitive X-ray experiment of kaonic hydrogen transition would go a long way in supporting or ruling out the CBM prediction. On the other hand, it is important to investigate how to incorporate isospin symmetry breaking effect in to the CBM. It may be the last piece of the puzzle of the branching ratio and the kaonic hydrogen.

Another direction is to apply this extended CBM in the nuclear environment, that is, to study the $K^- - A$ system. Since the nuclear environment test the off-energy shell (small r) part of the T-matrix, this would be a valuable adjoint to the present work.

BIBLIOGRAPHY

[1] Ernest S. Abers and Benjamin W. Lee. Phys. Rep. **9C**, 1 (1973).

[2] William Marciano and Heinz Pagels. Phys. Rep. **36C**, 139 (1978).

[3] A. Chodos, R. L. Jaffe, K. Johnson, C. B. Thorn, and V. F. Weisskopf. Phys. Rev. **D9**, 3471 (1974).

[4] A. Chodos, R. L. Jaffe, K. Johnson, and C. B. Thorn. Phys. Rev. **D10**, 2599 (1974).

[5] T. DeGrand, R. L. Jaffe, K. Johnson, and J. Kiskis. Phys. Rev. **D12**, 2060 (1975).

[6] P. Hasenfratz and J. Kuti. Phys. Rep. **40C**, 75 (1978).

[7] A. J. G. Hey. in *Proceedings of the Eighth International Seminar on Theroetical Physics, Salamanca, Spain, 1977*, edited by J. A. de Azcárraga. Springer-Verlag, Berlin, 1978.

[8] H. Pagels. Phys. Rep. **16**, 219 (1975).

[9] M. Gell-Mann and M. Lévy. Nuovo Cim. **16**, 705 (1960).

[10] J. Goldstone. Nuovo Cim. **19**, 154 (1961).

[11] Jeffrey Goldstone, Abdus Salam, and Steven Weinberg. Phys. Rev. **127**, 965 (1962).

[12] A. Chodos and Charles B. Thorn. Phys. Rev. **D12**, 2733 (1975).

[13] G. E. Brown and Mannque Rho. Phys. Lett. **82B**, 177 (1979).

[14] G. E. Brown, Mannque Rho, and Vincent Vento. Phys. Lett. **84B**, 383 (1979).

[15] R. L. Jaffe. in *Proceedings of the Seventeenth International School of Subnuclear Physics, Erice, Italy, 1979*, edited by Antonino Zichichi. Plenum, New York, 1982.

[16] C. E. DeTar. Phys. Rev. **D24**, 752 (1981).

[17] C. E. DeTar. Phys. Rev. **D24**, 762 (1981).

[18] G. A. Miller, A. W. Thomas, and S. Théberge. Phys. Lett. **91B**, 192 (1980).

[19] Gerald A. Miller, S. Theberge, and A. W. Thomas. Comm. Nucl. Part. Phys. **10**, 101 (1981).

[20] S. Théberge, A. W. Thomas, and Gerald A. Miller. Phys. Rev **D22**, 2838 (1980).

[21] S. Théberge, A. W. Thomas, and Gerald A. Miller. Phys. Rev **D23**, 2106 (1981).

[22] Serge Théberge, Gerald A. Miller, and A. W. Thomas. Can. J. Phys. **60**, 59 (1982).

[23] Serge Théberge. PhD thesis, The University of British Columbia (1982).

[24] A. W. Thomas. in *Advances in Nuclear Physics*, edited by J. Negele and E. Vogt. Vol. 13 page 1. Plenum, New York, 1984.

[25] A. W. Thomas and S. Théberge. Phys. Rev. **D24**, 216 (1981).

[26] S. Théberge and A. W. Thomas. Nucl. Phys. **A393**, 252 (1983).

[27] A. W. Thomas. J. Phys. **G7**, L283 (1981).

[28] Steven Weinberg. Phys. Rev. Lett. **17**, 616 (1966).

[29] Steven Weinberg. Phys. Rev. Lett. **18**, 188 (1967).

[30] B. K. Jennings and O. V. Maxwell. Nucl. Phys. **A422**, 589 (1984).

[31] B. K. Jennings, E. A. Veit, and A. W. Thomas. Phys. Lett. **148B**, 28 (1984).

[32] E. A. Veit, B. K. Jennings, and A. W. Thomas. Phys. Rev. **D33**, 1859 (1986).

[33] E. D. Cooper and B. K. Jennings. Phys. Rev. **D33**, 1509 (1986).

[34] E. D. Cooper, B. K. Jennings, P. A. M. Guichon, and A. W. Thomas. Nucl. Phys. **A469**, 717 (1987).

[35] E. A. Veit, B. K. Jennings, A. W. Thomas, and R. C. Barrett. Phys. Rev. **D31**, 1033 (1985).

[36] E. A. Veit, A. W. Thomas, and B. K. Jennings. Phys. Rev. **D31**, 2242 (1985).

[37] Mason B. Watson, Massimiliano Ferro-Luzz, and Robert D. Tripp. Phys. Rev. **131**, 2248 (1963).

[38] M. Sakitt, T. B. Day, R. G. Glasser, N. Seeman, J. Friedman, W. E. Humphrey, and R. R. Ross. Phys. Rev. **139**, 719 (1965).

[39] Jae Kwan Kim. Phys. Rev. Lett. **14**, 29 (1965).

[40] W. Kittel, G. Otter, and I. Wacek. Phys. Lett. **21**, 349 (1966).

[41] Jae Kwan Kim. Phys. Rev. Lett. **19**, 1074 (1967).

[42] T. S. Mast, M. Alston-Garnjost, R. O. Bangerter, A. S. Barbaro-Galtieri, F. T. Slomitz, and R. D. Tripp. Phys. Rev. **D 11**, 3078 (1975).

[43] Terry S. Mast, Margaret Alston-Garnjost, Roger O. Bangerter, Angela S. Barbaro-Galtieri, Frank T. Solmitz, and Robert D. Tripp. Phys. Rev. **D 14**, 13 (1976).

[44] R. O. Bangerter, M. Alston-Garnjost, A. Barbaro-Galtieri, T. S. Mast, F. T. Solmitz, and R. D. Tripp. Phys. Rev. **23**, 1484 (1981).

[45] J. Ciborowski, J. Gwizdz, D. Kielczewska, R. J. Nowak, E. Rondio, J. A. Zakrzewski, M. Goossens, G. Wilquet, N. H. Bedford, D. Evans, G. P. Fleming, Y. A. Hamam, J. V. Major, J. H. Bartley, D. H. Davis, D. J. Miller, D. N. Tovee, and T. Tymieniecka. J. Phys. **G 8**, 13 (1982).

[46] D. Evans, J. V. Major, E. Rondio, J. A. Zakrzewski, J. E. Conboy, D. J. Miller, and T. Tymieniecka. J. Phys. **G 9**, 885 (1983).

[47] William E. Humphrey and Ronald R. Ross. Phys. Rev. **127**, 1305 (1962).

[48] D. N. Tovee, D. H. Davis, and J. Simonovic. Nucl. Phys. **B33**, 493 (1971).

[49] R. J. Nowak, J. Armstrong, and D. H. Davis. Nucl. Phys. **B139**, 61 (1978).

[50] M. Goossens, G. Wilquet, J. L. Armstrong, and J. H. Bartley. in *Low and Interme-*

diate Energy Kaon-Nucleon Physics, edited by E. Ferrari and G. Violini. 1980.

[51] D. W. Thomas, A. Engler, H. E. Fisk, and R. W. Kraemer. Nucl. Phys. **B56**, 15 (1973).

[52] R. J. Hemingway. Nucl. Phys. **B253**, 742 (1985).

[53] M. Aguilar-Benitez and J. Salicio. Anales de Fisica A **77**, 144 (1981).

[54] E. A. Veit, B. K. Jennings, R. C. Barrett, and A. W. Thomas. Phys. Lett. **137B**, 415 (1984).

[55] Claude Itzykson and Jean-Bernard Zuber. *Quantum Field Theory*. McGraw-Hell Inc. 1980.

[56] C. Leroy. Phys. Rev. **D18**, 326 (1978).

[57] W. M. Gibson and B. R. Pollard. *Symmetry Principles in Elementary Particle Physics*. Cambridge University Press 1976.

[58] B. K. Jennings. (private communication).

[59] M. I. Haftel and F. Tabakin. Nucl. Phys. **158**, 1 (1970).

[60] R. H. Landau. Phys. Rev. **C27**, 2191 (1983).

[61] R. H. Landau and Beato Cheng. Phys. Rev. **C33**, 734 (1986).

[62] Yong Rae Kwon and F. Tabakin. Phys. Rev. **C18**, 932 (1978).

[63] Guangliang He, Paul Fink Jr., and Rubin Landau. Phys. Rev. **C40**, 1525 (1989).

[64] Particle Data Group. Phys. Lett. **239B**, 1 (1990).

[65] M. H. Alston, L. W. Alvarez, P. Eberhard, M. L. Good, W. Graziano, H. K. Ticho, and S. G. Wojcicki. Phys. Rev. Lett. **6**, 698 (1961).

[66] B. R. Martin and M. Sakitt. Phys. Rev. **183**, 1345 (1969).

[67] B. R. Martin and M. Sakitt. Phys. Rev. **183**, 1352 (1969).

[68] M. Alberg, E. M. Henley, and L. Wilets. Ann. Phys. **96**, 43 (1976).

[69] J. Schnick and R. H. Landau. Phys. Rev. Lett. **58**, 1719 (1987).

[70] P. B. Siegel and W. Weise. Phys. Rev. **C38**, 2221 (1988).

[71] Yasuo Umino and Fred Myhrer. Phys. Rev. **D39**, 3391 (1989).

[72] R. H. Dalitz and A. Deloff. J. Phys. **G 17**, 289 (1991).

[73] M. H. Alston, L. W. Alvarez, P. Eberhard, M. L. Good, W. Graziano, H. K. Ticho, and S. G. Wojcicki. Phys. Rev. Lett. **5**, 520 (1960).

[74] M. H. Alston, L. W. Alvarez, P. Eberhard, M. L. Good, W. Graziano, H. K. Ticho, and S. G. Wojcicki. Phys. Rev. Lett. **7**, 472 (1961).

[75] Roger G. Newton. *Scattering Theory of Waves and Particles.* McGraw-Hill New York, 1966.

[76] David Park. *Introduction to Strong Interactions.* Benjamin, New York, 1966.

[77] P. J. Fink, G. He, R. H. Landau, and J. W. Schnick. Phys. Rev. **C41** (1990).

[78] J. D. Davies, G. J. Pyle, G. T. A. Squier, C. J. Batty, S. F. Biagi, S. D. Hoath, P. Sharman, and A. S. Clough. Phys. Lett. **83B**, 55 (1979).

[79] M. Izycki, G. Backenstoss, L. Tauscher, P. Blum, R. Guigas, N. Hassler, H. Koch, H. Poth, K. Fransson, A. Nilsson P. Pavlopoulos, and K. Zioutas. Z. Phys. **A297**, 11 (1980).

[80] P. M. Bird, A. S. Clough, and K. R. Parker. Nucl. Phys. **A404**, 482 (1983).

[81] Jeffrey W. Schnick. PhD thesis, Oregon State University (1988).

Appendices

Appendix A

The Quark Wave Functions of the MIT Bag Model

For a static spherical MIT bag with radius R, the massless quark wave function is governed by the Dirac equation inside the bag

$$i \not{\partial} q(x) = 0 \quad r < R, \tag{A.1}$$

and the linear boundary condition

$$i \not{n} q(x) = q(x) \quad r = R, \tag{A.2}$$

where $\not{n} = -\boldsymbol{\gamma} \cdot \hat{r}$.

The Dirac equation (A.1) can be rearranged as

$$i\partial_t q = Hq \tag{A.3}$$

where the Hamiltonian H is defined as

$$H = \boldsymbol{\alpha} \cdot \mathbf{p} = -i\boldsymbol{\alpha} \cdot \nabla \tag{A.4}$$

and the 4×4 matrices $\boldsymbol{\alpha}$ are defined as

$$\boldsymbol{\alpha} = \begin{pmatrix} 0 & \boldsymbol{\sigma} \\ \boldsymbol{\sigma} & 0 \end{pmatrix} \tag{A.5}$$

with $\boldsymbol{\sigma}$ as the Pauli matrices.

The total angular momentum $\mathbf{J}$ is defined as the sum of the orbital angular momentum $\mathbf{l}$ and the spin $\boldsymbol{\Sigma}/2$

$$\mathbf{J} = \mathbf{l} + \frac{\boldsymbol{\Sigma}}{2} \tag{A.6}$$

where $\boldsymbol{\Sigma}$ is defined as

$$\boldsymbol{\Sigma} = \begin{pmatrix} \boldsymbol{\sigma} & 0 \\ 0 & \boldsymbol{\sigma} \end{pmatrix} \tag{A.7}$$

The total angular momentum $\mathbf{J}$ is conserved because it commutes with the Hamiltonian H

$$\begin{aligned} [\mathbf{J}, H] &= [\mathbf{l} + \boldsymbol{\Sigma}/2, H] \\ &= [\mathbf{r} \times \mathbf{p} + \boldsymbol{\Sigma}/2, \boldsymbol{\alpha} \cdot \mathbf{p}] \\ &= i\boldsymbol{\alpha} \times \mathbf{p} - i\boldsymbol{\alpha} \times \mathbf{p} \\ &= 0 \end{aligned} \tag{A.8}$$

If we define the operator K as

$$K = \beta(\boldsymbol{\Sigma} \cdot \mathbf{l} + 1) \tag{A.9}$$

we find that it commutes with both H, and $\mathbf{J}$.

$$\begin{aligned} [K, H] &= [\beta\boldsymbol{\Sigma} \cdot \mathbf{l}, \boldsymbol{\alpha} \cdot \mathbf{p}] + [\beta, \boldsymbol{\alpha} \cdot \mathbf{p}] \\ &= -2\beta\boldsymbol{\alpha} \cdot \mathbf{p} + 2\beta\boldsymbol{\alpha} \cdot \mathbf{p} \\ &= 0 \end{aligned} \tag{A.10}$$

and similarly

$$[K, \mathbf{J}] = 0 \tag{A.11}$$

Notice that we have the relation

$$K^2 = (\boldsymbol{\Sigma} \cdot \mathbf{l} + 1)^2 = \mathbf{l}^2 + \boldsymbol{\Sigma} \cdot \mathbf{l} + 1 = \mathbf{J}^2 + \frac{1}{4} \tag{A.12}$$

So the eigenvalue of K is related to eigenvalue of $\mathbf{J}$ by the relation

$$\kappa^2 = J(J+1) + \frac{1}{4} = \left(J + \frac{1}{2}\right)^2 \tag{A.13}$$

or

$$\kappa = \pm\left(J + \frac{1}{2}\right) \tag{A.14}$$

With all these help, we can now solve the Dirac equation for the eigenstate of H, $\mathbf{J}^2$, J_z and K. In spherical coordinates, we have

$$(\boldsymbol{\alpha} \cdot \mathbf{r})(\boldsymbol{\alpha} \cdot \mathbf{p}) = -ir\frac{\partial}{\partial r} + i\boldsymbol{\Sigma} \cdot \mathbf{l} = -ir\frac{\partial}{\partial r} + i(\beta K - 1) \tag{A.15}$$

and

$$(\boldsymbol{\alpha} \cdot \mathbf{r})(\boldsymbol{\alpha} \cdot \mathbf{r})(\boldsymbol{\alpha} \cdot \mathbf{p}) = r^2(\boldsymbol{\alpha} \cdot \mathbf{p}) \tag{A.16}$$

So we get the identity

$$(\boldsymbol{\alpha} \cdot \mathbf{p}) = -i(\boldsymbol{\alpha} \cdot \hat{r})\partial_r + \frac{i}{r}(\boldsymbol{\alpha} \cdot \hat{r})(\beta K - 1) \tag{A.17}$$

Notice that $\boldsymbol{\alpha} = \gamma_5 \boldsymbol{\Sigma}$, then for a stationary solution q, we can write the Dirac equation (A.3) as

$$Hq = -i\gamma_5(\boldsymbol{\Sigma} \cdot \hat{r})\left(\frac{\partial}{\partial r} + \frac{1}{r} - \frac{\beta K}{r}\right) q = Eq \tag{A.18}$$

and q is also eigenfunction of $\mathbf{J}^2$, J_z and K, as we mentioned before.

$$\mathbf{J}^2 q_J^{M,\kappa} = J(J+1) q_J^{M,\kappa} \tag{A.19}$$

$$J_z q_J^{M,\kappa} = M q_J^{M,\kappa} \tag{A.20}$$

$$K q_J^{M,\kappa} = -\kappa q_J^{M,\kappa} \tag{A.21}$$

For the convenience, we write q as

$$q_J^{M,\kappa} = \begin{pmatrix} \phi_{J,U}^{M,\kappa} \\ \phi_{J,L}^{M,\kappa} \end{pmatrix} \tag{A.22}$$

where $\phi_{J,U}^{M,\kappa}$ and $\phi_{J,L}^{M,\kappa}$ are Pauli spinors with total angular momentum jm, and

$$(\boldsymbol{\sigma} \cdot \mathbf{l} + 1) \phi_{J,U}^{M,\kappa} = -\kappa \phi_{J,U}^{M,\kappa} \tag{A.23}$$

$$(\boldsymbol{\sigma} \cdot \mathbf{l} + 1) \phi_{J,L}^{M,\kappa} = \kappa \phi_{J,L}^{M,\kappa} \tag{A.24}$$

We know that the spin-angle functions $\mathcal{Y}_{lJ}^M$ has the property

$$(\boldsymbol{\sigma} \cdot \mathbf{l}) \mathcal{Y}_{lJ}^M = \left(J(J+1) - l(l+1) - \frac{3}{4} \right) \mathcal{Y}_{lJ}^M \tag{A.25}$$

Then we can write ϕ_U and ϕ_L as

$$\phi_{J,U}^{M,\kappa} = g(r) \mathcal{Y}_{lJ}^M \tag{A.26}$$

$$\phi_{J,L}^{M,\kappa} = i f(r) \mathcal{Y}_{l'J}^M \tag{A.27}$$

the l and l' are related to J and κ by the relation

$$-\kappa = J(J+1) - l(l+1) + \frac{1}{4} \tag{A.28}$$

$$\kappa = J(J+1) - l'(l'+1) + \frac{1}{4} \tag{A.29}$$

For the spin-angle function $\mathcal{Y}_l^{jm}$, we know that $J = l \pm 1/2$. For the case $J = l - 1/2$, we have

$$l = \kappa \tag{A.30}$$

$$l' = \kappa - 1 \tag{A.31}$$

and for the case $J = l + 1/2$, we have

$$l = -\kappa - 1 \tag{A.32}$$

$$l' = -\kappa \tag{A.33}$$

Now let us go back to Eq. (A.18), using the identity

$$(\boldsymbol{\sigma} \cdot \hat{r})\mathcal{Y}_{lJ}^M = -\mathcal{Y}_{l'J}^M \tag{A.34}$$

we have

$$\left(\frac{d}{dr} + \frac{1+\kappa}{r}\right) g(r) = Ef(r) \tag{A.35}$$

$$\left(\frac{d}{dr} + \frac{1-\kappa}{r}\right) f(r) = -Eg(r) \tag{A.36}$$

These set of equations can be rewritten as

$$\frac{d^2g}{dr^2} + \frac{2}{r}\frac{dg}{dr} + \left(E^2 - \frac{\kappa(\kappa+1)}{r^2}\right) g = 0 \tag{A.37}$$

$$\frac{d^2f}{dr^2} + \frac{2}{r}\frac{df}{dr} + \left(E^2 - \frac{\kappa(\kappa-1)}{r^2}\right) f = 0 \tag{A.38}$$

and these are the differential equations for the spherical Bessel and Hankel functions. The spherical Hankel function is not related in this case because it diverges at $r = 0$. For the case of $J = l - 1/2$, $\kappa = l$ and $l' = l - 1$, the solution for g is (up to a constant)

$$g(r) = j_l(Er) \tag{A.39}$$

Using the identity

$$j_l'(x) = j_{l-1} - \frac{l+1}{x} j_l(x) \tag{A.40}$$

we can find that

$$f(r) = \frac{1}{E}\left(\frac{dg}{dr} + \frac{1+\kappa}{r} g\right) = j_{l-1}(Er) = j_{l'}(Er) \tag{A.41}$$

Therefore the 4-component quark wave function is

$$q_J^{M,\kappa} = N \begin{pmatrix} j_l(Er)\mathcal{Y}_{lJ}^M \\ i j_{l'}(Er)\mathcal{Y}_{l'J}^M \end{pmatrix} = N \begin{pmatrix} j_l(Er) \\ -i(\boldsymbol{\sigma}\cdot\hat{r}) j_{l'}(Er) \end{pmatrix} \mathcal{Y}_{lJ}^M \tag{A.42}$$

For the case of $J = l + 1/2$, $\kappa = -(l+1)$, and $l' = l+1$, the solution for g is

$$g(r) = j_l(Er) \tag{A.43}$$

Using the identity

$$j_l'(x) = \frac{l}{x} j_l(x) - j_{l+1}(x) \tag{A.44}$$

we can find

$$f(r) = \frac{1}{E}\left(\frac{dg}{dr} + \frac{1+\kappa}{r} g\right) = -j_{l+1}(Er) = -j_{l'}(Er) \tag{A.45}$$

There fore the 4-component quark wave function is

$$q_J^{M,\kappa} = N \begin{pmatrix} j_l(Er)\mathcal{Y}_{lJ}^M \\ -i j_{l'}(Er)\mathcal{Y}_{l'J}^M \end{pmatrix} = N \begin{pmatrix} j_l(Er) \\ i(\boldsymbol{\sigma}\cdot\hat{r}) j_{l'}(Er) \end{pmatrix} \mathcal{Y}_{lJ}^M \tag{A.46}$$

The normalization constant N is determined by the condition

$$\int d^3x\, q^\dagger q = 1 \tag{A.47}$$

and the energy level E is determined by the boundary condition (A.2). Also please notice that all above derivation is done inside the bag, so the wave function is only valid inside the bag. Outside the bag, the wave functions vanish.

$S_{1/2}$ Quark Wave Function

For $S_{1/2}$ quark wave function, $l = 0$, $J = 1/2$, $l' = 1$ and $\kappa = -1$. So we have

$$q_s^M = N \begin{pmatrix} j_0(\omega_s r) \\ i(\boldsymbol{\sigma}\hat{r}) j_1(\omega_s r) \end{pmatrix} \chi^M \tag{A.48}$$

The boundary condition (A.2) implies that

$$j_0(\omega_s R) = j_1(\omega_s R) \tag{A.49}$$

and the lowest solution is

$$\omega_s = \frac{2.04}{R} \tag{A.50}$$

$P_{1/2}$ Quark Wave Function

For $P_{1/2}$ quark wave function, $l = 1$, $J = 1/2$, $l' = 0$ and $\kappa = 1$. We have

$$q^M_{p_{1/2}} = N \begin{pmatrix} j_1(\omega_{p1} r) \\ -i(\boldsymbol{\sigma} \cdot \hat{r}) j_0(\omega_{p1} r) \end{pmatrix} \mathcal{Y}^M_{1,1/2} = N' \begin{pmatrix} -j_1(\omega_{p1} r)(\boldsymbol{\sigma} \cdot \hat{r}) \\ i j_0(\omega_{p1} r) \end{pmatrix} \chi^M \tag{A.51}$$

The boundary condition (A.2) implies that

$$j_0(\omega_{p1} R) = -j_1(\omega_{p1} R) \tag{A.52}$$

and the lowest solution is

$$\omega_{p1} = \frac{3.81}{R} \tag{A.53}$$

$P_{3/2}$ Quark Wave Function

For $P_{3/2}$ quark wave function, $l = 1$, $J = 3/2$, $l' = 2$ and $\kappa = -2$. We now have

$$q^M_{p_{3/2}} = N \begin{pmatrix} j_1(\omega_{p3} r) \\ i(\boldsymbol{\sigma} \cdot \hat{r}) j_2(\omega_{p3} r) \end{pmatrix} \mathcal{Y}^M_{1,3/2} \tag{A.54}$$

The boundary condition (A.2) implies that

$$j_2(\omega_{p3} R) = -j_1(\omega_{p3} R) \tag{A.55}$$

and the solution is

$$\omega_{p3} = \frac{3.20}{R} \tag{A.56}$$

Appendix B

Additional Fits

We give more fits in this appendix. Fc2.n.n.n.7 is a fit which fits only to the scattering data and fc2.n.n.n.c1 is a fit which fits to the scattering data with manually assigned equal error bars. The final parameters of these two fits are listed in Table 15. And the theoretical curves are shown in Figures 38-44. The curves labeled as tc2.n.n.n.7 corresponding to the fit fc2.n.n.n.7 and tc2.n.n.n.c1 corresponding to fit fc2.n.n.n.c1.

	R	M_s^*	M_p^*	M_d^*	$f^{I=0}$	$f_K^{I=1}$	$f_\pi^{I=1}$
fc2.n.n.n.7	1.34	1564	-1249	1553	92	80	88
fc2.n.n.n.c1	1.19	1623	-12682	1568	90	87	80

Table 15. Final parameters of the additional fits. The radius R is in fm, and other parameters are in MeV.

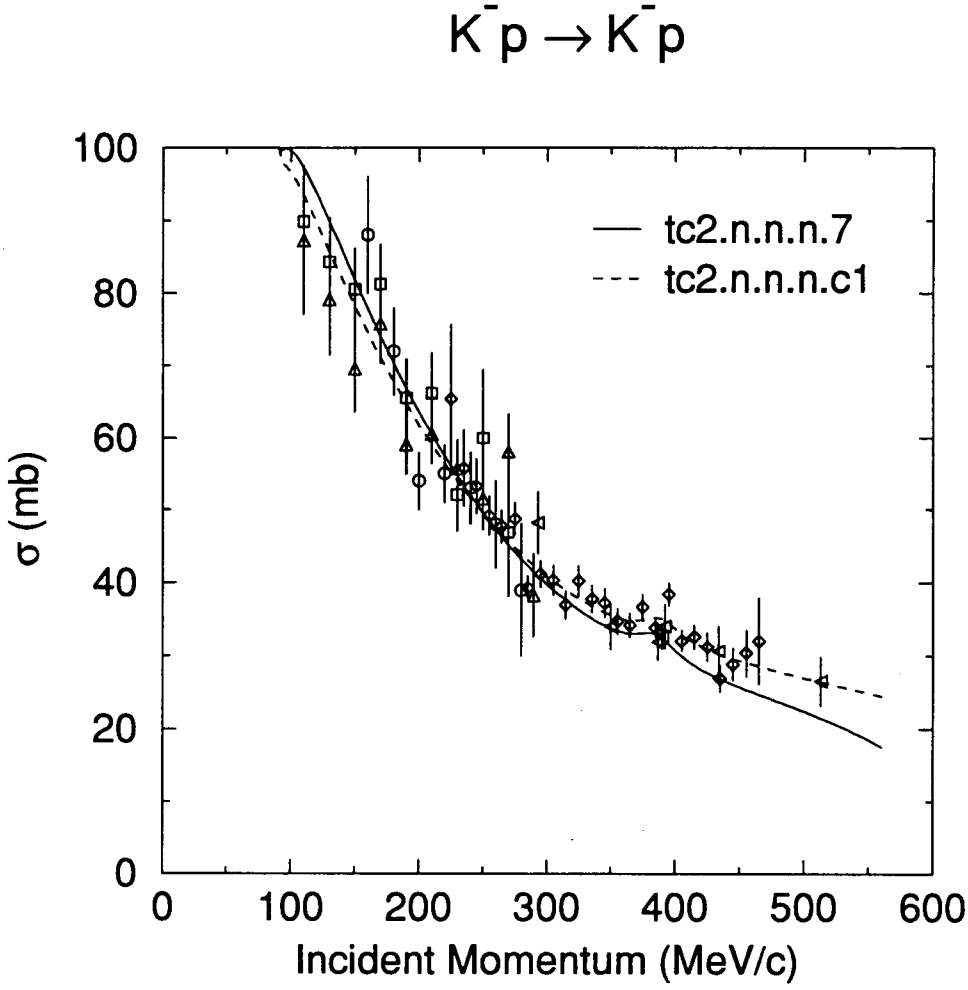

Figure 38. The $K^- p \rightarrow K^- p$ elastic scattering cross sections calculated by the CBM with the parameter sets from the additional fits.

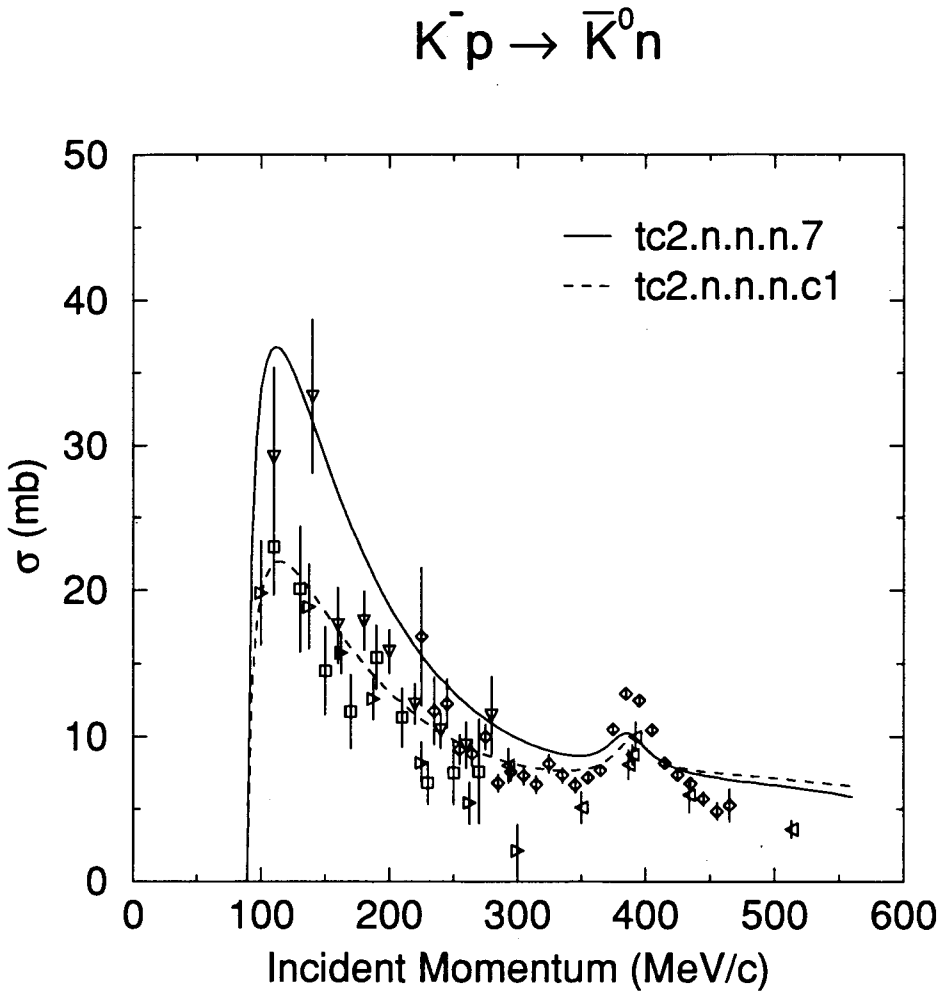

Figure 39. The $K^- p \rightarrow \bar{K}^0 n$ charge exchange cross sections calculated by the CBM with the parameter sets from the additional fits.

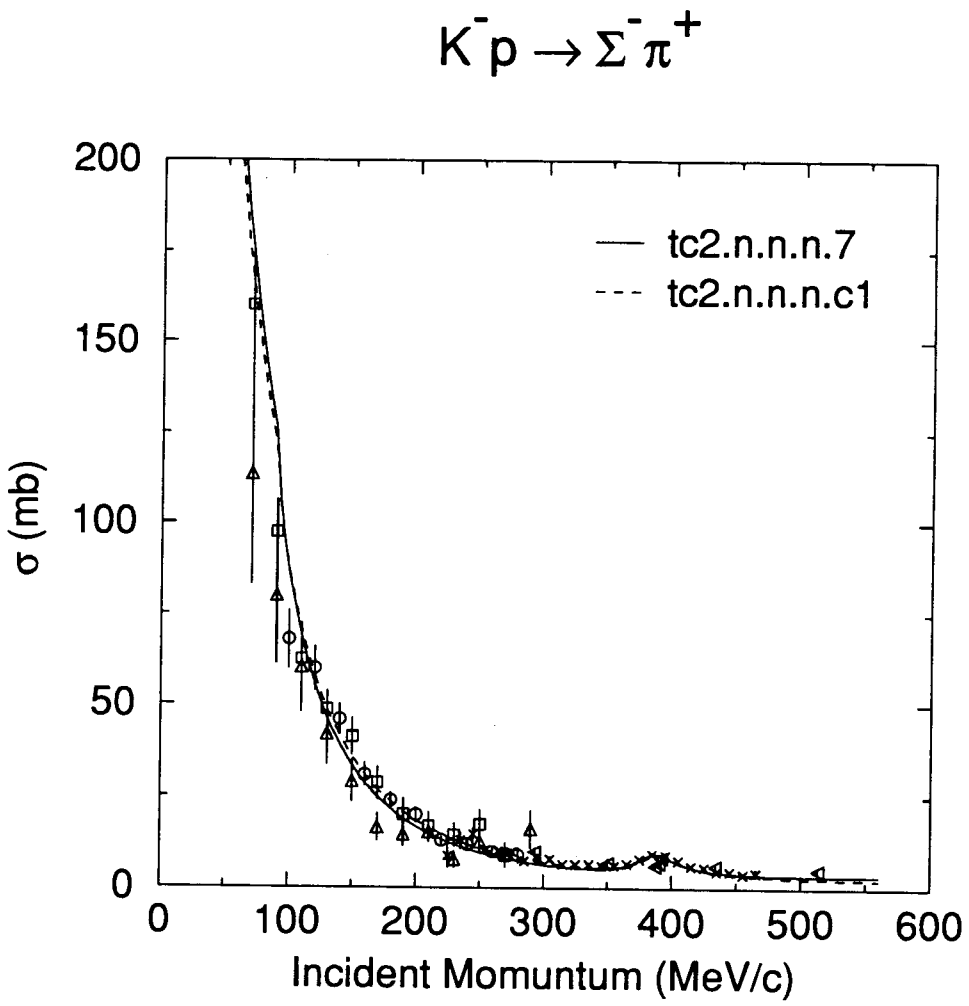

Figure 40. The $K^- p \rightarrow \pi^+ \Sigma^-$ reaction cross sections calculated by the CBM with the parameter sets from the additional fits.

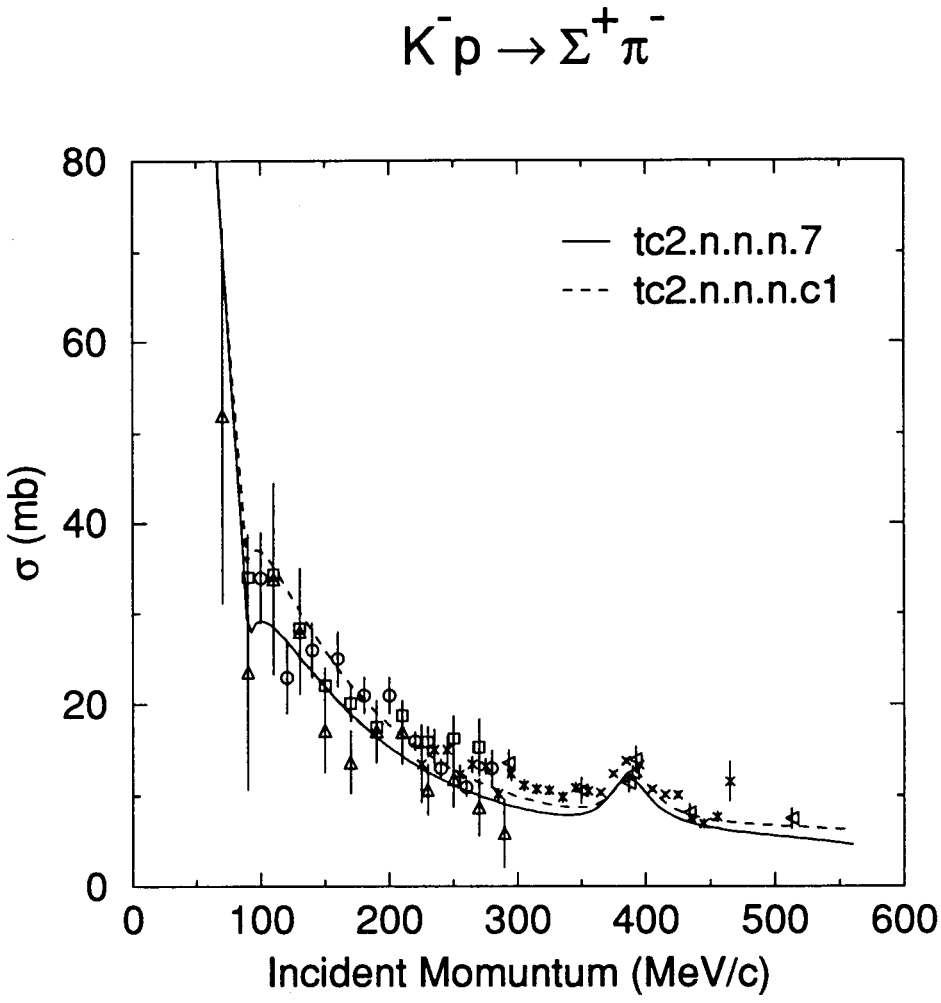

Figure 41. The $K^- p \rightarrow \pi^- \Sigma^+$ reaction cross sections calculated by the CBM with the parameter sets from the additional fits.

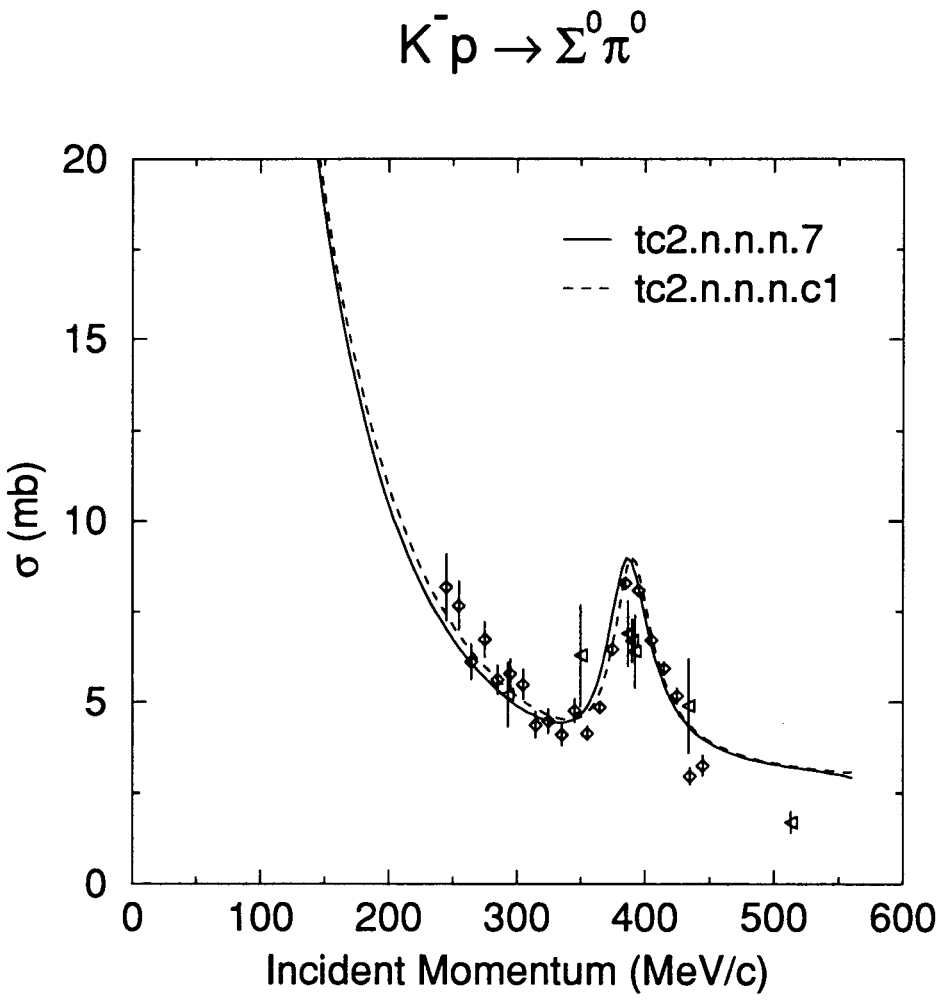

Figure 42. The $K^- p \rightarrow \pi^0 \Sigma^0$ reaction cross sections calculated by the CBM with the parameter sets from the additional fits.

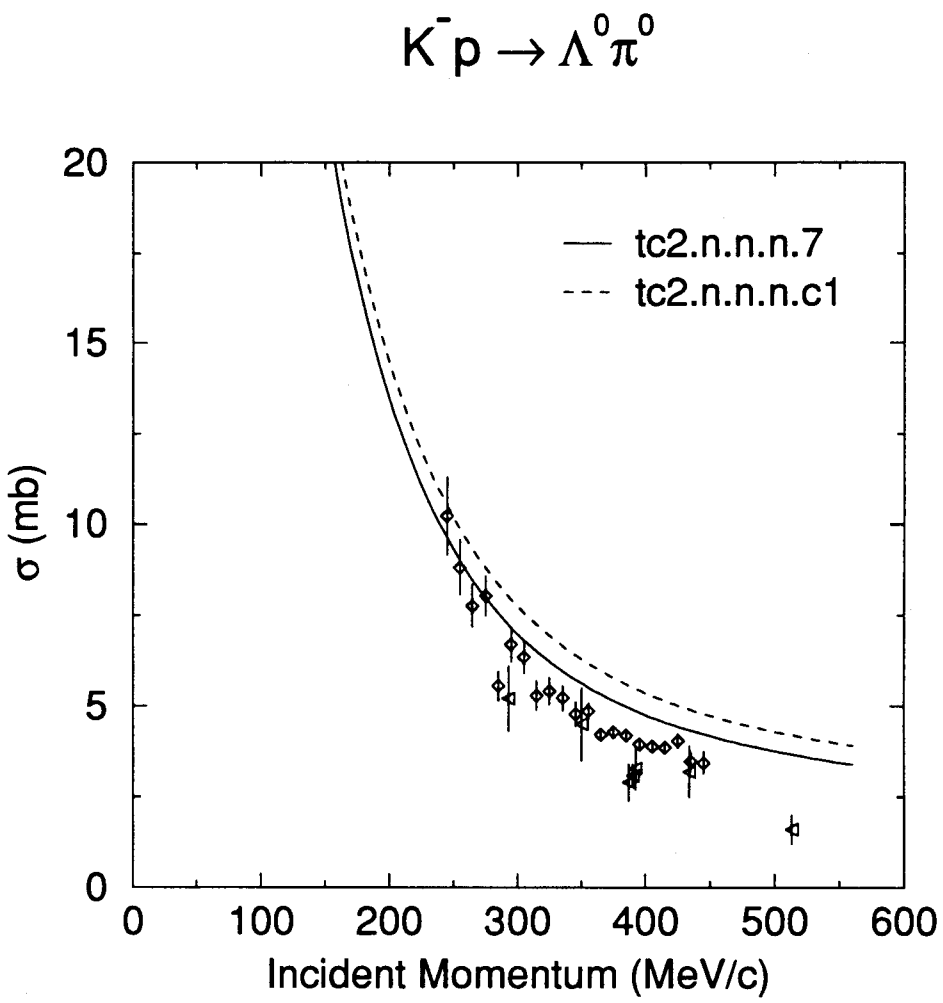

Figure 43. The $K^- p \rightarrow \pi^0 \Lambda$ reaction cross sections calculated by the CBM with the parameter sets from the additional fits.

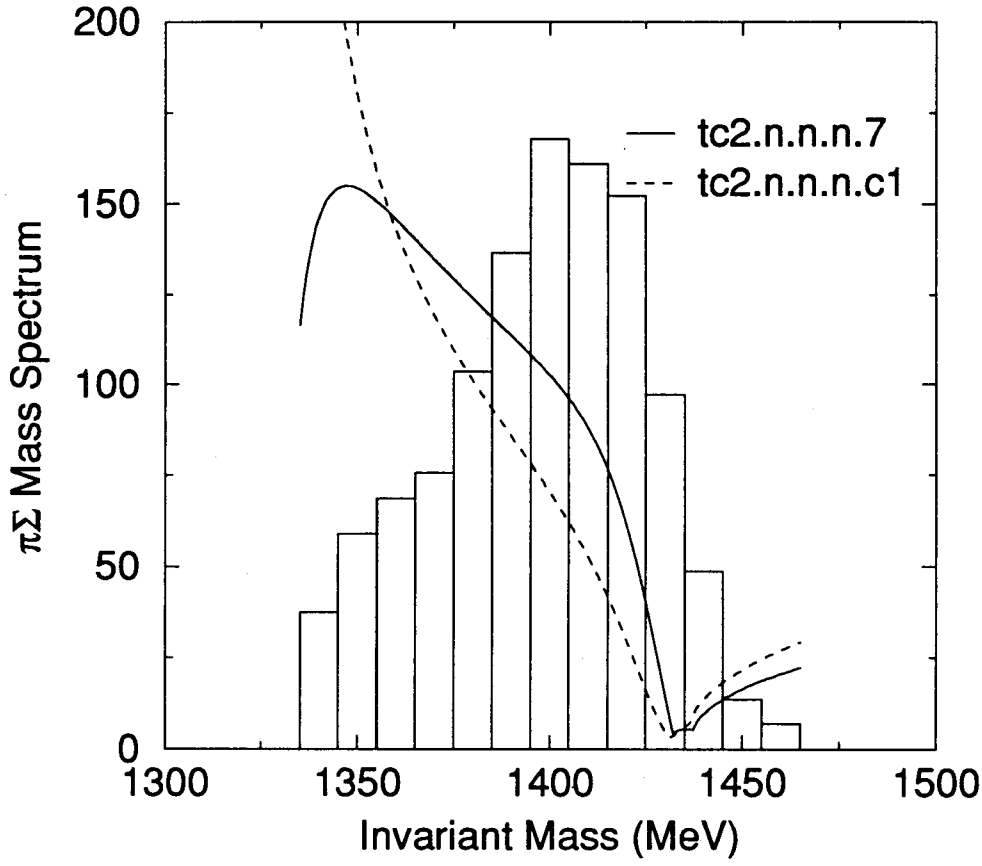

Figure 44. The $\pi\Sigma$ mass spectrum calculated by the CBM with parameter sets from the additional fits.